UNIVERSITÀ DEGLI STUDI DI GENOVA

SCUOLA POLITECNICA

Dipartimento di Ingegneria Navale, Elettrica, Elettronica e delle Telecomunicazioni

Corso di Dottorato in
Ingegneria Elettrica

PhD Thesis

STATIC MAGNETIC FIELD IMPACT ON SEMICONDUCTOR DEVICES AND CENTRIFUGAL PUMPS AT ITER

Revisori: *Chiar.^{mo} Prof. Ing Marco Aurelio Schroeder*
Chiar.^{ma} Prof. Ing. Gabriela Nicoleta Sava

Tutor di dottorato:
Chiar.^{mo}Prof. Ing. Renato Procopio

Candidate: Damiano Lanzarotto

Academic Year
2020/2021

Ringraziamenti

Un ringraziamento speciale a chi ha permesso la realizzazione del mio percorso di dottorato, a chi ha lavorato al mio fianco e a chi a distanza ha trasmesso consigli ed informazioni preziose al compimento di questo lavoro.

Ed infine, alla mia famiglia e al loro incondizionato supporto, agli amici e al loro immancabile sostegno e a tutti coloro che ho lungo il mio percorso professionale e personale hanno stimolato una maturazione della mia persona.

Introduction

An astounding number of components belonging to subsystems of different nature are installed in the ITER Tokamak building and all of those subjected to a constant or slowly variable magnetic field, an environmental condition unusual for other standard applications. Indeed, the magnetic field generated by ITER magnets can reach 70 mT in the crane hall of the Tokamak building, with a maximum derivative of 10 mT/s.

Among these components, there are a few which are critical in the correct operation of the overall system and on which extremely few data are available regarding their interaction with a strong External Static Magnetic Field (ESMF). In particular, power semiconductor devices and pumps stand out as key elements in the electrical distribution network supplying the magnets and in all cooling applications respectively.

Naturally, these two groups of components are not the only one potentially greatly affected by the ESMF, but the current phase of the plant design and construction requires an immediate action in gathering information on how the operation of these two very different devices is affected by the magnetic field.

Unfortunately, a very limited number of work is available both regarding the countermeasures that must be taken in designing power electronic systems and cooling pumps operating in the environment described above. Besides, no information is available concerning the magnetic compatibility of standard components normally installed nowadays in industrial applications.

In order to identify the operational limits of many other components such as low power electronics, low voltage circuit breakers, sensors, contactors, logical controllers and other control electronic devices, ITER in collaboration with external contractors put in place a set of experimental tests in the last two decades, whose main results were described in some papers and internal reports.

In particular, a large amount of operational malfunctioning and failure were observed, for instance; electromechanical relays would open or close with a certain delay, or they even would not close or open at all, depending on many factors such as their orientation with respect to the magnetic field direction. Usual active current transducers (LEM) might experience a 0.5% offset drift at 10 mT, typical pulse transformers work properly only up to 50 mT, switch mode power supply might generate some acoustic noise, increase the peak current in switching transistors and may even be destroyed in a DC induction higher than 30 mT, etc.

All the components which underwent the DC magnetic field immunity tests could be grouped into 3 main categories:

- Components whose operation relies on some ferro-magnetic nucleum (i.e. transformers, inductors, mechanical relays etc.).
- Sensors whose physical principle which they are based on relies on magnetic field measurements (Hall effect sensors).
- Semiconductor devices, electronics.

Although the physical mechanisms and interactions between a static magnetic field and the first two categories of components are clear and commonly known (they basically come down to iron saturation and the distortion of the hall voltage), it is still unclear how a DC magnetic fields inter-acts with solid state device.

Therefore, thrusted by the results (sometimes worrying) of previous test campaigns, ITER is currently moving towards the preparation of further experimental analysis, with a particular focus on power semiconductor devices (IGBTs, Thyristors, IGCTs etc.), pumps and electric motors. While some internal studies have already been made on the latter subject, no analysis has been carried out yet on pumps and power semiconductor devices.

Thus, it is exactly in this framework that this study places itself into, particularly pursuing two main goals which can be considered to be dual:

1. Provide a theoretical/simulation analysis useful for the interpretation of the results of future tests.
2. Provide fundamental insights and criteria to design devices specifically immunes to the presence of an ESMF (information which can difficultly be drawn from experimental tests), especially needed when no shielding is feasible.

As regards the analysis of the semiconductor devices, the aims are first to analyse the documents available in the scientific literature concerning the interaction between an ESMF and solid state devices. Secondly, due to the current lack at ITER of dedicated software licenses able to conduct this sort of compatibility analysis, to develop a simulation tool in MATLAB able to quantify, after some approximation and simplifications, the impact of a static magnetic field on solid state technology.

Given the degree of approximation in this case, the results are only to be interpreted as an indication of the order of magnitude of the considered phenomenon and as an indication of the potentially critical operating conditions to target for monitoring during the experimental tests.

On the other hand, as regards the analysis of centrifugal pumps, the magnetic analysis is carried out through the ANSYS/Maxwell software, allowing to obtain significantly more accurate predictions.

Analysis of the effect of a static magnetic field on semiconductor devices

1 Literary Review

1.1 Early research

Identifying works dealing with any study regarding how the behaviour of semiconductor device is affected by an External Static Magnetic Field (ESMF) is no easy task, the number of such works being extremely limited.

According to examined literature, one of the first studies concerning this phenomenon can be traced in [1]. In particular, this paper groups the effect caused by a magnetic field on the current flow across a semiconductor device into two categories:

- Category 1: The magnetic field may cause changes in the underlying electronic structure of the semiconducting material, therefore altering the basic device characteristics.
- Category 2: While leaving the electronic structure unchanged, the field may act directly on the current carriers, causing a redistribution of the current flow across the device (as it will be more clearly explained in section 5.4, this is the main focus of this report).

In particular, the authors of [1] focused their attention on the second group of effects and showed both from a theoretical and experimental point of view that a non uniform current density flowing through a p-n junction is determined by an external transverse static magnetic field. It is interesting to notice that [1] dates back to 1965 and it represents one of the first attempts to quantitatively describe the interaction bewteen a magnetic field and the physics of solid state devices.

Another very interesting research can be found in a NASA report dated 1970 [2]; in particular, the aim of the authors was to experimentally determine how the operational characteristics of various types of transistors were affected by both the magnetic strength and its orientation. The main results in this report show that a degradation in forward current ratio (ratio of the collector current to its base current) takes place due to the application of an external constant magnetic field. Specifically, the above mentioned degradation is assumed to be caused by different phenomena, such as:

1. A magnetic field dependent diffusion length (mean net distance a particle diffuses during its life time).
2. An increased resistive behavior, called ”Magnetoresistance” (MR) effect.

Probably, the first time the term ”Magnetoresistance” was associated with semiconductor devices took place in [3] in 1962; however, it has been investigated more thoroughly only in the last decade (for that reason a detailed description of this phenomenon is reported in the next section). Another couple of seemingly interesting works can be identified in [4, 5], but unfortunately it was not possible to aquire any of them and [3] as well, since, given the old publication date, it appears only their hard-copy formats exist.

On balance, it can be stated that the first category of effects proposed by [1] requires some deep background in physics of matter in order to be able to perform useful considerations, the second one can be analysed more effectively from an engineering point of view. Besides, it seems that the second group has been more widely investigated by researchers, as the vast majority of recent pubblications concerning this phenomenon fall into such category.

1.2 Latest research – Overview of the experimental findings on “Magnetoresistance” effect

The ”Magnetoresistance (MR)” effect, whose first analysis in relation with semiconductor devices was introduced in [3], has recently been at the center of some authors’ interest.

The most significant work concerning MR in semiconductor devices is [6], published in 2013, that clearly explains the origin of MR effect on a semiconductor from a physical point of view also including some effective experimental results. Following this work, an angular dependence of the MR effect in a silicon based p-n junction device is shown in [7], while a temperature dependent asymmetry of anysotropic MR in silicon p-n junctions is shown in [8].

All these works explore different aspects of the MR effect; thus, in order to understand the main concepts described, it is important to understand how the MR effect arises in semiconductor devices and what consequences it produces on the device during its normal operation.

From [6] one can read:

“At zero-magnetic field, the space-charge region between p-type and n-type silicon is uniform. Its width depends on the equilibrium between the diffusion process and the built-in electric field. However, when the external magnetic field is applied, the

equilibrium is broken. The carriers in n-type and p-type region are deflected by Lorenz force and accumulate at the edges of the sample. As a result, a trapezoidal distribution in Space-Charge Region (SCR) is formed to balance the magnetic field" (see Fig. 1).

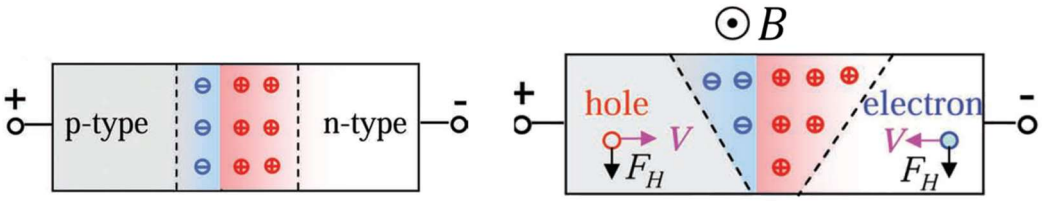

Fig. 1 Schematic representation of a p-n junction with and without an external static magnetic field

"Because the transport properties of the p–n junction strongly depend on the configuration of the SCR, the spatial distribution in space-charge region under the external magnetic field can drastically change the junction resistance.

Moreover, since the MR effect of p–n junction mainly stems from a change of SCR manipulated by the external magnetic field, the carrier concentrations play a very important role for the MR effect of p–n junction. When the magnetic field is applied, a carrier concentration gradient is formed due to the trapezoidal distribution of SCR. Such carrier concentration distribution strongly affects the junction resistance. It not only makes the electric field inhomogeneous, hence deflecting the current, but also it directly influences the silicon resistivity itself.

It is commonly known that the width of the SCR can be tuned by the electric field, as a consequence, the resistance of the p–n junction varyies by several orders of magnitude, i.e., from conducting to cut-off. This is known as the "rectification effect" of the p–n junction. The following interesting question is, what happens in the p–n junction when permeated by a constant magnetic field? Can the magnetic field also change the SCR, just like the electric field?

On the one hand, in contrast to conventional semiconductors under a magnetic field, there are enough accumulated carriers to generate a Hall electric field to balance the Lorentz force, on the other hand, the mobilizable carriers in the SCR are too few to balance the Lorentz force. Instead, a carrier concentration deviation is formed, which induces a diffusion process to compensate the Lorentz force in the SCR. This hypothesis is also confirmed by considering the carrier movement in the p- and n-type regions. The carriers in the p- and n-type regions are both deflected owing to the Lorentz force. The deflected carriers will accumulate at the boundary

and thus change the SCR. As a result, the carrier concentration in the SCR shows a deviation."

The following figure shows the effects of an applied electric field and an ESMF on the SCR boundaries of a p-n junction: applying a forward electric field leads to a shrinking of the SCR width (from black solid line to black dashed line), in addition an external constant magnetic field makes the SCR configuration trapezoidal (red dashed line).

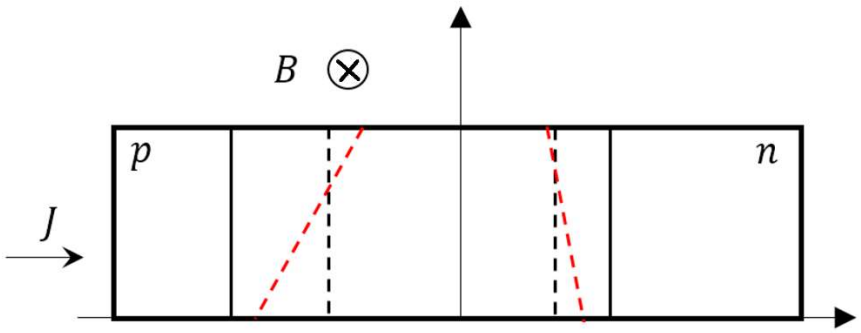

Fig. 2 p-n junction space charge region boundaries in thermal equilibrium (black solid line), under the effect of an applied electric field (black dashed line) and an external constant magnetic field (red dashed line).

On balance, the main conclusions which can be drawn from these research are the following:

- A supposedly large MR effect arises when a semiconductor device is permeated by an ESMF.
- The entity of this effect strongly depends on the ESMF magnitude and on the device temperature.

For instance, the change of the I-V characteristics depending on the applied transverse constant magnetic field are experimentally measured in [6] at 300K for a silicon p-n junction (more details are available in the paper) and they can be observed in Fig. 3:

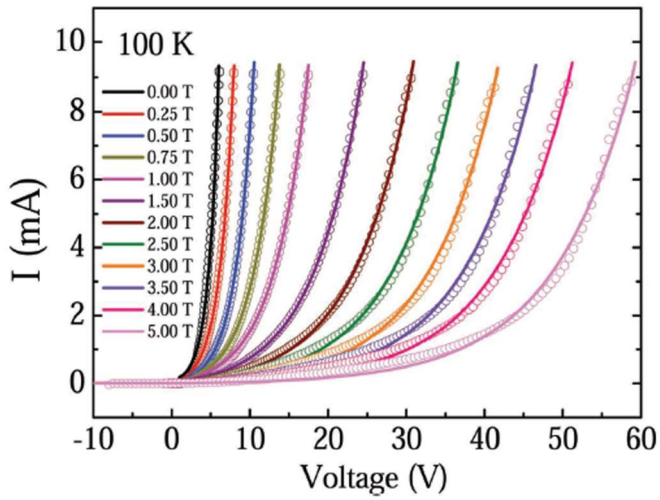

Fig. 3 I-V characteristics for a Silicon p-n junction permeated by different values of transverse constant magnetic field at 300K

It is immediate to notice the effect of the magnetic field on the steady state behavior of the p-n junction, which causes a sort of "dilatation" of the I-V characteristics towards right (i.e. the junction resistance increases with the applied magnetic field). Such increased resistance phenomenon strongly depends on the junction temperature, in particular, this can be shown by defining the following quantity:

$$MR(\%) = \frac{R(H) - R(0)}{R(0)} 100 \tag{1}$$

Where $R(0)$ and $R(H)$ are the resistance (V/I) at zero magnetic field and at the considered magnetic field respectively computed at a specific current value. Once MR is defined, the dependence of the entity of the MR effect on the junction temperature is shown in Fig. 4 [6]:

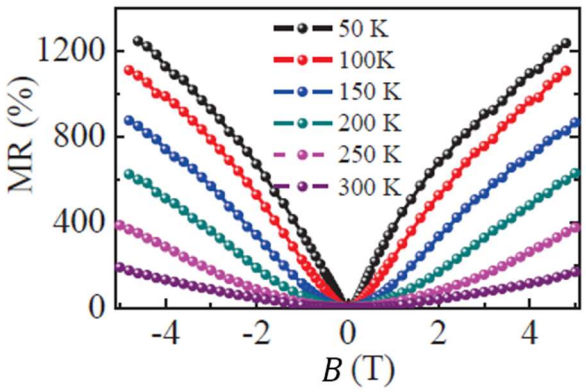

Fig. 4 MR ratio for different values of magnetic field as a function of the junction temperature at $\boldsymbol{I = 10mA}$

1.3 The importance of MR modelling

A large MR effect is shown to take place in p-n junction under an ESMF in all the works mentioned above; however, it is fundamental to notice some key points in the analyzed research:

1. None of these research works regard power electronic devices, but only "small signal" components.
2. The MR phenomenon is regarded as a positive effect, in that the authors' perspective is to make out of these components some "magnetosensors". Their aim is then to exploit this phenomenon, thus, the higher the MR, the better.
3. The applied ESMF goes well beyond (> 1 T in all the cases) the maximum value of the field affecting the power converters in the Tokamak building (70 mT).
4. The MR effect is shown only in steady state, no hints are given on what might happen in transients.

Therefore, it is important to analyse some fundamental consequences of aspects 1-4 in order not to draw wrong conclusions:

- Aspect 1: some parameters can be extremely different from signal components to power components (to name a few: geometry, doping levels, operating temperature etc…), in addition, for power converters, the junction temperature of the power semiconductor is a critical design parameter. Besides, power semiconductors, such as thyristors, are much larger (at least some thousand times) than signal semiconductors, it is therefore unclear so far how the component dimensions come into play in such scenario.
- Aspect 2: the MR effect could be exaggerated in order to stress the novelty and the validity of these research.
- Aspect 3: it is unclear if the ESMF in the range 10 mT – 70 mT has either a negligible or significant effect on the p-n junction, including estimating its operating temperature and hotspots.
- Aspect 4: a different dynamic behavior influences switching losses, could affect the dead time compensation, could affect the harmonic injection etc.

Because of the reasons mentioned above, what can be inferred from these research works is that some problems may arise in power semiconductor device due to the MR effect, however, is totally unclear to which extent. Therefore, it is crucial for ITER's purposes to develop a model describing such phenomenon in order to understand if typical power electronic devices operating in normal conditions,

permeated by an ESMF in range between 10 mT and 70 mT, experience any performance deterioration both in steady state and dynamic conditions.

1.4 Latest research – Overview of the modelling of "Magnetoresistance" effect in semiconductor devices and criticism of the analysed works

According to examined literature, the only attempt aiming at developing a model of a p-n junction influenced by an ESMF can be traced in [9]. The authors of this paper tried to develop a one-dimensional model of a p-n junction operating in steady state under a transverse ESMF, in addition they claimed they had successfully modelled the effect of the magnetic field on the SCR geometry (i.e how the SCR boundaries form a trapezoidal shape). Although such results appear appealing, after some reasoning it seemed clear that this research was developed on the basis of two seriously wrong considerations, which, unfortunately, make the proposed model totally unreliable.

In particular, the mistakes made by the authors of [9] can be pinpointed as follows (please remember that the underlined quantities represent vectors throughout the report):

1. The irrotationality of the electric field (i.e. the condition: $curl(\underline{E}) = \underline{0}$) is incorrectly violated in order to obtain a 1-dimensional model.
2. The Lorentz's force is wrongly applied.

The first mistake is easily identifiable, as a matter of fact, recalling the first Maxwell's equation:

$$\nabla \times \underline{E} = -\frac{\partial \underline{B}}{\partial t} \tag{2}$$

and since $\underline{B}$ is assumed to be time-constant, (2) becomes:

$$\nabla \times \underline{E} = \underline{0} \tag{3}$$

However, the electric field computed in [9] (see equation (7)) and which the proposed model is based on, does not satisfy (3).

As regards the second error, the authors exploited an incomplete relation between the carrier speed and the current density (equation (3) in [9]). In order to properly understand this problem, let us recall how the current in a semiconductor device is computed. It is common practice to calculate the total current density as:

$$\underline{J} = \underline{J}_n + \underline{J}_p \tag{4}$$

Where $\underline{J}_n$ and $\underline{J}_p$ are the electron and hole current density vectors respectively. Electron and hole current densities are caused by two physical phenomena: the electric field applies some force on the carriers, giving rise to the "drift components", while the concentration gradients with respect to the space coordinates determine the "diffusion components" (for more details please refer to [10]), therefore, $\underline{J}_n$ and $\underline{J}_p$ are defined as:

$$\underline{J}_n(x,y,z) = q\mu_n n(x,y,z)\underline{E}(x,y,z) + qD_n \nabla n(x,y,z) \tag{5}$$

$$\underline{J}_p(x,y,z) = q\mu_p p(x,y,z)\underline{E}(x,y,z) - qD_p \nabla p(x,y,z) \tag{6}$$

where q is the elementary charge, μ_n and μ_p are the electron and hole mobilities (as a first approximation they can be considered as constant parameters), n and p are the electron and hole concentrations respectively and finally D_n and D_p are the electron and hole diffusion coefficients respectively.

For notation simplification the space coordinate dependence of the main variables most of the times omitted further in the report, except when strictly needed.

Coming back to the second mistake, in order to evaluate the carrier speed, only the drift component of the current densities were considered in [9], wrongfully neglecting the diffusion components (which are of the same order of the drift components, or even higher). It follows that the Lorentz's force has been undoubtedly misevaluated. Thus, the correct relation between the carrier speed and the current density is [11]:

$$\underline{J}_n = -qn\underline{v}_n \tag{7}$$

$$\underline{J}_p = qp\underline{v}_p \tag{8}$$

where $\underline{v}_n$ and $\underline{v}_p$ are the electron type and hole type carrier speeds. Therefore, the correct carrier speeds are:

$$\underline{v}_n = -\frac{1}{qn}\underline{J}_n \tag{9}$$

$$\underline{v}_p = \frac{1}{qp}\underline{J}_p \tag{10}$$

where $\underline{J}_n$ and $\underline{J}_p$ are given by (5) and (6). Please note that (9) and (10) will be very useful in the next section for the development of a suitable model.

Another not negligible consequence of the second mistake is that the MR effect arises also when the applied voltage to the junction is zero (in other words the authors claim that the SCR configuration becomes trapezoidal under an ESMF even at zero bias), however this is not true. As a matter of fact, Lorentz's force acts on carriers only when they are in motion, i.e. when some current is flowing (thus only when some external voltage is applied to the junction and not when the junction is in thermal equilibrium).

1.5 Key information extracted from the examined literary review

On balance, what can be deducted from the available scientific literature is qualitatively how the static magnetic field affects the steady state performance of a semiconductor device from the standpoint of the direct action on the current carriers:

- An ESMF influences at least the conduction losses (please note that the consumption increase of a semiconductor device permeated by a static magnetic field is also made known in many ITER reports after some experimental tests on electronics).
- An ESMF gives rise to a non-uniform current distribution in the device, leading to hotspots.

On the contrary, what cannot be inferred by analyzing the available scientific literature is:

- How an ESMF affects the dynamic performance of a semiconductor device (for instance turning on/off times could be affected, switching losses are also highly likely affected too, etc.)

2 Modeling the interaction between a static magnetic field and semiconductor devices

This section presents the mathematical models describing the effect of a static magnetic field on solid state technology, in particular, two approaches are presented: the first one is a general approach based on a first order perturbation of the electron (or hole) distribution function in the Boltzman Transport Equation for non equilibrium conditions, to include higher order magnetic field effects. The second one is based on a Lorentz's force approach, it is interesting to notice that after some simplifications, the model given by the former approach is equal to the one given by the latter.

2.1 Magnetic carrier transport equations

The models hereby presented were developed to study, optimize and design semiconductor magnetosensors; however, although this is the only use that has been made so far of such tools, it does not mean that it is the only possible one. As a matter of fact, the models are totally general and just by properly tuning some parameters, boundary conditions etc. they can represent every semiconductor device.

The main references providing a detailed analysis are: [12-19]. All the mathematical analysis is here omitted and just the key points are described.

Essentially, using microscopic transport theory the general form of the carrier transport equations in the presence of an ESMF is derived. As previously mentioned, the derivation is based on a first order perturbation of the electron (or hole) distribution function in the Boltzman Transport Equation for non equilibrium conditions, to include higher order magnetic field effects. After that, two possibilities appear:

1. A series expansion of the magnetic field in the perturbation function is employed to yield galvanomagnetic transport coefficient that are magnetic field independent.
2. A series expansion is directly employed in the galvanomagnetic transport coefficient in order to take into account the magnetic field dependence of such parameters.

It is important to notice that model 1. (which is simpler) is usually implemented in commercial softwares (ATLAS or SENTAURUS DEVICE [20, 21]).

The entire discussion is restricted to so-called "weak field" limit, i.e. $\left(\mu_{n,p}B\right)^2 \ll 1$, where $\mu_{n,p}$ is the electron/hole mobility and B is the intensity of the magnetic

induction. That has different implications depending on different materials, for instance with n-type silicon, typically one has $\mu_n = 0.14\ m^2/Vs$, therefore B can be as high as $2.2\ T$. Besides, real mobility values are usually lower than rated values because of different phenomena such as lattice scattering (i.e. temperature dependence), impurity scattering, carrier scattering etc. Thus, the admissible value of the magnetic induction can be even higher for the model to be still reliable. In any case, a value of $2.2\ T$ is already significantly higher than the maximum magnetic intensity predicted to arise in the crane hall of the Tokamak building.

Please be aware that the general derivation procedure of the transport equation is treated formally in [12] and outlined in [14] for an easier understanding.

2.1.1 Transport coefficients independent of the magnetic field

The final result of possibility 1. (i.e. magnetic field independent transport equation coefficient) is given by the following generalized continuity equations:

$$\underline{J}_n + \mu_{Hn}\underline{J}_n \times \underline{B} = q\mu_n n\nabla\Phi_n \tag{11}$$

$$\underline{J}_p - \mu_{Hp}\underline{J}_p \times \underline{B} = -q\mu_p p\nabla\Phi_p \tag{12}$$

Where ϕ_n and ϕ_p are the electron and hole quasi-Fermi potential, n and p are the electron and hole concentration respectively, q is the elementary charge, $\underline{B}$ is the magnetic induction vector, μ_n and μ_p are the electron and hole mobility respectively and $\underline{J}_n$ and $\underline{J}_p$ are the electron and hole current density.

If the Fermi energies are sufficiently far from band edges, Boltzmann statistics can be employed to yield simple expressions for $\phi_{n,p}$ in terms of the carrier concentrations and the electrostatic potential φ [14]:

$$\Phi_n = \varphi - \frac{kT}{q}\ln\left(\frac{n}{n_i}\right) \tag{13}$$

$$\Phi_p = \varphi + \frac{kT}{q}\ln\left(\frac{p}{n_i}\right) \tag{14}$$

Where k is the Boltztman's quantity, T is the absolute temperature and n_i is the intrinsic concentration. Substituting (11) in (13) and (12) in (14) one has after some passages the final form of the transport equations:

$$\underline{J}_n + \mu_{Hn}\underline{J}_n \times \underline{B} = q\left[D_n\nabla n - \mu_n n\nabla\varphi\right] \tag{15}$$

$$\underline{J}_p - \mu_{Hp}\underline{J}_p \times \underline{B} = -q\left[D_p \nabla p + \mu_p p \nabla \varphi\right] \tag{16}$$

Where μ_{Hn} and μ_{Hp} are the electron and hole Hall mobility respectively, D_n and D_p are the electron and hole diffusion coefficients defined as:

$$D_n = \frac{kT\mu_n}{q} \quad , \quad D_p = \frac{kT\mu_p}{q} \tag{17}$$

After some tedious mathematical passages equations in (15) can be rearranged as follows:

$$\underline{J}_n = \mathbf{M}_{BH,n}\underline{J}_{ns} \tag{18}$$

$$\underline{J}_p = \mathbf{M}_{BH,p}\underline{J}_{ps} \tag{19}$$

where:

$$\underline{J}_{ns} = q\left(D_n \nabla n - \mu_n n \nabla \varphi\right) \tag{20}$$

$$\underline{J}_{ps} = -q\left(D_p \nabla p + \mu_p p \nabla \varphi\right) \tag{21}$$

are the "standard" forms of the current densities in semiconductor devices when no magnetic field is present. Besides, matrices $\boldsymbol{M}_{BH,n}$ and $\boldsymbol{M}_{BH,p}$ read:

$$\mathbf{M}_{BH,n} = \frac{1}{\mu_{Hn}^2\left(B_x^2 + B_y^2 + B_z^2\right)+1}\begin{bmatrix} \mu_{Hn}^2 B_x^2 + 1 & -\mu_{Hn}\left(B_z - \mu_{Hn}B_xB_y\right) & \mu_{Hn}\left(B_y + \mu_{Hn}B_xB_z\right) \\ \mu_{Hn}\left(B_z + \mu_{Hn}B_xB_y\right) & \mu_{Hn}^2 B_y^2 + 1 & -\mu_{Hn}\left(B_x - \mu_{Hn}B_yB_z\right) \\ -\mu_{Hn}\left(B_y - \mu_{Hn}B_xB_z\right) & \mu_{Hn}\left(B_x + \mu_{Hn}B_yB_z\right) & \mu_{Hn}^2 B_z^2 + 1 \end{bmatrix} \tag{22}$$

$$\mathbf{M}_{BH,p} = \frac{1}{\mu_{Hp}^2\left(B_x^2 + B_y^2 + B_z^2\right)+1}\begin{bmatrix} \mu_{Hp}^2 B_x^2 + 1 & \mu_{Hp}\left(B_z + \mu_{Hp}B_xB_y\right) & -\mu_{Hp}\left(B_y - \mu_{Hp}B_xB_z\right) \\ -\mu_{Hp}\left(B_z - \mu_{Hp}B_xB_y\right) & \mu_{Hp}^2 B_y^2 + 1 & \mu_{Hp}\left(B_x + \mu_{Hp}B_yB_z\right) \\ \mu_{Hp}\left(B_y + \mu_{Hp}B_xB_z\right) & -\mu_{Hp}\left(B_x - \mu_{Hp}B_yB_z\right) & \mu_{Hp}^2 B_z^2 + 1 \end{bmatrix} \tag{23}$$

In which B_x, B_y and B_z are the x, y, and z components of the magnetic induction vector. Besides, one has:

$$\mu_{Hn} = r_n \mu_n \tag{24}$$

$$\mu_{Hp} = r_p \mu_p \tag{25}$$

Common values for r_n and r_p are [16]:

$$r_n = 1.1 \quad , \quad r_p = 0.7 \tag{26}$$

On balance, the complete model reads:

$$\boxed{\begin{aligned} \nabla \cdot \nabla \varphi &= \frac{q}{\varepsilon}\left(n - p - C\right) \\ \frac{\partial n}{\partial t} - \nabla \cdot \left[\mathbf{M}_{BH,n}\left(D_n \nabla n - n\mu_n \nabla \varphi\right)\right] &= -R \\ \frac{\partial p}{\partial t} + \nabla \cdot \left[\mathbf{M}_{BH,p}\left(D_p \nabla p + p\mu_p \nabla \varphi\right)\right] &= -R \end{aligned}} \tag{27}$$

Please note that the Poisson's equation is only indirectly affected by the magnetic field since its time derivative is assumed to be either zero or negligible.

Where the dependent variables are given by the set φ, n, p.

As regards the symbols which has not been defined already one has: ε is the dielectric constant of the material, C is the dopant concentration and R represent the recombination rate. Numerous phenomena affect the latter quantity, however, the dominant recombination mechanism in silicon is the so called "Shockley-Read-Hall process" [22], which is well modeled by the following expression:

$$R = \frac{np - n_i^2}{\tau_p\left(n + n_i\right) + \tau_n\left(p + n_i\right)} \tag{28}$$

In which τ_p and τ_n are the hole and electron lifetime respectively.

2.1.2 Magnetic field dependent transport coefficients

If one prefers to consider the effect of the ESMF, not only on the moving carriers, but also on the material properties, then the transport coefficient dependence on the magnetic field must not be neglected.

The mathematical derivation of the final equations is even more complicated and it is described in detail in [13, 14]. Here a further simplification is proposed in order to obtain the same structure of equations (15) but with magnetic field dependent parameters.

Since this simplification is not presented in the analysed documents, it is described in the following. The derivation is carried out for only for electrons for brevity's sake; the exact same procedure can be applied to the hole equation too.

The final continuity equation presented in the cited documents reads:

$$\underline{J}_n = -\left(K_1 + K_2\underline{B}\times + K_3\underline{B}\underline{B}\cdot\right)\nabla\Phi_n \tag{29}$$

Which can be written as follows in order to avoid confusion of notation:

$$\underline{J}_n = -K_1\nabla\Phi_n - K_2\underline{B}\times\nabla\Phi_n - K_3\underline{B}\underline{B}\cdot\nabla\Phi_n \tag{30}$$

Where in general K_1, K_2 and K_3 are magnetic field dependent tensors. However, according to [13], these transport coefficients reduce to scalars in materials like Silicon and Germanium because "*several non-spherical constant energy surfaces are symmetrically arranged in the k space"*.

Assuming the worst operating condition to take place for the device, i.e. $\underline{B}$ perpendicular to the current flow, then $\underline{B}\cdot\nabla\phi_n \cong 0$ since the angle between $\nabla\phi_n$ and $\underline{J}_n$ is exactly zero when no ESMF is applied and it remains very small even in the presence of an ESMF. Thanks to this assumption (30) becomes:

$$\underline{J}_n = -K_1\nabla\Phi_n - K_2\underline{B}\times\nabla\Phi_n \tag{31}$$

and multiplying both sides of (30) by $\frac{K_2}{K_1}\underline{B}\times$ one obtains:

$$\frac{K_2}{K_1}\underline{B}\times\underline{J}_n = -K_1\frac{K_2}{K_1}\underline{B}\times\nabla\Phi_n - K_2\frac{K_2}{K_1}\underline{B}\times\underline{B}\times\nabla\Phi_n \tag{32}$$

Excluding the quadratic term in the magnetic field (as proposed in [23]) one has:

$$-K_2\underline{B}\times\nabla\Phi_n = \frac{K_2}{K_1}\underline{B}\times\underline{J}_n \tag{33}$$

Substituting (33) in (31) one obtains:

$$\underline{J}_n = -K_1\nabla\Phi_n + \frac{K_2}{K_1}\underline{B}\times\underline{J}_n \tag{34}$$

In particular, from [13, 14] the transport coefficients are:

$$K_2 / K_1 = \mu_{Hn}\left(B\right) = \mu_{Hn0}\left[1 - \beta\left(\mu_{Hn0}B\right)^2\right] \tag{35}$$

$$K_1 = \sigma_{Hn}\left(B\right) = q\mu_n n\left[1-\left(\mu_{Hn0}B\right)^2\right] \tag{36}$$

Where μ_{Hn0} is the electron Hall mobility at zero magnetic field, computed according to (24), B is the magnetic induction intensity, i.e. $B = \sqrt{B_x^2 + B_y^2 + B_z^2}$ and a common number for β is 1.26 [13, 14]. Therefore, the final form of the electron continuity equation with magnetic field dependent coefficients is obtained replacing (35) and (36) in (34):

$$\underline{J}_n + \mu_{Hn}\left(B\right)\underline{J}_n \times \underline{B} = -\sigma_{Hn}\left(B\right)\nabla\Phi_n \tag{37}$$

It is immediate to note that (37) and (11) have an identical structure, in particular (37) considers the effect of the magnetic field on the material properties, i.e. on the transport coefficients.

$$\underline{J}_p - \mu_{Hp}\left(B\right)\underline{J}_p \times \underline{B} = -\sigma_{Hp}\left(B\right)\nabla\Phi_p \tag{38}$$

$$\mu_{Hp}\left(B\right) = \mu_{Hp0}\left[1-\beta\left(\mu_{Hp0}B\right)^2\right] \tag{39}$$

$$\sigma_{Hp}\left(B\right) = q\mu_{Hp}p\left[1-\left(\mu_{Hp0}B\right)^2\right] \tag{40}$$

The hole equation can be derived in the exact same way leading to another identical equation to (12) as far as the structure is concerned.

Finally, the resulting model remains formally unchanged with respect to (27).

2.2 Drift-diffusion model of a semiconductor device permeated by a constant magnetic field – construction via a Lorentz's force approach

The Drift Diffusion (DD) model is the most common mathematical approach for the study of semiconductor devices, especially in industrial simulations [24]. The aim of this section is to generalize the standard DD model in order to consider also the contribution of an ESMF (the resulting model is therefore called "Generalized Drift Diffusion" (GDD) model). The generalisation of the standard DD model is obtained applying Lorentz's force to the already known semiconductor equations to include the effect of the magnetic field.

Please note that the theoretical basis for the subsequent discussion are mainly provided by the following textbooks or papers: [11], [24], [10], [25], [22], [26].

2.2.1 Complete generalized drift diffusion model

The starting point of this analysis is given by the Maxwell's equations, which in the differential form read:

$$\nabla \times \underline{E} = -\frac{\partial \underline{B}}{\partial t} \tag{41}$$

$$\nabla \times \underline{H} = \underline{J} + \frac{\partial \underline{D}}{\partial t} \tag{42}$$

$$\nabla \cdot \underline{D} = \rho \tag{43}$$

$$\nabla \cdot \underline{B} = 0 \tag{44}$$

Also the constitutive laws characterizing the electromagnetic properties of the material must be mentioned:

$$\underline{D} = \varepsilon \underline{E} \tag{45}$$

$$\underline{B} = \mu_m \underline{H} \tag{46}$$

Where ε is the material dielectric permittivity $[Fm^{-1}]$ and μ_m is the magnetic permeability $[Hm^{-1}]$. Assuming a time-invariant magnetic field $\underline{B}$, (41) becomes:

$$\nabla \times \underline{E} = \underline{0} \tag{47}$$

Thus, there exists a scalar potential φ such that:

$$\underline{E} = -\nabla \varphi \tag{48}$$

Applying the divergence operator to (48) and thanks to (45) one obtains:

$$\nabla \cdot \nabla \varphi = -\frac{\rho}{\varepsilon} \tag{49}$$

Which is the *Poisson's equation*. In addition, applying the divergence operator to (42) one has:

$$\nabla \cdot \left(\nabla \times \underline{H} \right) = \nabla \cdot \left(\underline{J} + \frac{\partial \underline{D}}{\partial t} \right) \tag{50}$$

It is well known that the divergence of the curl of any vector field is identically zero, therefore, replacing (43) in (50), one obtains the *continuity equation*:

$$\nabla \cdot \underline{J} + \frac{\partial \rho}{\partial t} = 0 \tag{51}$$

It is important at this point to specify the mathematical form of the charge density ρ:

$$\rho = \underbrace{q\left(p - n\right)}_{\rho_{free}} + \underbrace{qC}_{\rho_{fixed}} \tag{52}$$

Where $n = n(x, y, z, t)$, $p = p(x, y, z, t)$ and $C = C(x, y, z)$ are the electron, hole and doping concentrations respectively, while q is the elementary charge. For instance, in 1 step 1d or 2d p-n junction C reads:

$$C = \frac{1}{2}\left(N_d - N_a + \left(N_d + N_a\right) sign\left(x\right)\right) \tag{53}$$

leading to the following charge distribution:

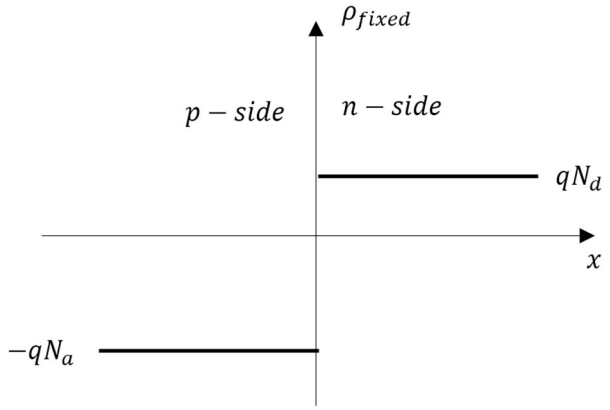

Fig. 5 Doping concentration in a 1-dimensional step p-n junction

(N_a is concentration of "acceptor atoms" while N_d is the concentration of "donor atoms"). Since two different type of carriers are defined (i.e. holes and electrons), it is very useful to split the total current density into their separate contributions:

$$\underline{J} = \underline{J}_n + \underline{J}_p \tag{54}$$

Substituting (52) and (54) in (51), the doping concentration being time-constant, one has:

$$\nabla \cdot \left(\underline{J}_n + \underline{J}_p\right) + q\frac{\partial\left(p - n\right)}{\partial t} = 0 \tag{55}$$

Introducing the arbitrary function $R = R(n,p)$, equation (55) can be split in 2 equations as follows:

$$-q\frac{\partial n}{\partial t} + \nabla \cdot \underline{J}_n = qR \tag{56}$$

$$q\frac{\partial p}{\partial t} + \nabla \cdot \underline{J}_p = -qR \tag{57}$$

Where R can be considered as the net rate of generation and recombination of holes and electrons. It is still necessary to explicitly express the current densities as a function of the hole and electron concentration and the electric potential. It is also important at this stage to take into account the presence of an ESMF, therefore, the drift components of the current densities are not only given by the electric field but by the Lorentz's force in general, namely:

$$\underline{J}_n = q\mu_n n\left(\underline{E} + \underline{v}_n \times \underline{B}\right) + qD_n \nabla n \tag{58}$$

$$\underline{J}_p = q\mu_p p\left(\underline{E} + \underline{v}_p \times \underline{B}\right) - qD_p \nabla p \tag{59}$$

Where $\underline{B} = \underline{B}(x,y,z)$ is in general assumed to be constant and non-uniform. Thanks to (9) and (10) relations (58) and (59) read:

$$\underline{J}_n = \mu_n\left(qn\underline{E} - \underline{J}_n \times \underline{B}\right) + qD_n \nabla n \tag{60}$$

$$\underline{J}_p = \mu_p\left(qp\underline{E} + \underline{J}_p \times \underline{B}\right) - qD_p \nabla p \tag{61}$$

Explicitly computing the vector products in (60) one has:

$$\begin{cases} J_{nx} = -\mu_n\left(B_z J_{ny} - B_y J_{nz} + qnE_x\right) - qD_n\dfrac{\partial n}{\partial x} \\ J_{ny} = -\mu_n\left(B_x J_{nz} - B_z J_{nx} + qnE_y\right) - qD_n\dfrac{\partial n}{\partial y} \\ J_{nz} = -\mu_n\left(B_y J_{nx} - B_x J_{ny} + qnE_z\right) - qD_n\dfrac{\partial n}{\partial z} \end{cases} \tag{62}$$

Where $J_{nx},\ J_{ny},\ J_{nz}$ are the electron current density components, E_x, E_y, E_z are the electric field components while B_x, B_y, B_z are the magnetic field components. In other terms:

$$\underline{J}_n = \left[J_{nx}\ ,\ J_{ny}\ ,\ J_{nz}\right]^T \tag{63}$$

$$\underline{E} = \left[E_x \, , E_y \, , E_z \right]^T \tag{64}$$

$$\underline{B} = \left[B_x \, , B_y \, , B_z \right]^T \tag{65}$$

$$\nabla n = \left[\frac{\partial n}{\partial x} , \frac{\partial n}{\partial y} , \frac{\partial n}{\partial z} \right]^T \tag{66}$$

A very similar set of equations can be obtained for holes (i.e. from (61)). Solving the system of equations (62) for J_{nx}, J_{ny}, J_{nz} and rearranging the solution in the matrix form, one obtains:

$$\underline{J}_n = \mathbf{M}_{B,n} \left(q\mu_n n \underline{E} + qD_n \nabla n \right) \tag{67}$$

Where $\boldsymbol{M}_{B,n}$ reads:

$$\mathbf{M}_{B,n} = \frac{1}{\mu_n^2 \left(B_x^2 + B_y^2 + B_z^2 \right) + 1} \begin{bmatrix} \mu_n^2 B_x^2 + 1 & -\mu_n \left(B_z - \mu_n B_x B_y \right) & \mu_n \left(B_y + \mu_n B_x B_z \right) \\ \mu_n \left(B_z + \mu_n B_x B_y \right) & \mu_n^2 B_y^2 + 1 & -\mu_n \left(B_x - \mu_n B_y B_z \right) \\ -\mu_n \left(B_y - \mu_n B_x B_z \right) & \mu_n \left(B_x + \mu_n B_y B_z \right) & \mu_n^2 B_z^2 + 1 \end{bmatrix} \tag{68}$$

the hole current density is obtained in a similar fashion:

$$\underline{J}_p = \mathbf{M}_{B,p} \left(q\mu_p p \underline{E} - qD_p \nabla p \right) \tag{69}$$

Where:

$$\mathbf{M}_{B,p} = \frac{1}{\mu_p^2 \left(B_x^2 + B_y^2 + B_z^2 \right) + 1} \begin{bmatrix} \mu_p^2 B_x^2 + 1 & \mu_p \left(B_z + \mu_p B_x B_y \right) & -\mu_p \left(B_y - \mu_p B_x B_z \right) \\ -\mu_p \left(B_z - \mu_p B_x B_y \right) & \mu_p^2 B_y^2 + 1 & \mu_p \left(B_x + \mu_p B_y B_z \right) \\ \mu_p \left(B_y + \mu_p B_x B_z \right) & -\mu_p \left(B_x - \mu_p B_y B_z \right) & \mu_p^2 B_z^2 + 1 \end{bmatrix} \tag{70}$$

It is now possible to write all the model equations, in particular, let us summarize the necessary equations: (49), (56) and (57) which read:

$$\begin{cases} \nabla \cdot \nabla \varphi = -\dfrac{\rho}{\varepsilon} \\ -q \dfrac{\partial n}{\partial t} + \nabla \cdot \underline{J}_n = qR \\ q \dfrac{\partial p}{\partial t} + \nabla \cdot \underline{J}_p = -qR \end{cases} \tag{71}$$

The only missing information so far is how to properly model the recombination/generation rate R. It is important to keep in mind that electrons and holes are in continuous fluctuations due to their thermal energy, the macroscopic result is that the net recombination rate at equilibrium is identically zero. Our interest is to analyze the deviation from this condition. While generation events are usually due to thermal agitation or an external input source (applied voltage, light etc.), the recombination events happen in order to neutralize an excess of charge.

The phenomenological model for the net recombination rate is often given in the following form:

$$R(n,p) = \left(np - n_i^2\right) F(n,p) \tag{72}$$

Where n_i is the "intrinsic concentration" and it is a temperature dependent parameter, while F is a function accounting for specific recombination events. The function F is given by different contributions, however, in silicon the dominant recombination mechanism can be modelled as follows [22] (Shockley Read Hall recombination process):

$$F(n,p) = \frac{1}{\tau_p\left(n + n_i\right) + \tau_n\left(p + n_i\right)} \tag{73}$$

where τ_n and τ_p are the electron and hole lifetime respectively.

Inserting the expression of the charge density (52) into the first of (71), the expression of the current densities (67) and (69) into the second and the third equations respectively of (71) one finally achieves, after some passages, a dynamic 3-dimensional model of a semiconductor device permeated by an ESMF:

$$\boxed{\begin{aligned} \nabla\cdot\nabla\varphi &= \frac{q}{\varepsilon}\left(n - p - C\right) \\ \frac{\partial n}{\partial t} - \nabla\cdot\left[\mathbf{M}_{B,n}\left(D_n\nabla n - n\mu_n\nabla\varphi\right)\right] &= -\frac{np - n_i^2}{\tau_p\left(n + n_i\right) + \tau_n\left(p + n_i\right)} \\ \frac{\partial p}{\partial t} + \nabla\cdot\left[\mathbf{M}_{B,p}\left(D_p\nabla p + p\mu_p\nabla\varphi\right)\right] &= \frac{np - n_i^2}{\tau_p\left(n + n_i\right) + \tau_n\left(p + n_i\right)} \end{aligned}} \tag{74}$$

In particular, such model is a 3-dimensional (i.e. $\varphi = \varphi(x,y,z), n = n(x,y,z), p = p(x,y,z)$) and a 3 Partial Differential Equations (PDE) model in the variables $\{\varphi, n, p\}$. Specifically, two of these equations are time-varying, and all of them are highly non-linear and strongly coupled with one another. In summary, they represent an extremely tough set of equations to be solved.

Moreover, it is fundamental to notice that if there is no ESMF, one has:

$$\mathbf{M}_{Bn,p}\Big|_{\underline{B}=\underline{0}} = \begin{bmatrix} 1 & 0 & 0 \\ 0 & 1 & 0 \\ 0 & 0 & 1 \end{bmatrix} \tag{75}$$

Thus, the resulting model becomes the standard DD model commonly used for semiconductor device simulations [24].

It is very interesting to notice that the models (74) and (27) are formally identical and in particular, the matrices (68) and (70) are equals to (22) and (23) respectively if μ_{Hn} and μ_{Hp} are replaced by μ_n and μ_p.

It is natural at this point to wonder if a solution to this model exists and if so, whether it is unique or not. The question about existence of solutions of the basic semiconductor equations with their associated boundary conditions for a specific device is important only from a mathematical standpoint. Physically, of course, solutions obviously exist. However, since the equations are models they are never exactly correct. How well posed mathematically a model is, gives in some sense a measure of the quality of the model. For instance, if one has a mathematical proof that no solutions exist for some model, this in general indicates that the model is wrong.

A very interesting discussion on the existence and uniqueness of the solution can be found in [24], besides more references to other works concerning this problem can be found there. Suffice it to say that no proofs are available both for the existence and uniqueness in the general case, however, these properties can be analytically shown if some more restrictive hypotheses on the model are assumed.

As a final remark, it is of primary importance to notice that the basic semiconductor equations only constitute a time dependent problem if the boundary condition for the electric potential is time dependent. If the boundary condition for the electrostatic potential is time invariant, the semiconductor equations reduce to a system of three coupled elliptic equations.

2.3 Adopted model

2.3.1 Simplifications

In order to be able to perform the necessary simulations and still obtain meaningful results some approximations have to be made to the proposed model:

1. The first one consists of reducing (74) to a 2-dimensional model, in order to do that one must assumes that $\underline{B}$ is only in the z-direction, namely:

$$\underline{B}(x,y)=\left[0,0,B_z(x,y)\right]^T \tag{76}$$

In addition, assuming also that:

$$\underline{J}_n(x,y)=\left[J_{nx}(x,y),J_{ny}(x,y),0\right]^T \tag{77}$$

$$\underline{J}_p(x,y)=\left[J_{px}(x,y),J_{py}(x,y),0\right]^T \tag{78}$$

$$n=n(x,y) \tag{79}$$

$$p=p(x,y) \tag{80}$$

$$\varphi=\varphi(x,y) \tag{81}$$

Therefore, after these assumptions (74) is formally unchanged, however, φ, n and p are functions only of x and y, while $\boldsymbol{M}_{Bn}$ and $\boldsymbol{M}_{Bp}$ become:

$$\mathbf{M}_{Bn}(x,y)=\frac{1}{1+\mu_{nH}^2B_z^2(x,y)}\begin{bmatrix}1 & -\mu_{nH}B_z(x,y)\\ \mu_{nH}B_z(x,y) & 1\end{bmatrix} \tag{82}$$

$$\mathbf{M}_{Bp}(x,y)=\frac{1}{1+\mu_{pH}^2B_z^2(x,y)}\begin{bmatrix}1 & \mu_{pH}B_z(x,y)\\ -\mu_{pH}B_z(x,y) & 1\end{bmatrix} \tag{83}$$

2. Another further simplification is to consider $\underline{B}$ uniform, hence, the entries of the matrices $\boldsymbol{M}_{Bn}$ and $\boldsymbol{M}_{Bp}$ become constant (B being the constant value of the z component of the magnetic induction):

$$\mathbf{M}_{Bn}=\frac{1}{1+\mu_{Hn}^2B^2}\begin{bmatrix}1 & -\mu_{Hn}B\\ \mu_{Hn}B & 1\end{bmatrix} \tag{84}$$

$$\mathbf{M}_{Bp}=\frac{1}{1+\mu_{Hp}^2B^2}\begin{bmatrix}1 & \mu_{Hp}B\\ -\mu_{Hp}B & 1\end{bmatrix} \tag{85}$$

Please notice that the Hall mobilities have been chosen in the matrices containing the static magnetic field coefficients instead of the "simple

mobilities". Thus, the magnetic carrier transport equation approach is chosen, due to its higher generality and more solid theoretical foundation compared to the Lorentz's force approach.

3. In addition, only the steady state behaviour is of interest in this study, hence, the time derivatives of the electron and hole concentrations must be neglected:

$$\frac{\partial n}{\partial t} = 0 \tag{86}$$

$$\frac{\partial p}{\partial t} = 0 \tag{87}$$

From a mathematical point of view, it is clear that the effect of an external magnetic field is to couple the x-axis, y-axis and z-axis continuity equations with one another, both for electrons and holes. In absence of any magnetic field the different axis equations are totally decoupled (see relation (75)).

Therefore, the model chosen for the analysis, at least for a preliminary study, is a 2-dimensional, steady state model with transverse constant magnetic field and a recombination rate dominated by the Shockley Read Hall process.

Thus, let us recall such model:

$$\boxed{\begin{array}{c} \nabla \cdot \nabla \varphi = \frac{q}{\varepsilon}\left(n - p - C\right) \\ \nabla \cdot \underline{J}_n = R \\ \nabla \cdot \underline{J}_p = -R \end{array}} \tag{88}$$

Where $n = n(x,y), p = p(x,y)$ and $\varphi = \varphi(x,y)$ are the dependent variables and in particular they are the electron concentration in $[m^{-3}]$, the hole concentration in $[m^{-3}]$ and the electric voltage in $[V]$ respectively. Whereas, q is the elementary charge, ε is the dielectric constant of the material, $C = C(x,y)$ is the dopant concentration in $[m^{-3}]$, R is the recombination rate and $\underline{J}_n = \left[J_{nx}, J_{ny}\right]^T$ and $\underline{J}_p = \left[J_{px}, J_{py}\right]^T$ are the electron and hole current density in $[A/cm^2]$ defined as:

$$\underline{J}_n = \mathbf{M}_{B,n}\underline{J}_{ns} \tag{89}$$

$$\underline{J}_p = \mathbf{M}_{B,p}\underline{J}_{ps} \tag{90}$$

Where:

$$\mathbf{M}_{B,n} = \frac{1}{1+\mu_{nH}^2 B^2}\begin{bmatrix} 1 & -\mu_{nH}B \\ \mu_{nH}B & 1 \end{bmatrix} \tag{91}$$

$$\mathbf{M}_{B,p} = \frac{1}{1+\mu_{pH}^2 B^2}\begin{bmatrix} 1 & \mu_{pH}B \\ -\mu_{pH}B & 1 \end{bmatrix} \tag{92}$$

In which B is the intensity of the magnetic induction in $[T]$, where $\underline{B}_{ext} = [0,0,B]^T$, whereas μ_{nH} and μ_{pH} are the Hall electron and hole mobility respectively and $\underline{J}_{ns} = \left[J_{nxs}, J_{nys}\right]^T$ and $\underline{J}_{ps} = \left[J_{pxs}, J_{pys}\right]^T$ are the "standard" electron and hole current density (i.e. the current density when no magnetic field is present). In particular, they are defined as:

$$\underline{J}_{ns} = -q\left(\mu_n n\nabla\varphi - D_n\nabla n\right) \tag{93}$$

$$\underline{J}_{ps} = -q\left(\mu_p p\nabla\varphi + D_p\nabla p\right) \tag{94}$$

Where μ_n and μ_p are the electron and hole mobility and D_n and D_p are the electron and hole diffusion coefficients. Among the parameters $\mu_{n(p)}$, $\mu_{nH(pH)}$ and $D_{n(p)}$ the following relations hold:

$$\mu_{nH(pH)} = r_{n(p)}\mu_{n(p)} \tag{95}$$

$$D_{n(p)} = \frac{kT}{q}\mu_{n(p)} \tag{96}$$

Where $r_{n(p)}$ are constant parameters, k is the Boltzmann's constant and T is the absolute temperature. Finally, many models for the recombination rate R are available, the following form is adopted:

$$R = \frac{np - n_i^2}{\tau_p\left(n+n_i\right)+\tau_n\left(p+n_i\right)} \tag{97}$$

Finally, the choice of the function C (together with the boundary conditions) defines which semiconductor device is under study. In this case the focus is on PN and PIN junctions (i.e. diodes) for reasons that are explained further on.

Therefore, depending on what kind of diode is selected for the study, the function C will describe its dopant concentration distribution in the silicon wafer.

2.3.2 Boundary conditions

Finally, the boundary conditions must be specified.

Choosing a rectangular geometry, which is a good 2D approximation of a diode, four sides can be identified:

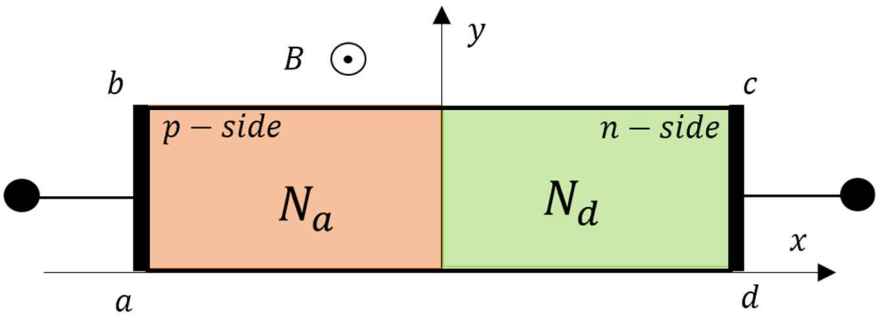

Fig. 6 2-dimensional rectangular step p-n junction

A simplified version of the boundary conditions for the electron and hole continuity equations on the insulated sides (i.e. the b-c and d-a sides) is given in the following:

$$\underline{J_n} \cdot \underline{\eta} = 0 \tag{98}$$

$$\underline{J_p} \cdot \underline{\eta} = 0 \tag{99}$$

Where $\underline{\eta}$ is the normal vector to the boundary line (or surface in the 3-dimensional case). More information on the conditions (98) and (99)-and their more sophisticated versions can be found in [24]. Besides, the boundary condition on the insulated side for the Poisson's equation is detailed in the next subsection.

As far as the metallic contacts (i.e. the "short" sides) are concerned, one has for the electric potential:

$$\varphi_{ab} = 0 \tag{100}$$

$$\varphi_{cd} = V_0 - V_s + V_{applied} \tag{101}$$

Where $V_{applied}$ denotes the externally applied voltage; V_s represents the Schottky barrier height, which is a characteristic quantity of the metal and the semiconductor with which the Schottky contact is fabricated. The numerical value of V_s is usually between half a volt and one volt. V_0 is the built-in potential (the potential generated by the p-n junction in thermal equilibrium) which, in this context is frequently omitted and implicitly accounted for with a properly adjusted value for V_s [24].

The boundary conditions for the carrier concentrations are obtained under the well-established hypothesis of thermal equilibrium and vanishing space charge at the

boundaries (i.e. at the ohmic contacts). These assumptions lead to the following relations:

$$np - n_i^2 = 0 \tag{102}$$

$$n - p - C = 0 \tag{103}$$

Solving (102) and (103) with respect to n and p one has:

$$n = \frac{\sqrt{C^2 + 4n_i^2} + C}{2} \tag{104}$$

$$p = \frac{\sqrt{C^2 + 4n_i^2} - C}{2} \tag{105}$$

Thus, if the p-side is on the negative x half-plane (see Fig. 6), one obtains:

$$n_{ab} = \frac{\sqrt{N_a^2 + 4n_i^2} - N_a}{2} \tag{106}$$

$$p_{ab} = \frac{\sqrt{N_a^2 + 4n_i^2} + N_a}{2} \tag{107}$$

$$n_{cd} = \frac{\sqrt{N_d^2 + 4n_i^2} + N_d}{2} \tag{108}$$

$$p_{cd} = \frac{\sqrt{N_d^2 + 4n_i^2} - N_d}{2} \tag{109}$$

2.3.3 Magnetic field dependent Boundary conditions

A further comment regarding the Neumann conditions (i.e. the boundary conditions on the insulating or "floating" boundaries) must be made here. Recalling such conditions, one has for the continuity equations:

$$\underline{J}_n \cdot \underline{\eta} = 0 \tag{110}$$

$$\underline{J}_p \cdot \underline{\eta} = 0 \tag{111}$$

Where $\underline{\eta}$ is the normal vector to the boundary line (surface). On the other hand, as regards Poisson's equation, a zero normal component of the electric field would be inconsistent with the presence of a Hall field [16, 17, 27], a zero-space-charge

variation would couple the electrons and hole concentrations at the boundaries too tightly. Two types of alternative boundary conditions can be found in literature, here the physics-based one proposed in [16] is chosen. After some tedious mathematical manipulations, a convenient form of such boundary conditions can be obtained as a function of the current densities and the magnetic field:

$$\frac{\partial \varphi}{\partial \underline{\eta}} = -\frac{\rho_{surf}}{\varepsilon} - \frac{1}{\sigma_{nH} + \sigma_{pH}} \left(\mu_{Hn} \underline{B} \times \underline{J}_{ns} + \mu_{Hp} \underline{B} \times \underline{J}_{ps} \right) \cdot \underline{\eta} \tag{112}$$

Where ρ_{surf} is the surface charge and:

$$\sigma_{nH} = qn\mu_{Hn} \quad , \quad \sigma_{pH} = qp\mu_{Hp} \tag{113}$$

In the special case of:

$$\underline{B} = \left[0, 0, B \right]^T \tag{114}$$

Then

$$\frac{\partial \varphi}{\partial \underline{\eta}} = -\frac{\rho_{surf}}{\varepsilon} - \frac{1}{\sigma_{nH} + \sigma_{pH}} \left(\mu_{Hn} B \left[-J_{nyS}, J_{nxS}, 0 \right] + \mu_{Hp} B \left[-J_{pyS}, J_{pxS}, 0 \right] \right) \cdot \underline{\eta} \tag{115}$$

If the floating boundaries are parallel to the x-axis:

$$\underline{\eta} = \left[0, \pm 1, 0 \right] \tag{116}$$

Hence, neglecting the surface charge:

$$\frac{\partial \varphi}{\partial \underline{\eta}} = \begin{cases} -\dfrac{B}{\sigma_{nH} + \sigma_{pH}} \left(\mu_{Hn} J_{nxS} + \mu_{Hp} J_{pxS} \right) \\ \dfrac{B}{\sigma_{nH} + \sigma_{pH}} \left(\mu_{Hn} J_{nxS} + \mu_{Hp} J_{pxS} \right) \end{cases} \tag{117}$$

2.3.4 Usage of the adopted model

After all the simplifications made to the complete model it is important to understand what still are the meaningful results that can be obtained from it.

Therefore, thanks to this model it is possible to:

- Identify the I-V characteristics of a 2d p-n junction for different values of B, where $B \in [10, 70]$ mT and of operating temperature $T \in [100, 150]$ °C.
- Investigate increased current density regions in steady state operations.

Thanks to the identification of the I-V characteristics it is straightforward to:

- Quantify the impact of external static magnetic field on the conduction losses of a simple pn-junction.
- Extract some very useful insights on how static magnetic field interacts with the electric behavior of semiconductor devices at a basic level.

Thanks to the investigation of increased current densities region critical local temperatures can be evaluated in steady state.

2.3.5 Model parameters

The basic semiconductor equations just determine the structure of the set of equations which have to be solved in order to simulate the internal behavior of a device. Any quantitative simulation of a device relies heavily on applicable models for the parameter involved in these equations. In addition, a mathematical characterization of the problem of solving the basic semiconductor equations is only feasible with at least qualitative knowledge of the associated parameters (e. g. sign, smoothness, order of magnitude).

Many models are available for the calculation of such parameters, however it is of primary importance to bear in mind that those models describe very complex phenomena, sometimes even at quantum level, it is thus imperative to consider these models only as a very rough estimate of the real quantities labelled as "parameters" (and anyway the best possible estimate available employing classical mathematics).

As a matter of fact, many sophisticated models are available in the complete review proposed by [24] in Chapter 4, however, they run the risk of representing mathematical abstractions bringing negligible added values to the overall semiconductor device modeling. This is the reason why the attention in this report is focused more on phenomenological models, which are much simpler from a mathematical point of view and they are "tuned" on the basis of experimental results.

The physical quantities modeled as parameters in the GDD model are listed in the following table:

Symbol	Name	Unit
μ_n, μ_p	Electron, hole mobility	$m^2/_{Vs}$
$\boldsymbol{\mu_{nH}, \mu_{pH}}$	Electron, hole Hall mobility	$m^2/_{Vs}$
D_n, D_p	Electron, hole diffusion coefficient	$m^2/_{s}$
τ_n, τ_p	Electron, hole lifetime	s
n_i	Intrinsic concentration	$no.\ of\ carriers/_{m^3}$

Tab. 1 Parameters of the DD model

The calculation of those parameters is detailed in the sections describing the simulations.

3 Solving the Semiconductor Equations Under the Effect of a Static Magnetic Field

3.1 Review of potentially suitable software programs available in ITER

Among all the software programs available in ITER, MATLAB and ANSYS appeared to be the only one potentially able to carry out this task. However, after some investigations, ANSYS appeared not be suitable for this purpose; firstly because ITER is not in possession of a valid license for the semiconductor module (RedHawk or Totem), secondly such modules do not seem to be able to simulate the effect of an ESMF on the device.

On the other hand, MATLAB being a general-purpose software, it provides a higher flexibility. Two possible paths can be taken:

1. The Partial Differential Equation (PDE) tool can be used.
2. A dedicated finite difference or finite element code can be developed.

Indeed, MATLAB provides the possibility of using the PDE tool, where in principle any kind of PDE can be implemented and solved in two dimensions. However, it was verified that such tool is unable at present to solve even the standard semiconductor equations and even with Mathworks' assistance. The main reason for such failure is probably the absence in this tool of a special discretizing technique which was developed on purpose for semiconductor equations.

As a matter of fact, this technique known as the "Gummel-Sharfetter's method" is widely employed by every software programs dedicated to semiconductor device simulations (COMSOL, ATLAS, SENTAURUS device, etc.) and it allows to satisfactorily solve semiconductor equations employing meshes formed by a reasonable number of points.

The following figure shows schematically the outcomes of the software programme investigation described above.

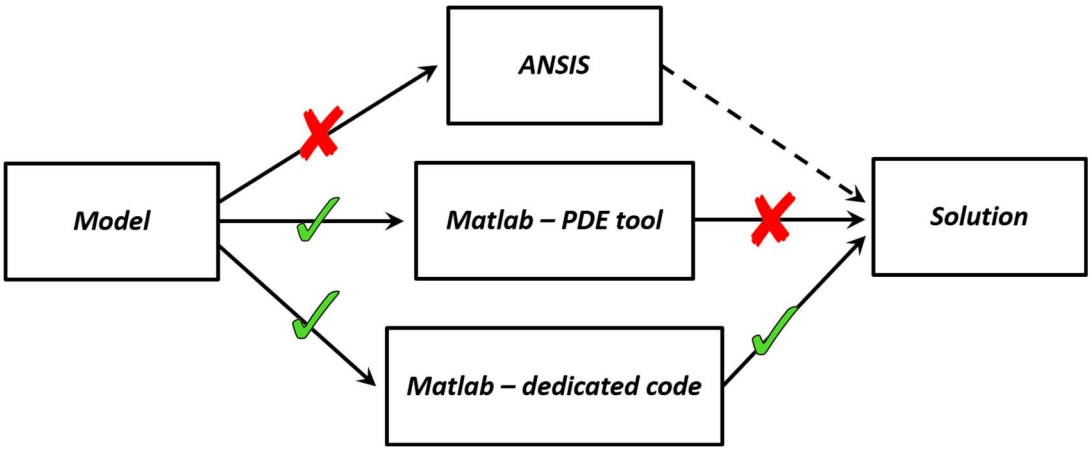

Fig. 7 Software program suitability investigation

On the other hand, Mathworks pointed out, after a direct inquiry, that their PDE tool is unable to solve even the standard semiconductor equations.

3.2 Simulation model

The purpose of this section is to present the model that has been implemented in the simulation code in order to better understand the obtained results. Indeed, in order to solve the equations of the complete modela very long time is required to properly develop the dedicated code. Therefore, some key simplifying assumptions must be made to minimize the complexity of the work in order to achieve some results in a reasonable time, both simplifying the geometry of the device and the structure of the equations.

Those necessary simplifying assumptions have been already presented in section 2.3 and are reported in the following for the clarity's sake.

3.2.1 Simplifying assumptions

The following simplifying assumptions have been made:

- The device is simulated in 2D on the x-y plane.
- The section geometry of the device is rectangular.
- The device is simulated in steady state.
- All the dependencies of the parameters on the variables n, p, φ (electron concentration, hole concentration and electric voltage) are neglected, therefore, such parameters are assumed to be constant.
- The temperature is assumed to be uniform throughout the device.
- The magnetic field is assumed to be uniform and parallel to the z-axis.
- The device considered is a diode.

It is important to notice that these assumptions are somehow coherent with another, i.e. a rectangular geometry is a good approximation in simulating a diode, a uniform temperature is a good approximation in steady state operating conditions as the current density is supposed to uniform in the device and finally, the assumption related to the magnetic field is a conservative assumption as conservative will be the values chosen for the parameters assumed to be constant.

Besides, it is fundamental to understand that although the device under consideration is a diode (i.e. a simple PN junction in signal applications and a PIN junction in power applications) the results obtained are significant also for other types of semiconductor devices in general (especially thyristors) operating in steady state. As a matter of fact, either the PN or the PIN junction is the basic element of every solid state device. However, it cannot be stated the same is true in a dynamic operating condition, where each case should be addressed independently.

3.2.2 Model

Again, the adopted model is described in section 2.3, however it is reported here for clarity's sake.

After all the simplifications described in the previous subsection, the model in the compact form reads:

$$\boxed{\begin{aligned} \nabla\cdot\nabla\varphi &= \frac{q}{\varepsilon}\left(n-p-C\right) \\ \nabla\cdot\underline{J}_n &= R \\ \nabla\cdot\underline{J}_p &= -R \end{aligned}} \tag{118}$$

Where $n = n(x,y), p = p(x,y)$ and $\varphi = \varphi(x,y)$ are the dependent variables and in particular they are the electron concentration in $[m^{-3}]$, the hole concentration in $[m^{-3}]$ and the electric voltage in $[V]$ respectively. Whereas, q is the elementary charge, ε is the dielectric constant of the material, $C = C(x,y)$ is the dopant concentration in $[m^{-3}]$, R is the recombination rate and $\underline{J}_n = \left[J_{nx}, J_{ny}\right]^T$ and $\underline{J}_p = \left[J_{px}, J_{py}\right]^T$ are the electron and hole current density in $[A/cm^2]$ defined as:

$$\underline{J}_n = \mathbf{M}_{B,n}\underline{J}_{ns} \tag{119}$$

$$\underline{J}_p = \mathbf{M}_{B,p}\underline{J}_{ps} \tag{120}$$

Where:

$$\mathbf{M}_{B,n} = \frac{1}{1+\mu_{nH}^2 B^2}\begin{bmatrix} 1 & -\mu_{nH}B \\ \mu_{nH}B & 1 \end{bmatrix} \tag{121}$$

$$\mathbf{M}_{B,p} = \frac{1}{1+\mu_{pH}^2 B^2}\begin{bmatrix} 1 & \mu_{pH}B \\ -\mu_{pH}B & 1 \end{bmatrix} \tag{122}$$

In which B is the intensity of the magnetic induction in $[T]$, where $\underline{B}_{ext} = [0,0,B]^T$, whereas μ_{nH} and μ_{pH} are the Hall electron and hole mobility respectively and $\underline{J}_{ns} = \left[J_{nxs}, J_{nys}\right]^T$ and $\underline{J}_{ps} = \left[J_{pxs}, J_{pys}\right]^T$ are the "standard" electron and hole current density (i.e. the current density when no magnetic field is present). In particular, they are defined as:

$$\underline{J}_{ns} = -q\left(\mu_n n \nabla\varphi - D_n \nabla n\right) \tag{123}$$

$$\underline{J}_{ps} = -q\left(\mu_p p \nabla\varphi + D_p \nabla p\right) \tag{124}$$

Where μ_n and μ_p are the electron and hole mobility and D_n and D_p are the electron and hole diffusion coefficients. Among the parameters $\mu_{n(p)}$, $\mu_{nH(pH)}$ and $D_{n(p)}$ the following relations hold:

$$\mu_{nH(0pH)} = r_{n(p)}\mu_{n(p)} \tag{125}$$

$$D_{n(p)} = \frac{kT}{q}\mu_{n(p)} \tag{126}$$

Where β and $r_{n(p)}$ are constant parameters, k is the Boltzmann's constant and T is the absolute temperature. Finally, many models for the recombination rate R are available, the following form is adopted:

$$R = \frac{np - n_i^2}{\tau_p\left(n + n_i\right) + \tau_n\left(p + n_i\right)} \tag{127}$$

In order to complete the model description, the boundary conditions must be included. Therefore, on the metal contacts one has (for the sake of clarity the contacts are identified as "A" and "B"):

$$\begin{cases} \varphi_A = 0 \\ n_A = \dfrac{\sqrt{C_A^2 + 4n_i^2} + C}{2} \\ p_A = \dfrac{\sqrt{C_A^2 + 4n_i^2} - C_A}{2} \end{cases} \qquad \begin{cases} \varphi_B = V_0 - V_{applied} \\ n_B = \dfrac{\sqrt{C_B^2 + 4n_i^2} + C_B}{2} \\ p_B = \dfrac{\sqrt{C_B^2 + 4n_i^2} - C_B}{2} \end{cases} \tag{128}$$

In which n_i is the intrinsic concentration, V_0 is the built in potential and $V_{applied}$ is the externally applied voltage. On the insulating boundaries, neglecting the surface charge, one has:

$$\frac{\partial \varphi}{\partial \underline{\eta}} = -\frac{1}{\sigma_{nH} + \sigma_{pH}} \left(\mu_{Hn} \underline{B} \times \underline{J}_{ns} + \mu_{Hp} \underline{B} \times \underline{J}_{ps} \right) \cdot \underline{\eta} \tag{129}$$

$$\underline{J}_n \cdot \underline{\eta} = 0 \tag{130}$$

$$\underline{J}_p \cdot \underline{\eta} = 0 \tag{131}$$

Where $\underline{\eta}$ is the unity normal vector to the boundary line, while:

$$\sigma_{Hn} = q \mu_{Hn} n \tag{132}$$

$$\sigma_{Hp} = q \mu_{Hp} p \tag{133}$$

If the geometry of the device is rectangular, the insulating boundary are parallel to the x-axis and the magnetic field is parallel to the z-axis (see Fig. 8) then (129), (130) and (131) reduce to:

$$\frac{\partial \varphi}{\partial \underline{\eta}} = \pm \frac{B}{\sigma_{nH} + \sigma_{pH}} \left(\mu_{Hn} J_{nxS} + \mu_{Hp} J_{pxS} \right) \tag{134}$$

$$J_{ny} = 0 \tag{135}$$

$$J_{py} = 0 \tag{136}$$

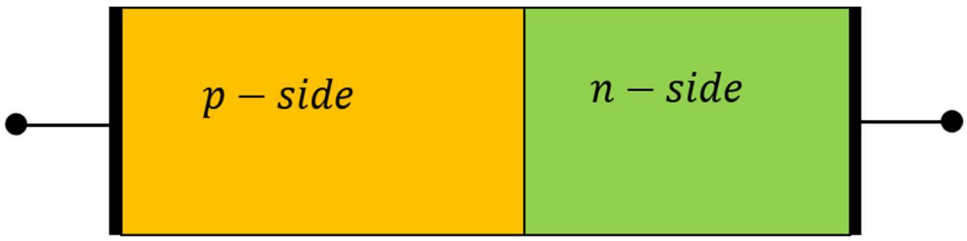

Fig. 8 Rectangular PN junction

3.3 Simulation code development

Before getting into the code description a fundamental remark must be made. Although this part may look as highly mathematical and theoretical, one has to keep in mind that it only represents the basis of any finite difference/element solver. As

a matter of fact, every commercial software making 3D/2D finite difference/element simulations is based on complex partial differential equations, sophisticated discretization techniques, efficient solving algorithms and the list goes further on. However, all this part is somehow "hidden" from the software user because it has already been programmed in advance. Anyhow, although it is hidden, it represents the "invisible basis" without which the programme would not even exist. Therefore, the lack of software programs in this case able to run the desired simulations, made it necessary to develop the entire software from the very foundation, leading to complex but necessary pure mathematical steps. Hence, it is of crucial importance to remember that even if these mathematical steps are tedious and lengthy, they only constitute the necessary (and very rudimental) tools to solve semiconductor equations which are anyway already dealt with by other state of the art software [20, 21], whose license is not available in ITER.

The description of such part is necessary because all the results depend on it, but again, it only represents the tool to achieve the final goal, which in the end is being able to solve the semiconductor equations in every operating condition of interest. In such view, this section could be skipped entirely and reading can be resumed starting from section 7.

This section is dedicated to describe all the necessary steps that must be taken in order to develop a finite difference/volume code able to solve the equations of the proposed model. More specifically, these steps can be listed as follows:

1. Scaling equations: in order to reduce the computational effort, scaling always represent a good strategy as it reduces the numerical range within which the dependent variables can vary. In particular, the dependent variables considered in this study, (i.e. φ, n, p) are of greatly different orders of magnitude (easily even more than 15) and show a strongly different behaviour in regions with small and large space charge; therefore, the first step towards a structural analysis has to be appropriate scaling.
2. Discretizing the continuous equations over a mesh grid: the system of partial differential equations together with appropriate boundary conditions determine a system which cannot be solved explicitly in general. Therefore, the solution must be calculated by means of numerical approaches. Any numerical approach consists essentially of three tasks, first the domain (i.e. the simulation geometry of the device has to be partitioned into finite number of subdomains, in which the solution can be approximated easily with a desired accuracy). Secondly, the differential equations have to be approximated in each subdomain by algebraic equations which involve only values of the continuous dependent variables at discrete points in the

domain and knowledge of the structure of the chosen functions which approximate the dependent variables within each of the subdomains.

3. Implementing a particular technique in order to solve systems of algebraic equations. Thanks to the discretizing process one obtains a fairly large system of, in general nonlinear, algebraic equations with unknowns comprised of approximations of the continuous dependent variables at discrete points. The solution of this system is the third task to be carried out.

It should be noted a priori that with the above outlined procedure it is impossible to obtain an exact solution of the analytically formulated problem. Instead one can obtain in the best case an exact solution of the nonlinear algebraic equations which form the discrete problem. Such solution represents a good approximation to the solution of the analytically formulated problem depending upon the fineness of the partitions of the simulation subdomains and the suitability of the approximating functions for the dependent variables within the subdomains.

The following subsections describe point 1. 2. and 3. in the 2-dimensional case.

3.4 Equation scaling

The final results of the equation scaling are reported in the following.

Table 1 Real value and normalised quantities

$\boldsymbol{\varphi}$	Electric voltage [$\boldsymbol{V}$]	$\boldsymbol{\varphi_{pu}}$	Electric voltage [$\boldsymbol{pu}$]
$\boldsymbol{n}$	Electron concentration $[m^{-3}]$	n_{pu}	Electron concentration $[pu]$
$\boldsymbol{p}$	Hole concentration $[m^{-3}]$	p_{pu}	Hole concentration $[pu]$
$\boldsymbol{c}$	Dopant concentration $[m^{-3}]$	c_{pu}	Dopant concentration $[pu]$
$\boldsymbol{x}$	X-coordinate $[m]$	x_{pu}	X-coordinate $[pu]$
$\boldsymbol{y}$	Y-coordinate $[m]$	y_{pu}	Y-coordinate $[pu]$

Where “pu” is for “Per Unit”. If the following relations are defined:

$$\varphi = U_t \varphi_{pu} \quad , \quad U_t = \frac{kT}{q} \tag{137}$$

$$n = n_i n_{pu} \tag{138}$$

$$p = n_i p_{pu} \tag{139}$$

$$c = n_i c_{pu} \tag{140}$$

$$x = L_0 x_{pu} \quad , \quad L_0 = \sqrt{\frac{U_t \varepsilon}{n_i q}} \tag{141}$$

$$y = L_0 y_{pu} \tag{142}$$

$$D_{n,p} = D_0 d_{n,p} \tag{143}$$

Where:

$$D_0 = \max\left\{D_n, D_p\right\} = U_t \max\left\{\mu_n, \mu_p\right\} \tag{144}$$

The following scaled equations are obtained:

$$\boxed{\begin{array}{c} \nabla \cdot \nabla \varphi_{pu} + p_{pu} - n_{pu} - c_{pu} = 0 \\ \nabla \cdot \underline{j}_{n,pu} = r_n \\ \nabla \cdot \underline{j}_{p,pu} = r_p \end{array}} \tag{145}$$

Where:

$$r_n = \frac{np - 1}{\tau_p^n \left(n+1\right) + \tau_n^n \left(p+1\right)} \tag{146}$$

$$r_p = -\frac{np - 1}{\tau_p^p \left(n+1\right) + \tau_n^p \left(p+1\right)} \tag{147}$$

In which:

$$\tau_p^n = \tau_p \frac{D_0}{\left(1 + c_{Bn}^2\right) L_0^2} \quad , \quad \tau_n^n = \tau_n \frac{D_0}{\left(1 + c_{Bn}^2\right) L_0^2} \quad , \quad \tau_p^p = \tau_p \frac{D_0}{\left(1 + c_{Bp}^2\right) L_0^2} \quad , \quad \tau_n^p = \tau_n \frac{D_0}{\left(1 + c_{Bp}^2\right) L_0^2} \tag{148}$$

Finally, the scaled current densities are:

$$J_{nx} = J_{0n} j_{nx,pu} \quad , \quad J_{ny} = J_{0n} j_{ny,pu} \tag{149}$$

$$J_{px} = J_{0p} j_{px,pu} \quad , \quad J_{py} = J_{0p} j_{py,pu} \tag{150}$$

Where:

$$J_{0n} = \frac{qn_i D_0}{L_0\left(1+c_{nB}^2\right)} \tag{151}$$

$$J_{0p} = \frac{qn_i D_0}{L_0\left(1+c_{pB}^2\right)} \tag{152}$$

And:

$$c_{nB} = \mu_{Hn} B \tag{153}$$

$$c_{pB} = -\mu_{Hp} B \tag{154}$$

In addition, one has:

$$\underline{j}_{n,pu} = \begin{bmatrix} j_{nx,pu} \\ j_{ny,pu} \end{bmatrix} = \begin{bmatrix} j_{nxS,pu} - c_{Bn} j_{nyS,pu} \\ j_{nyS,pu} + c_{Bn} j_{nxS,pu} \end{bmatrix} \tag{155}$$

$$\underline{j}_{p} = \begin{bmatrix} j_{px} \\ j_{py} \end{bmatrix} = \begin{bmatrix} j_{pxS} - c_{Bp} j_{pyS} \\ j_{pyS} + c_{Bp} j_{pxS} \end{bmatrix} \tag{156}$$

In which:

$$j_{nxS,pu} = \frac{\partial n_{pu}}{\partial x_{pu}} - n_{pu}\frac{\partial \varphi_{pu}}{\partial x_{pu}} \quad , \quad j_{nyS,pu} = \frac{\partial n_{pu}}{\partial y_{pu}} - n_{pu}\frac{\partial \varphi_{pu}}{\partial y_{pu}} \tag{157}$$

$$j_{pxS,pu} = -\frac{\partial p_{pu}}{\partial x_{pu}} - p_{pu}\frac{\partial \varphi_{pu}}{\partial x_{pu}} \quad , \quad j_{pyS,pu} = -\frac{\partial p_{pu}}{\partial y_{pu}} - p_{pu}\frac{\partial \varphi_{pu}}{\partial y_{pu}} \tag{158}$$

For the sake of notation simplification, from now the “pu” subscript will be dropped.

3.5 Equation discretization

Let us define the elementary cell of a 2-dimensional mesh depicted in Fig. 9 and let us use the following abbreviations:

$$\begin{aligned} h_i &= x_{i+1} - x_i \quad i = 1,2,...,N_x \\ k_j &= y_{j+1} - y_j \quad j = 1,2,...,N_y \end{aligned} \tag{159}$$

$$f_{i,j} = f\left(x_i, y_j\right) \quad , \quad f_{i+1/2,j} = f\left(\frac{x_i + x_{i+1}}{2}, y_j\right) \quad , \quad f_{i,j+1/2} = f\left(x_i, \frac{y_j + y_{j+1}}{2}\right) \tag{160}$$

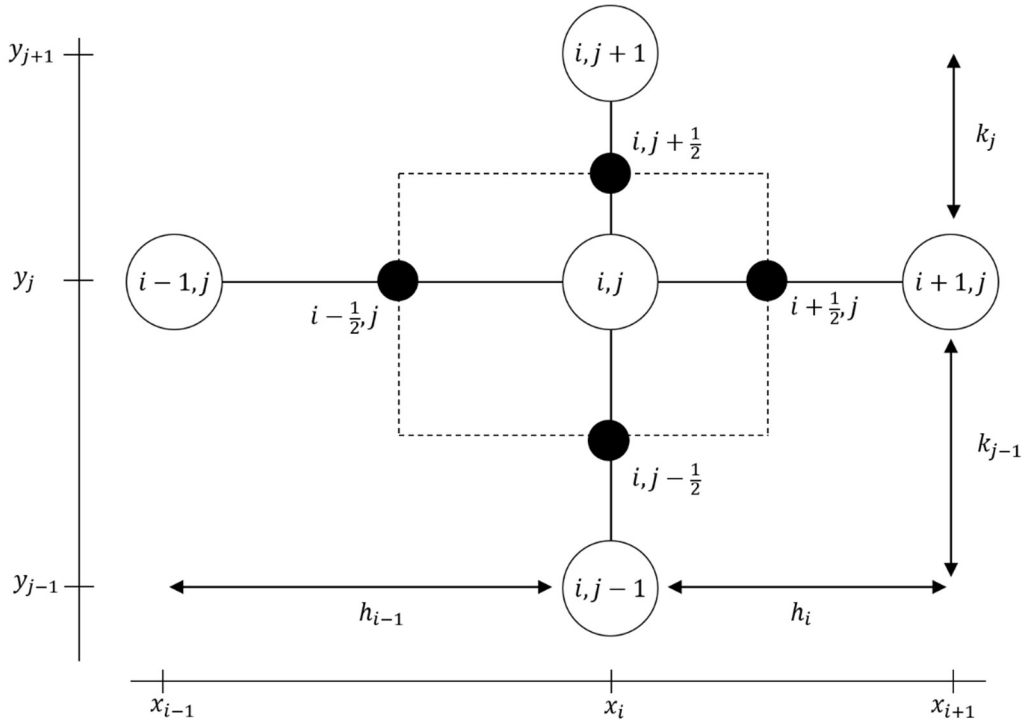

Fig. 9 Finite difference mesh - elementary cell

Please remember that the middle points (for instance the point $(x_{i-\frac{1}{2}}, y_j)$) do not belong to the mesh, they are only useful to obtain the final discretized functions, in which they should not appear.

The finite difference scheme replaces the derivative operator by difference operator, i.e.:

$$\left.\frac{\partial f}{\partial x}\right|_{i,j} \cong \frac{f_{i+1/2,j} - f_{i-1/2,j}}{\frac{h_i + h_{i+1}}{2}} \quad , \quad \left.\frac{\partial f}{\partial y}\right|_{i,j} \cong \frac{f_{i,j+1/2} - f_{i,j-1/2}}{\frac{k_j + k_{j+1}}{2}} \tag{161}$$

Focusing on the Poisson's equation (i.e. the first one of (145)) and applying once the finite difference operator, one obtains:

$$\frac{\left.\frac{\partial\varphi}{\partial x}\right|_{i+1/2,j} - \left.\frac{\partial\varphi}{\partial x}\right|_{i-1/2,j}}{\frac{h_i + h_{i-1}}{2}} + \frac{\left.\frac{\partial\varphi}{\partial y}\right|_{i,j+1/2} - \left.\frac{\partial\varphi}{\partial y}\right|_{i,j-1/2}}{\frac{k_j + k_{j-1}}{2}} - n_{i,j} + p_{i,j} - c_{i,j} = 0 \qquad (162)$$

Applying a second time the finite difference operator to (162), one obtains the final form the discretized Poisson's equation:

$$F^I_{i,j} = \frac{\frac{\varphi_{i+1,j} - \varphi_{i,j}}{h_i} - \frac{\varphi_{i,j} - \varphi_{i-1,j}}{h_{i-1}}}{\frac{h_i + h_{i-1}}{2}} + \frac{\frac{\varphi_{i,j+1} - \varphi_{i,j}}{k_j} - \frac{\varphi_{i,j} - \varphi_{i,j-1}}{k_{j-1}}}{\frac{k_j + k_{j-1}}{2}} - n_{i,j} + p_{i,j} - c_{i,j} = 0 \qquad (163)$$

Please note that since (163) has been obtained merely applied the finite difference operator, it automatically implies that the variation of the electric potential on the paths between mesh points has been approximated as linear, (i.e. the electric field is approximated as constant on these paths). Please note also that no information on this variation is available off these paths.

As regards the continuity equations, the first step is always to replace the differential operator with the difference operator (the attention is focused here only on the electron equation, as it is sufficient to apply exactly the same procedure to the hole equation in order to obtain its final discretized version):

$$\frac{j_{nx}\big|_{i+1/2,j} - j_{nx}\big|_{i-1/2,j}}{\bar{h}_i} + \frac{j_{ny}\big|_{i,j+1/2} - j_{ny}\big|_{i,j-1/2}}{\bar{k}_j} = r_n\big|_{i,j} \qquad (164)$$

Where:

$$\bar{h}_i = \frac{h_i + h_{i-1}}{2} \qquad (165)$$

$$\bar{k}_j = \frac{k_j + k_{j-1}}{2} \qquad (166)$$

Thanks to (155), (164) can be transformed into:

$$\frac{\left(j_{nxS}\Big|_{i+1/2,j} - c_{Bn}\, j_{nyS}\Big|_{i+1/2,j}\right) - \left(j_{nxS}\Big|_{i-1/2,j} - c_{Bn}\, j_{nyS}\Big|_{i-1/2,j}\right)}{\overline{h}_i} +$$
$$+ \frac{\left(j_{nyS}\Big|_{i,j+1/2} + c_{Bn}\, j_{nxS}\Big|_{i,j+1/2}\right) - \left(j_{nyS}\Big|_{i,j-1/2} + c_{Bn}\, j_{nxS}\Big|_{i,j-1/2}\right)}{\overline{k}_j} = \tag{167}$$
$$= r_n\Big|_{i,j}$$

Rearranging (167), one obtains:

$$\frac{j_{nxS}\Big|_{i+1/2,j} - j_{nxS}\Big|_{i-1/2,j}}{\overline{h}_i} + \frac{j_{nyS}\Big|_{i,j+1/2} - j_{nyS}\Big|_{i,j-1/2}}{\overline{k}_j} +$$
$$- c_{Bn}\frac{j_{nyS}\Big|_{i+1/2,j} - j_{nyS}\Big|_{i-1/2,j}}{\overline{h}_i} + c_{Bn}\frac{j_{nxS}\Big|_{i,j+1/2} - j_{nxS}\Big|_{i,j-1/2}}{\overline{k}_j} \tag{168}$$
$$= r_n\Big|_{i,j}$$

The discretization of the current density terms is extremely crucial. Indeed, if one proceeded with the standard finite difference method an extremely and excessively fine mesh would be necessary to obtain reasonable results. As a matter of fact, while the linear variation of the electric potential between mesh points is a good approximation, it cannot be stated the same as regards the electron and hole concentration (it is shown in [24] that if a linear variation of the electric potential is assumed, an exponential variation of n and p between mesh points occurs).

Thus, a different approach which was developed specifically for semiconductor equations must be adopted. Such approach, called the "Gummel-Sharfetter's method" was originally proposed in [28] and since then it has experienced many extensions and improvements. The basic idea behind this method is to consider constant over each interval between mesh points all the "slowly" varying quantities in the current density definition and solve analytically the resulting differential equation in n and p. By doing so, the current density terms can be discretized with significantly higher accuracy.

Only the final results are presented here. However, in 2 dimensions and in the presence of a non-zero ESMF, another problem arises when one has to deal with the discretization of continuity equations. As a matter of fact, the magnetic field invalidates some of the symmetries that facilitate the discretization of these equations. A couple of methods have been traced in the scientific literature [27, 29], however, after some studying, one seemed to provide poor performance while the other appeared to be unsatisfyingly complicated. Therefore, another method for discretizing these equations has been adopted in this study, which can be seen as a

good trade-off between complexity and performance. Such method is described below.

While the current terms in the first row of (168) can be computed according to the standard Gummel – Sharfetter's method, the current terms in the second row must be estimated differently because no boundary conditions are available if one tries to employ the Gummel-Sharfetter procedure. Thus, the simplest way to proceed without computing arithmetic means of the electron concentration in order to obtain the missing boundary conditions, is to directly calculate a bilinear interpolation of the current densities. Please note that using directly arithmetic means of the mesh point electron concentration values would invalidate the Gummel-Sharfetter's method, which is the reason why it must be completely avoided.

Let us first present the formula calculating a bilinear interpolation (for more information regarding bilinear interpolations, one can simply refer to [30]). Knowing the value of a generic function f in the points Q_{11}, Q_{12}, Q_{21} and Q_{22}, $f(P)$ is given by:

$$f\left(P\left(x,y\right)\right)=\frac{1}{\left(x_2-x_1\right)\left(y_2-y_1\right)}\left[x_2-x\ ,x-x_1\right]\begin{bmatrix}f\left(Q_{11}\right) & f\left(Q_{12}\right)\\ f\left(Q_{21}\right) & f\left(Q_{22}\right)\end{bmatrix}\begin{bmatrix}y_2-y\\ y-y_1\end{bmatrix} \tag{169}$$

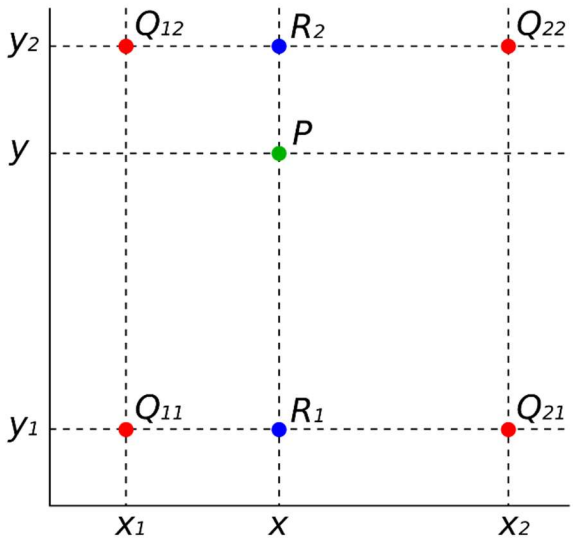

Fig. 10 Bilinear interpolation

(169) is the general formula, when P becomes the center of the rectangle, (i.e. $x_0 = \frac{x_1+x_2}{2}$ and $y_0 = \frac{y_1+y_2}{2}$) it degenerates in a simple arithmetic mean:

$$f\left(P\left(x_0,y_0\right)\right)=\frac{f_{11}+f_{12}+f_{21}+f_{22}}{4}$$

While, only when $y_0=\frac{y_1+y_2}{2}$ (169) becomes

$$f\left(P\left(x,y_0\right)\right)=\frac{\left(f_{11}+f_{12}\right)h_2+\left(f_{21}+f_{22}\right)h_1}{2\left(h_1+h_2\right)} \tag{170}$$

where $h_1=x-x_1$, $h_2=x_2-x$.

Note that this is the case of the $j_{nxS}|_{i,j+1/2}$ and $j_{nxS}|_{i,j-1/2}$ estimation since the mesh will be chosen to be non uniform in the x direction (more details are given further on this aspect).

On the other hand, if the grid is chosen to be non uniform also in the y direction, the general formula (169) has to be used.

The following figure describes graphically which are the points included in the bilinear approximation of $j_{nyS}|_{i+1/2,j}$ assuming a uniform mesh along the y direction (i.e. $k_1=k_2=\cdots=k_{N_y}$).

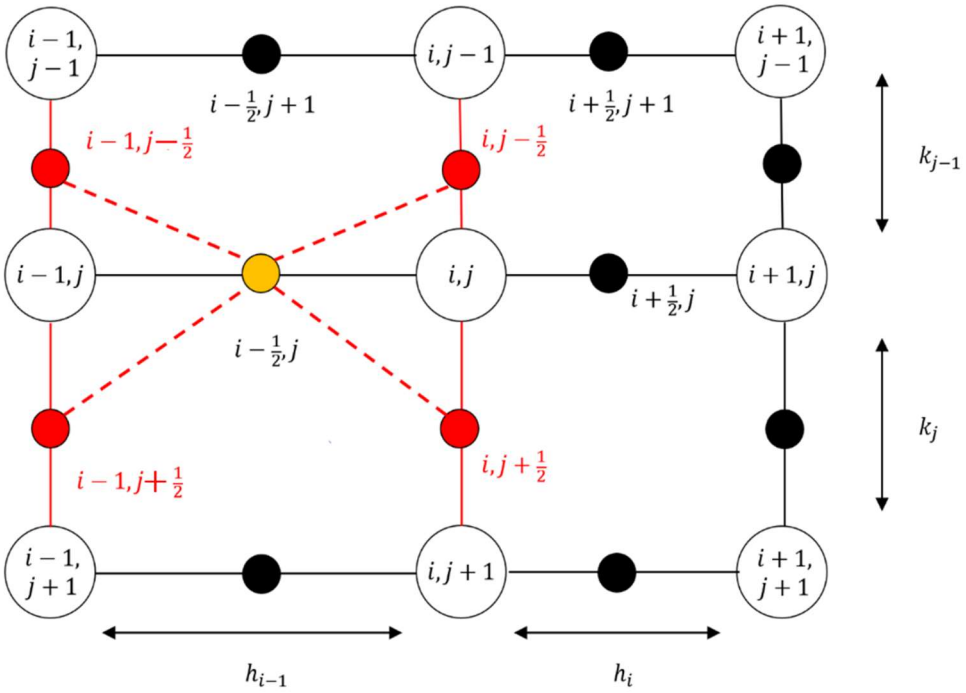

Fig. 11 Elementary cell of a finite difference mesh

Thus, in this case one has:

$$j_{nyS}\Big|_{i-1/2,j}=\frac{j_{nyS}\Big|_{i-1,j-1/2}+j_{nyS}\Big|_{i-1,j+1/2}+j_{nyS}\Big|_{i,j+1/2}+j_{nyS}\Big|_{i,j-1/2}}{4} \tag{171}$$

And similarly:

$$j_{nyS}\Big|_{i+1/2,j}=\frac{j_{nyS}\Big|_{i,j-1/2}+j_{nyS}\Big|_{i,j+1/2}+j_{nyS}\Big|_{i+1,j+1/2}+j_{nyS}\Big|_{i+1,j-1/2}}{4} \tag{172}$$

On the other hand, as far as j_{nxS} is concerned one has:

$$j_{nxS}\Big|_{i,j+1/2}=\frac{\left(j_{nxS}\Big|_{i-1/2,j}+j_{nxS}\Big|_{i-1/2,j+1}\right)h_i+\left(j_{nxS}\Big|_{i+1/2,j+1}+j_{nxS}\Big|_{i+1/2,j}\right)h_{i-1}}{2\left(h_i+h_{i-1}\right)} \tag{173}$$

$$j_{nxS}\Big|_{i,j-1/2}=\frac{\left(j_{nxS}\Big|_{i-1/2,j-1}+j_{nxS}\Big|_{i-1/2,j}\right)h_i+\left(j_{nxS}\Big|_{i+1/2,j}+j_{nxS}\Big|_{i+1/2,j-1}\right)h_{i-1}}{2\left(h_i+h_{i-1}\right)} \tag{174}$$

Recalling (168) one has:

$$\begin{aligned}&\frac{j_{nxS}\Big|_{i+1/2,j}-j_{nxS}\Big|_{i-1/2,j}}{\overline{h}_i}+\frac{j_{nyS}\Big|_{i,j+1/2}-j_{nyS}\Big|_{i,j-1/2}}{\overline{k}_j}+\\&-c_{Bn}\frac{j_{nyS}\Big|_{i+1/2,j}-j_{nyS}\Big|_{i-1/2,j}}{\overline{h}_i}+c_{Bn}\frac{j_{nxS}\Big|_{i,j+1/2}-j_{nxS}\Big|_{i,j-1/2}}{\overline{k}_j}\\&=r_n\Big|_{i,j}\end{aligned} \tag{175}$$

Inserting (171)-(174) in (175) the following expression is obtained:

$$\begin{aligned}&\frac{j_{nxS}\Big|_{i+1/2,j}-j_{nxS}\Big|_{i-1/2,j}}{\overline{h}_i}+\frac{j_{ny}\Big|_{i,j+1/2}-j_{ny}\Big|_{i,j-1/2}}{\overline{k}_j}+\\&-c_{Bn}\frac{\dfrac{j_{nyS}\Big|_{i,j-1/2}+j_{nyS}\Big|_{i,j+1/2}+j_{nyS}\Big|_{i+1,j+1/2}+j_{nyS}\Big|_{i+1,j-1/2}}{4}-\dfrac{j_{nyS}\Big|_{i-1,j-1/2}+j_{nyS}\Big|_{i-1,j+1/2}+j_{nyS}\Big|_{i,j+1/2}+j_{nyS}\Big|_{i,j-1/2}}{4}}{\overline{h}_i}\\&+c_{Bn}\frac{\dfrac{\left(j_{nxS}\Big|_{i-1/2,j}+j_{nxS}\Big|_{i-1/2,j+1}\right)h_i+\left(j_{nxS}\Big|_{i+1/2,j+1}+j_{nxS}\Big|_{i+1/2,j}\right)h_{i-1}}{2\left(h_i+h_{i-1}\right)}-\dfrac{\left(j_{nxS}\Big|_{i-1/2,j-1}+j_{nxS}\Big|_{i-1/2,j}\right)h_i+\left(j_{nxS}\Big|_{i+1/2,j}+j_{nxS}\Big|_{i+1/2,j-1}\right)h_{i-1}}{2\left(h_i+h_{i-1}\right)}}{\overline{k}_j}\\&=r_n\Big|_{i,j}\end{aligned} \tag{176}$$

Thus, after some simplifications:

$$\frac{j_{nxS}\big|_{i+1/2,j}-j_{nxS}\big|_{i-1/2,j}}{\bar{h}_i}+\frac{j_{ny}\big|_{i,j+1/2}-j_{ny}\big|_{i,j-1/2}}{\bar{k}_j}+$$
$$-c_{Bn}\frac{\frac{\cancel{j_{nyS}\big|_{i,j-1/2}}+\cancel{j_{nyS}\big|_{i,j+1/2}}+j_{nyS}\big|_{i+1,j+1/2}+j_{nyS}\big|_{i+1,j-1/2}}{4}-\frac{j_{nyS}\big|_{i-1,j-1/2}+j_{nyS}\big|_{i-1,j+1/2}+\cancel{j_{nyS}\big|_{i,j+1/2}}+\cancel{j_{nyS}\big|_{i,j-1/2}}}{4}}{\bar{h}_i}$$
$$+c_{Bn}\frac{\frac{\left(\cancel{j_{nxS}\big|_{i-1/2,j}}+j_{nxS}\big|_{i-1/2,j+1}\right)h_i+\left(j_{nxS}\big|_{i+1/2,j+1}+\cancel{j_{nxS}\big|_{i+1/2,j}}\right)h_{i-1}}{2\left(h_i+h_{i-1}\right)}-\frac{\left(j_{nxS}\big|_{i-1/2,j-1}+\cancel{j_{nxS}\big|_{i-1/2,j}}\right)h_i+\left(\cancel{j_{nxS}\big|_{i+1/2,j}}+j_{nxS}\big|_{i+1/2,j-1}\right)h_{i-1}}{2\left(h_i+h_{i-1}\right)}}{\bar{k}_j}$$
$$=r_n\big|_{i,j}$$

(177)

Leading to the final form of the discretized electron continuity equation:

$$\boxed{\begin{aligned}F_{i,j}^{II}=&\frac{j_{nxS}\big|_{i+1/2,j}-j_{nxS}\big|_{i-1/2,j}}{\bar{h}_i}+\frac{j_{nyS}\big|_{i,j+1/2}-j_{nyS}\big|_{i,j-1/2}}{k}+\\&-c_{Bn}\frac{\left(j_{nyS}\big|_{i+1,j+1/2}+j_{nyS}\big|_{i+1,j-1/2}\right)-\left(j_{nyS}\big|_{i-1,j-1/2}+j_{nyS}\big|_{i-1,j+1/2}\right)}{4\bar{h}_i}+\\&+c_{Bn}\frac{\left(j_{nxS}\big|_{i-1/2,j+1}-j_{nxS}\big|_{i-1/2,j-1}\right)h_i+\left(j_{nxS}\big|_{i+1/2,j+1}-j_{nxS}\big|_{i+1/2,j-1}\right)h_{i-1}}{2\left(h_i+h_{i-1}\right)k}+\\&-r_n\big|_{i,j}=0\end{aligned}} \tag{178}$$

Where:

$$j_{nxS}\big|_{i+1/2,j}=\frac{d_{n,i+1/2,j}}{h_i}\left(-B\left(-\Delta\varphi_{i,j}^{x}\right)n_{i,j}+B\left(\Delta\varphi_{i,j}^{x}\right)n_{i+1,j}\right) \tag{179}$$

In which $\Delta\varphi_{i,j}^{x}=\varphi_{i,j}-\varphi_{i-1,j}$ and $B(\cdot)$ is known to be the Bernoulli's function:

$$B\left(t\right)=t/\left(e^{t}-1\right) \tag{180}$$

Similarly:

$$j_{nxS}\big|_{i,j+1/2}=\frac{d_{n,i,j+1/2}}{k_j}\left(-B\left(-\Delta\varphi_{i,j}^{y}\right)n_{i,j}+B\left(\Delta\varphi_{i,j}^{y}\right)n_{i,j+1}\right) \tag{181}$$

where $\Delta\varphi_{i,j}^{y}=\varphi_{i,j+1}-\varphi_{i,j}$ and:

$$d_{n,i+1/2,j}=\frac{d_{n,i,j}+d_{n,i+1,j}}{2}\quad,\quad d_{n,i,j+1/2}=\frac{d_{n,i,j}+d_{n,i,j+1}}{2} \tag{182}$$

This particular discretization of the current density [24, 28, 31] is necessary due to the fact that in the continuity equations variables of different order of magnitude appear (i.e. φ on one side and n and p on the other). Thus the standard linear approximation given by the finite difference method would require a huge number of points in order to obtain accurate results.

Exactly the same procedure can be applied to the hole continuity equation, leading to:

$$\begin{gathered}\frac{j_{pxS}\Big|_{i+1/2,j}-j_{pxS}\Big|_{i-1/2,j}}{\bar{h}_i}+\frac{j_{pyS}\Big|_{i,j+1/2}-j_{pyS}\Big|_{i,j-1/2}}{k}+\\ -c_{Bp}\frac{\left(j_{pyS}\Big|_{i+1,j+1/2}+j_{pyS}\Big|_{i+1,j-1/2}\right)-\left(j_{pyS}\Big|_{i-1,j-1/2}+j_{pyS}\Big|_{i-1,j+1/2}\right)}{4\bar{h}_i}+\\ +c_{Bn}\frac{\left(j_{pxS}\Big|_{i-1/2,j+1}-j_{pxS}\Big|_{i-1/2,j-1}\right)h_i+\left(j_{pxS}\Big|_{i+1/2,j+1}-j_{pxS}\Big|_{i+1/2,j-1}\right)h_{i-1}}{2\left(h_i+h_{i-1}\right)k}=\\ =r_p\Big|_{i,j}\end{gathered} \tag{183}$$

Where:

$$j_{pxS}\Big|_{i+1/2,j}=\frac{d_{p,i+1/2,j}}{h_i}\left(-B\left(-\Delta\varphi^x_{i,j}\right)p_{i+1,j}+B\left(\Delta\varphi^x_{i,j}\right)p_{i,j}\right) \tag{184}$$

$$j_{pyS}\Big|_{i,j+1/2}=\frac{d_{p,i,j+1/2}}{k_j}\left(-B\left(-\Delta\varphi^y_{i,j}\right)p_{i,j+1}+B\left(\Delta\varphi^y_{i,j}\right)p_{i,j}\right) \tag{185}$$

And:

$$d_{p,i+1/2,j}=\frac{d_{p,i,j}+d_{p,i+1,j}}{2}\quad,\quad d_{p,i,j+1/2}=\frac{d_{p,i,j}+d_{p,i,j+1}}{2} \tag{186}$$

On balance, the assumptions which has been made are the following:

1. E_x is constant along horizontal paths connecting each single mesh point.
2. E_y is constant along vertical paths connecting each single mesh point.
3. j_{nxS} is constant along horizontal paths connecting each single mesh point.
4. j_{nyS} is constant along vertical paths connecting each single mesh point.
5. j_{nxS} and j_{nyS} vary linearly along paths connecting midpoints.

Please notice that the only additional assumption which has been made (in comparison with the standard case with no magnetic field [24]) is the 5th, which is the assumption necessary to make the bilinear interpolation among current density values.

It remains to obtain the discretized version of the Neumann's boundary condition (i.e. the conditions at the insulating boundaries). Recalling (129)-(131) one has:

$$\frac{\partial \varphi}{\partial \underline{\eta}} = \pm \frac{B}{\sigma_{nH} + \sigma_{pH}} \left(\mu_{Hn} J_{nxS} + \mu_{Hp} J_{pxS} \right) \quad , \quad \underline{j}_n \cdot \underline{\eta} = 0 \quad , \quad \underline{j}_p \cdot \underline{\eta} = 0 \quad (187)$$

In order to discretize the Neuman's boundary conditions the mirror imaging technique is adopted [24]. According to this technique, without any loss of generality, one can write the following linear interpolation scheme, assuming a boundary parallel to the x-axis:

$$u_{i,j} = \frac{u_{i,j+1/2} + u_{i,j-1/2}}{2} \quad j = 1, N_y \quad (188)$$

For a rectangular geometry, assuming Dirichlet's boundary conditions applied to boundaries parallel to the y-axis (i.e. at the metal contacts), (187) becomes:

$$\frac{\partial \varphi}{\partial y} = \pm \frac{B}{\sigma_{nH} + \sigma_{pH}} \left(\mu_{Hn} J_{nxS} + \mu_{Hp} J_{pxS} \right) \quad , \quad j_{ny} = 0 \quad , \quad j_{py} = 0 \quad (189)$$

As regards the discretization of Neumann's condition on the electric potential, one has:

$$\frac{\left.\frac{\partial \varphi}{\partial y}\right|_{i,N_y+1/2} + \left.\frac{\partial \varphi}{\partial y}\right|_{i,N_y-1/2}}{2} = -\frac{B}{\sigma_{nH} + \sigma_{pH}} \left(\mu_{Hn} \frac{j_{nxS}\big|_{i-1/2,N_y} + j_{nxS}\big|_{i+1/2,N_y}}{2} + \mu_{Hp} \frac{j_{pxS}\big|_{i-1/2,N_y} + j_{pxS}\big|_{i+1/2,N_y}}{2} \right) \quad (190)$$

$$\frac{\left.\frac{\partial \varphi}{\partial y}\right|_{i,1+1/2} + \left.\frac{\partial \varphi}{\partial y}\right|_{i,1-1/2}}{2} = \frac{B}{\sigma_{nH} + \sigma_{pH}} \left(\mu_{Hn} \frac{j_{nxS}\big|_{i-1/2,1} + j_{nxS}\big|_{i+1/2,1}}{2} + \mu_{Hp} \frac{j_{pxS}\big|_{i-1/2,1} + j_{pxS}\big|_{i+1/2,1}}{2} \right) \quad (191)$$

Leading to:

$$\left.\frac{\partial\varphi}{\partial y}\right|_{i,N_y+1/2} = -\left.\frac{\partial\varphi}{\partial y}\right|_{i,N_y-1/2} - \frac{2B}{\sigma_{nH}+\sigma_{pH}}\left(\mu_{Hn}\frac{j_{nxS}\big|_{i-1/2,N_y}+j_{nxS}\big|_{i+1/2,N_y}}{2}+\mu_{Hp}\frac{j_{pxS}\big|_{i-1/2,N_y}+j_{pxS}\big|_{i+1/2,N_y}}{2}\right) \tag{192}$$

$$\left.\frac{\partial\varphi}{\partial y}\right|_{i,1-1/2} = -\left.\frac{\partial\varphi}{\partial y}\right|_{i,1+1/2} + \frac{2B}{\sigma_{nH}+\sigma_{pH}}\left(\mu_{Hn}\frac{j_{nxS}\big|_{i-1/2,N_y}+j_{nxS}\big|_{i+1/2,N_y}}{2}+\mu_{Hp}\frac{j_{pxS}\big|_{i-1/2,N_y}+j_{pxS}\big|_{i+1/2,N_y}}{2}\right) \tag{193}$$

Therefore, the discretized Poisson's equation for $j = 1, N_y$ is obtained respectively replacing (192) in (162), hence:

$$\frac{\left.\frac{\partial\varphi}{\partial x}\right|_{i+1/2,N_y} - \left.\frac{\partial\varphi}{\partial x}\right|_{i-1/2,N_y}}{\frac{h_i+h_{i-1}}{2}} + \frac{-\frac{2B}{\sigma_{nH}+\sigma_{pH}}\left(\mu_{Hn}\frac{j_{nxS}\big|_{i-1/2,N_y}+j_{nxS}\big|_{i+1/2,N_y}}{2}+\mu_{Hp}\frac{j_{pxS}\big|_{i-1/2,N_y}+j_{pxS}\big|_{i+1/2,N_y}}{2}\right) - 2\left.\frac{\partial\varphi}{\partial y}\right|_{i,N_y-1/2}}{k_{N_y-1}} +$$
$$-n_{i,N_y}+p_{i,N_y}-c_{i,N_y}=0 \tag{194}$$

And finally:

$$F^I_{By1} = \frac{\frac{\varphi_{i+1,N_y}-\varphi_{i,N_y}}{h_i} - \frac{\varphi_{i,N_y}-\varphi_{i-1,N_y}}{h_{i-1}}}{\frac{h_i+h_{i-1}}{2}} +$$
$$\frac{-\frac{2B}{\sigma_{nH}+\sigma_{pH}}\left(\mu_{Hn}\frac{j_{nxS}\big|_{i-1/2,N_y}+j_{nxS}\big|_{i+1/2,N_y}}{2}+\mu_{Hp}\frac{j_{pxS}\big|_{i-1/2,N_y}+j_{pxS}\big|_{i+1/2,N_y}}{2}\right) + 2\left.\frac{\partial\varphi}{\partial y}\right|_{i,N_y-1/2}}{k_{N_y-1}} +$$
$$-n_{i,N_y}+p_{i,N_y}-c_{i,N_y}=0 \tag{195}$$

While the discretized equation on the other boundary is obtained substituting and (193) in (162), leading to:

$$F_{By2}^{I}=\frac{\frac{\varphi_{i+1,N_y}-\varphi_{i,N_y}}{h_i}-\frac{\varphi_{i,N_y}-\varphi_{i-1,N_y}}{h_{i-1}}}{\frac{h_i+h_{i-1}}{2}}+$$
$$-\frac{\frac{2B}{\sigma_{nH}+\sigma_{pH}}\left(\mu_{Hn}\frac{j_{nxS}\big|_{i-1/2,N_y}+j_{nxS}\big|_{i+1/2,N_y}}{2}+\mu_{Hp}\frac{j_{pxS}\big|_{i-1/2,N_y}+j_{pxS}\big|_{i+1/2,N_y}}{2}\right)+2\frac{\varphi_{i,N_y}-\varphi_{i,N_y-1}}{k_{N_y-1}}}{k_{N_y-1}}+$$
$$-n_{i,N_y}+p_{i,N_y}-c_{i,N_y}=0$$

(196)

$$F_{By1}^{I}=\frac{\frac{\varphi_{i+1,1}-\varphi_{i,1}}{h_i}-\frac{\varphi_{i,1}-\varphi_{i-1,1}}{h_{i-1}}}{\frac{h_i+h_{i-1}}{2}}$$
$$+\frac{2\frac{\varphi_{i,2}-\varphi_{i,1}}{k_1}-\frac{2B}{\sigma_{nH}+\sigma_{pH}}\left(\mu_{Hn}\frac{j_{nxS}\big|_{i-1/2,1}+j_{nxS}\big|_{i+1/2,1}}{2}+\mu_{Hp}\frac{j_{pxS}\big|_{i-1/2,1}+j_{pxS}\big|_{i+1/2,1}}{2}\right)}{k_1}$$
$$-n_{i,1}+p_{i,1}-c_{i,1}=0$$

(197)

On the other hand, as regards the electron continuity equation, j_{nyS} for $j=1$ and $j=N_y$ becomes:

$$j_{ny}\big|_{i,1}=\frac{j_{ny}\big|_{i,1-1/2}+j_{ny}\big|_{i,1+1/2}}{2}=0 \quad , \quad j_{ny}\big|_{i,N_y}=\frac{j_{ny}\big|_{i,N_y-1/2}+j_{ny}\big|_{i,N_y+1/2}}{2}=0$$

(198)

Therefore:

$$j_{ny}\big|_{i,1-1/2}=-j_{ny}\big|_{i,1+1/2} \qquad j=1 \tag{199}$$

$$j_{ny}\big|_{i,N_y+1/2}=-j_{ny}\big|_{i,N_y-1/2} \qquad N_y=1 \tag{200}$$

Hence:

$$j_{nyS}\big|_{i,1-1/2}+c_{Bn}\,j_{nxS}\big|_{i,1-1/2}=-\left(j_{nyS}\big|_{i,1+1/2}+c_{Bn}\,j_{nxS}\big|_{i,1+1/2}\right) \qquad j=1 \tag{201}$$

$$j_{nyS}\big|_{i,1+1/2}+c_{Bn}\,j_{nxS}\big|_{i,1+1/2}=-\left(j_{nyS}\big|_{i,1-1/2}+c_{Bn}\,j_{nxS}\big|_{i,1-1/2}\right) \qquad j=N_y \tag{202}$$

Recalling (167) :

$$\frac{\left(j_{nxS}\Big|_{i+1/2,j}-c_{Bn}\,j_{nyS}\Big|_{i+1/2,j}\right)-\left(j_{nxS}\Big|_{i-1/2,j}-c_{Bn}\,j_{nyS}\Big|_{i-1/2,j}\right)}{\overline{h}_i}+$$
$$+\frac{\left(j_{nyS}\Big|_{i,j+1/2}+c_{Bn}\,j_{nxS}\Big|_{i,j+1/2}\right)-\left(j_{nyS}\Big|_{i,j-1/2}+c_{Bn}\,j_{nxS}\Big|_{i,j-1/2}\right)}{\overline{k}_j}= \tag{203}$$
$$=r_n\Big|_{i,j}$$

Therefore, inserting (201) in (203) we obtain the discretized equation at the horizontal boundaries:

$$\frac{\left(j_{nxS}\Big|_{i+1/2,1}-c_{Bn}\,j_{nyS}\Big|_{i+1/2,1}\right)-\left(j_{nxS}\Big|_{i-1/2,1}-c_{Bn}\,j_{nyS}\Big|_{i-1/2,1}\right)}{\overline{h}_i}+$$
$$+\frac{\left(j_{nyS}\Big|_{i,1+1/2}+c_{Bn}\,j_{nxS}\Big|_{i,1+1/2}\right)+\left(j_{nyS}\Big|_{i,1+1/2}+c_{Bn}\,j_{nxS}\Big|_{i,1+1/2}\right)}{\overline{k}_j}= \tag{204}$$
$$=r_n\Big|_{i,1}$$

Which leads to:

$$\frac{\left(j_{nxS}\Big|_{i+1/2,1}-c_{Bn}\,j_{nyS}\Big|_{i+1/2,1}\right)-\left(j_{nxS}\Big|_{i-1/2,1}-c_{Bn}\,j_{nyS}\Big|_{i-1/2,1}\right)}{\overline{h}_i}+$$
$$+2\frac{j_{nyS}\Big|_{i,1+1/2}+c_{Bn}\,j_{nxS}\Big|_{i,1+1/2}}{k_1}= \tag{205}$$
$$=r_n\Big|_{i,1}$$

Whereas for $j=N_y$, (167) becomes:

$$\frac{\left(j_{nxS}\Big|_{i+1/2,N_y}-c_{Bn}\,j_{nyS}\Big|_{i+1/2,N_y}\right)-\left(j_{nxS}\Big|_{i-1/2,N_y}-c_{Bn}\,j_{nyS}\Big|_{i-1/2,N_y}\right)}{\overline{h}_i}+$$
$$+\frac{-\left(j_{nyS}\Big|_{i,N_y-1/2}+c_{Bn}\,j_{nxS}\Big|_{i,N_y-1/2}\right)-\left(j_{nyS}\Big|_{i,N_y-1/2}+c_{Bn}\,j_{nxS}\Big|_{i,N_y-1/2}\right)}{k_{N_y-1}}= \tag{206}$$
$$=r_n\Big|_{i,N_y}$$

Thus:

$$\frac{\left(j_{nxS}\Big|_{i+1/2,N_y}-c_{Bn}\,j_{nyS}\Big|_{i+1/2,N_y}\right)-\left(j_{nxS}\Big|_{i-1/2,N_y}-c_{Bn}\,j_{nyS}\Big|_{i-1/2,N_y}\right)}{\overline{h}_i}+$$
$$-2\frac{j_{nyS}\Big|_{i,N_y-1/2}+c_{Bn}\,j_{nxS}\Big|_{i,N_y-1/2}}{k_{N_y-1}}= \tag{207}$$
$$=r_n\Big|_{i,N_y}$$

Finally, inserting (173) in (205) we have:

$$\frac{j_{nxS}\Big|_{i+1/2,1}-j_{nxS}\Big|_{i-1/2,1}}{\overline{h}_i}-c_{Bn}\frac{j_{nyS}\Big|_{i+1/2,1}-j_{nyS}\Big|_{i-1/2,1}}{\overline{h}_i}+$$
$$+2\frac{j_{nyS}\Big|_{i,1+1/2}}{k_1}+2c_{Bn}\frac{\left(j_{nxS}\Big|_{i-1/2,1}+j_{nxS}\Big|_{i-1/2,1+1}\right)h_i+\left(j_{nxS}\Big|_{i+1/2,1+1}+j_{nxS}\Big|_{i+1/2,1}\right)h_{i-1}}{2\left(h_i+h_{i-1}\right)k_1}=$$
$$=r_n\Big|_{i,1}\qquad j=1 \tag{208}$$

Similarly, inserting (174) in (207) we obtain:

$$\frac{j_{nxS}\Big|_{i+1/2,N_y}-j_{nxS}\Big|_{i-1/2,N_y}}{\overline{h}_i}-c_{Bn}\frac{j_{nyS}\Big|_{i+1/2,N_y}-j_{nyS}\Big|_{i-1/2,N_y}}{\overline{h}_i}+$$
$$-2\frac{j_{nyS}\Big|_{i,N_y-1/2}}{k_{N_y-1}}-2c_{Bn}\frac{\left(j_{nxS}\Big|_{i-1/2,N_y-1}+j_{nxS}\Big|_{i-1/2,N_y}\right)h_i+\left(j_{nxS}\Big|_{i+1/2,N_y}+j_{nxS}\Big|_{i+1/2,N_y-1}\right)h_{i-1}}{2\left(h_i+h_{i-1}\right)k_{N_y-1}}=$$
$$=r_n\Big|_{i,N_y}\qquad j=N_y \tag{209}$$

A final remark should be made on how to compute $j_{nys}\big|_{i-1/2,j}$ and $j_{nys}\big|_{i+1/2,j}$ for $j=1,N_y$. In particular, (171) and (172) can be written as:

$$j_{nyS}\Big|_{i-1/2,1}=\frac{j_{nyS}\Big|_{i-1,1+1/2}+j_{nyS}\Big|_{i,1+1/2}}{2}\quad,\quad j_{nyS}\Big|_{i+1/2,1}=\frac{j_{nyS}\Big|_{i,1+1/2}+j_{nyS}\Big|_{i+1,1+1/2}}{2} \tag{210}$$

And similarly:

$$j_{nyS}\Big|_{i-1/2,N_y}=\frac{j_{nyS}\Big|_{i-1,N_y-1/2}+j_{nyS}\Big|_{i,N_y-1/2}}{2}\quad,\quad j_{nyS}\Big|_{i+1/2,N_y}=\frac{j_{nyS}\Big|_{i,N_y-1/2}+j_{nyS}\Big|_{i+1,N_y-1/2}}{2}$$

(211)

Thus, one has:

$$\begin{aligned}j_{nyS}\Big|_{i+1/2,1}-j_{nyS}\Big|_{i-1/2,1}&=\frac{j_{nyS}\Big|_{i,1+1/2}+j_{nyS}\Big|_{i+1,1+1/2}-\left(j_{nyS}\Big|_{i-1,1+1/2}+j_{nyS}\Big|_{i,1+1/2}\right)}{2}\\&=\frac{j_{nyS}\Big|_{i+1,1+1/2}-j_{nyS}\Big|_{i-1,1+1/2}}{2}\end{aligned}\tag{212}$$

$$\begin{aligned}j_{nyS}\Big|_{i+1/2,N_y}-j_{nyS}\Big|_{i-1/2,N_y}&=\frac{j_{nyS}\Big|_{i,N_y-1/2}+j_{nyS}\Big|_{i+1,N_y-1/2}-\left(j_{nyS}\Big|_{i-1,N_y-1/2}+j_{nyS}\Big|_{i,N_y-1/2}\right)}{2}\\&=\frac{j_{nyS}\Big|_{i+1,N_y-1/2}-j_{nyS}\Big|_{i-1,N_y-1/2}}{2}\end{aligned}$$

(213)

Therefore, (208) and (209), thanks to (212) and (213) respectively become:

$$\boxed{\begin{gathered}F^{II}_{By1,i}=\frac{j_{nxS}\Big|_{i+1/2,1}-j_{nxS}\Big|_{i-1/2,1}}{\overline{h}_i}-c_{Bn}\frac{j_{nyS}\Big|_{i+1,1+1/2}-j_{nyS}\Big|_{i-1,1+1/2}}{2\overline{h}_i}+\\+2\frac{j_{nyS}\Big|_{i,1+1/2}}{k_1}+2c_{Bn}\frac{\left(j_{nxS}\Big|_{i-1/2,1}+j_{nxS}\Big|_{i-1/2,1+1}\right)h_i+\left(j_{nxS}\Big|_{i+1/2,1+1}+j_{nxS}\Big|_{i+1/2,1}\right)h_{i-1}}{2\left(h_i+h_{i-1}\right)k_1}=\\-r_n\Big|_{i,1}=0\end{gathered}}\qquad j=1$$

(214)

$$\boxed{\begin{gathered}F^{II}_{By2,i}=\frac{j_{nxS}\Big|_{i+1/2,N_y}-j_{nxS}\Big|_{i-1/2,N_y}}{\overline{h}_i}-c_{Bn}\frac{j_{nyS}\Big|_{i+1,N_y-1/2}-j_{nyS}\Big|_{i-1,N_y-1/2}}{2\overline{h}_i}+\\-2\frac{j_{nyS}\Big|_{i,N_y-1/2}}{k_{N_y-1}}-2c_{Bn}\frac{\left(j_{nxS}\Big|_{i-1/2,N_y-1}+j_{nxS}\Big|_{i-1/2,N_y}\right)h_i+\left(j_{nxS}\Big|_{i+1/2,N_y}+j_{nxS}\Big|_{i+1/2,N_y-1}\right)h_{i-1}}{2\left(h_i+h_{i-1}\right)k_{N_y-1}}=\\-r_n\Big|_{i,N_y}=0\end{gathered}}\qquad j=N_y$$

(215)

The same expression can be obtained for the hole continuity equation:

$$\boxed{\begin{aligned} F^{III}_{By1,i} &= \frac{j_{pxS}\big|_{i+1/2,1} - j_{pxS}\big|_{i-1/2,1}}{\overline{h}_i} - c_{Bn}\frac{j_{pyS}\big|_{i+1,1+1/2} - j_{pyS}\big|_{i-1,1+1/2}}{2\overline{h}_i} + \\ +2\frac{j_{pyS}\big|_{i,1+1/2}}{k} + 2c_{Bp}&\frac{\left(j_{pxS}\big|_{i-1/2,1} + j_{pxS}\big|_{i-1/2,1+1}\right)h_i + \left(j_{pxS}\big|_{i+1/2,1+1} + j_{pxS}\big|_{i+1/2,1}\right)h_{i-1}}{2\left(h_i + h_{i-1}\right)k_1} = \\ &-r_p\big|_{i,1} = 0 \end{aligned}} \qquad j = 1 \quad (216)$$

$$\boxed{\begin{aligned} F^{III}_{By2,i} &= \frac{j_{pxS}\big|_{i+1/2,N_y} - j_{pxS}\big|_{i-1/2,N_y}}{\overline{h}_i} - c_{Bn}\frac{j_{pyS}\big|_{i+1,N_y-1/2} - j_{pyS}\big|_{i-1,N_y-1/2}}{2\overline{h}_i} + \\ -2\frac{j_{pyS}\big|_{i,N_y-1/2}}{k} - 2c_{Bn}&\frac{\left(j_{pxS}\big|_{i-1/2,N_y-1} + j_{pxS}\big|_{i-1/2,N_y}\right)h_i + \left(j_{pxS}\big|_{i+1/2,N_y} + j_{pxS}\big|_{i+1/2,N_y-1}\right)h_{i-1}}{2\left(h_i + h_{i-1}\right)k_{N_y-1}} = \\ &-r_p\big|_{i,N_y} = 0 \end{aligned}} \qquad j = N_y$$

(217)

The discretized Poisson's equation and continuity equations have therefore been obtained, both in inside the domain and on its boundaries.

Finally, it is important to obtain the discretized expression of the current densities in order for such quantities to be computed after the problem is numerically solved:

$$j_{nx}\big|_{i-1/2,j} = j_{nxS}\big|_{i-1/2,j} - c_{Bn}\, j_{nyS}\big|_{i-1/2,j} = j_{nxS}\big|_{i-1/2,j} - c_{Bn}\frac{j_{nyS}\big|_{i-1,j+1/2} + j_{nyS}\big|_{i,j+1/2} + j_{nyS}\big|_{i,j-1/2} + j_{nyS}\big|_{i-1,j-1/2}}{4}$$

(218)

$$j_{ny}\big|_{i,j-1/2} = j_{nyS}\big|_{i,j-1/2} + c_{Bn}\, j_{nxS}\big|_{i,j-1/2} = j_{nxS}\big|_{i,j-1/2} + c_{Bn}\frac{\left(j_{nxS}\big|_{i-1/2,j-1} + j_{nxS}\big|_{i-1/2,j}\right)h_i + \left(j_{nxS}\big|_{i+1/2,j} + j_{nxS}\big|_{i+1/2,j-1}\right)h_{i-1}}{2\left(h_i + h_{i-1}\right)}$$

(219)

Thus, for electrons at the position $(i-1/2, j)$:

$$\boxed{j_{nx}\big|_{i-1/2,j} = j_{nxS}\big|_{i-1/2,j} - c_{Bn}\frac{j_{nyS}\big|_{i-1,j+1/2} + j_{nyS}\big|_{i,j+1/2} + j_{nyS}\big|_{i,j-1/2} + j_{nyS}\big|_{i-1,j-1/2}}{4}} \qquad 2 \le j \le N_y - 1$$

(220)

$$\boxed{j_{nx}\big|_{i-1/2,1} = j_{nxS}\big|_{i-1/2,1} - c_{Bn}\frac{j_{nyS}\big|_{i-1,1+1/2} + j_{nyS}\big|_{i,1+1/2}}{2}} \qquad j = 1 \qquad (221)$$

$$\boxed{j_{nx}\Big|_{i-1/2,N_y} = j_{nxS}\Big|_{i-1/2,N_y} - c_{Bn}\frac{j_{nyS}\Big|_{i-1,N_y-1/2} + j_{nyS}\Big|_{i,N_y-1/2}}{2}} \quad j = N_y \qquad (222)$$

$$\boxed{j_{ny}\Big|_{i,j-1/2} = j_{nxS}\Big|_{i,j-1/2} + c_{Bn}\frac{\left(j_{nxS}\Big|_{i-1/2,j-1} + j_{nxS}\Big|_{i-1/2,j}\right)h_i + \left(j_{nxS}\Big|_{i+1/2,j} + j_{nxS}\Big|_{i+1/2,j-1}\right)h_{i-1}}{2\left(h_i + h_{i-1}\right)}}$$

(223)

Similarly, for holes at the position $(i-1/2, j)$:

$$\boxed{j_{px}\Big|_{i-1/2,j} = j_{pxS}\Big|_{i-1/2,j} - c_{Bp}\frac{j_{pyS}\Big|_{i-1,j+1/2} + j_{pyS}\Big|_{i,j+1/2} + j_{pyS}\Big|_{i,j-1/2} + j_{pyS}\Big|_{i-1,j-1/2}}{4}} \quad 2 \le j \le N_y - 1$$

(224)

$$\boxed{j_{px}\Big|_{i-1/2,1} = j_{pxS}\Big|_{i-1/2,1} - c_{Bp}\frac{j_{pyS}\Big|_{i-1,1+1/2} + j_{pyS}\Big|_{i,1+1/2}}{2}} \quad j = 1 \qquad (225)$$

$$\boxed{j_{px}\Big|_{i-1/2,N_y} = j_{pxS}\Big|_{i-1/2,N_y} - c_{Bp}\frac{j_{pyS}\Big|_{i-1,N_y-1/2} + j_{pyS}\Big|_{i,N_y-1/2}}{2}} \quad j = N_y \qquad (226)$$

$$\boxed{j_{py}\Big|_{i,j-1/2} = j_{pxS}\Big|_{i,j-1/2} + c_{Bp}\frac{\left(j_{pxS}\Big|_{i-1/2,j-1} + j_{pxS}\Big|_{i-1/2,j}\right)h_i + \left(j_{pxS}\Big|_{i+1/2,j} + j_{pxS}\Big|_{i+1/2,j-1}\right)h_{i-1}}{2\left(h_i + h_{i-1}\right)}}$$

(227)

On balance, all the discretized equations can be summed up in the following table:

Table 2 Discretized equation summary

Poisson's equation	**(163)**	$\boldsymbol{i = 1, 2, \dots, N_x}$ $\boldsymbol{j = 2, 3, \dots, N_y - 1}$
	(196) (197)	$i = 1,2, \dots, N_x$ $j = 1, N_y$
Electron continuity equation	(178)	$i = 1,2, \dots, N_x$ $j = 2,3, \dots, N_y - 1$
	(214) (215)	$i = 1,2, \dots, N_x$ $j = 1, N_y$
Hole continuity equation	(183)	$i = 1,2, \dots, N_x$ $j = 2,3, \dots, N_y - 1$
	(216) (217)	$i = 1,2, \dots, N_x$ $j = 1, N_y$

Finally, always considering a rectangular geometry, where the sides parallel the x-axis correspond to the metal contacts, the Dirichlet's boundary conditions apply at the mesh points $i = 0, N_x + 1, \forall j$:

$$\begin{cases} \varphi_{0,j} = 0 \\ n_{0,j} = \dfrac{\sqrt{c_A^2 + 4n_i^2} + c_A}{2} \\ p_{0,j} = \dfrac{\sqrt{c_A^2 + 4n_i^2} - c_A}{2} \end{cases} \qquad \begin{cases} \varphi_{N_x+1,j} = V_0 - V_{applied} \\ n_{N_x+1,j} = \dfrac{\sqrt{c_B^2 + 4n_i^2} + c_B}{2} \\ p_{N_x+1,j} = \dfrac{\sqrt{c_B^2 + 4n_i^2} - c_B}{2} \end{cases} \tag{228}$$

3.6 Solving nonlinear systems of algebraic equations

Once the semiconductor equations have been discretized they give birth to a system of $3N_x \cdot N_y$ nonlinear algebraic equations with $3N_x \cdot N_y$ unknowns (i.e. $\varphi_{i,j}, n_{i,j}, p_{i,j}$ for $i = 1,2,\dots,N_x \;\; j = 1,2,\dots,N_y$), where N is the number of mesh points. In general, only iterative methods are applicable for the solution of systems of nonlinear algebraic equations. The most important method, without any doubt, is the Newton's method with some modifications.

The Newton's method modified according to the Gummel's algorithm to solve semiconductor equations in 1 dimension has already been described in [24]. The 2-dimensional case only represents its natural extension. It's fundamental to bear in mind that, given the particular form of semiconductor equations, Gummel's algorithm, beyond the improving effect it has on the convergence properties of the solver, is fundamental in order to solve the problem within an acceptable CPU time.

The basic idea of such algorithm is shifting all the nonlinearities to Poisson's equation, such that the continuity equations becomes linear and decoupled during the iteration process. Skipping all the mathematical passages, after some manipulations, the final form of (163) is:

$$F_{G\,i,j}^{I} = \frac{\dfrac{\varphi_{i+1,j}^{[k]} - \varphi_{i,j}^{[k]}}{h_i} - \dfrac{\varphi_{i,j}^{[k]} - \varphi_{i-1,j}^{[k]}}{h_{i-1}}}{\dfrac{h_i + h_{i-1}}{2}} + \frac{\dfrac{\varphi_{i,j+1}^{[k]} - \varphi_{i,j}^{[k]}}{k_j} - \dfrac{\varphi_{i,j}^{[k]} - \varphi_{i,j-1}^{[k]}}{k_{j-1}}}{\dfrac{k_j + k_{j-1}}{2}} - n_{i,j}^{[k-1]} e^{\varphi_{i,j}^{[k]} - \varphi_{i,j}^{[k-1]}} + p_{i,j}^{[k-1]} e^{\varphi_{i,j}^{[k-1]} - \varphi_{i,j}^{[k]}} - c_{i,j} = 0 \tag{229}$$

where k is the number of the current iteration step. While the electron continuity equation becomes:

$$\boxed{F^{II}_{G\,i,j} = F^{II}_{i,j}\left(\varphi^{[k]}, n^{[k]}, p^{[k-1]}\right)} \tag{230}$$

In particular, it easy to notice that (230) is a linear and decoupled equation where the only unknown is $n^{[k]}$. Analogously, the hole continuity equation becomes:

$$\boxed{F^{III}_{G\,i,j} = F^{III}_{i,j}\left(\varphi^{[k]}, n^{[k]}, p^{[k]}\right)} \tag{231}$$

Again, (231) is a linear and decoupled equation where the only unknown is $p^{[k]}$.

The same manipulation happens to the discretized equations at the insulating boundaries. i.e, as far as Poisson's equation is concerned:

$$\boxed{\begin{aligned} F^{I}_{G,By2} = & \frac{\dfrac{\varphi^{[k]}_{i+1,N_y} - \varphi^{[k]}_{i,N_y}}{h_i} - \dfrac{\varphi^{[k]}_{i,N_y} - \varphi^{[k]}_{i-1,N_y}}{h_{i-1}}}{\dfrac{h_i + h_{i-1}}{2}} + \\ & \frac{2B}{\sigma_{nH} + \sigma_{pH}}\left(\mu_{Hn}\frac{j_{nxS}\big|_{i-1/2,N_y}\left(\varphi^{[k-1]}, n^{[k-1]}\right) + j_{nxS}\big|_{i+1/2,N_y}\left(\varphi^{[k-1]}, n^{[k-1]}\right)}{2} + \mu_{Hp}\frac{j_{pxS}\big|_{i-1/2,N_y}\left(\varphi^{[k-1]}, n^{[k-1]}\right) + j_{pxS}\big|_{i+1/2,N_y}\left(\varphi^{[k-1]}, n^{[k-1]}\right)}{2}\right) + \\ & \frac{+2\dfrac{\varphi^{[k]}_{i,N_y} - \varphi^{[k]}_{i,N_y-1}}{k_{N_y-1}}}{k_{N_y-1}} - n^{[k]}_{i,N_y} e^{\varphi^{[k]}_{i,N_y} - \varphi^{[k-1]}_{i,N_y}} + p^{[k]}_{i,N_y} e^{\varphi^{[k-1]}_{i,N_y} - \varphi^{[k]}_{i,N_y}} - c_{i,N_y} = 0 \end{aligned}} \tag{232}$$

$$\boxed{\begin{aligned} F^{I}_{G,By1} = & \frac{\dfrac{\varphi^{[k]}_{i+1,1} - \varphi^{[k]}_{i,1}}{h_i} - \dfrac{\varphi^{[k]}_{i,1} - \varphi^{[k]}_{i-1,1}}{h_{i-1}}}{\dfrac{h_i + h_{i-1}}{2}} \\ & \frac{2B}{\sigma_{nH} + \sigma_{pH}}\left(\mu_{Hn}\frac{j_{nxS}\big|_{i-1/2,1}\left(\varphi^{[k-1]}, p^{[k-1]}\right) + j_{nxS}\big|_{i+1/2,1}\left(\varphi^{[k-1]}, p^{[k-1]}\right)}{2} + \mu_{Hp}\frac{j_{pxS}\big|_{i-1/2,1}\left(\varphi^{[k-1]}, p^{[k-1]}\right) + j_{pxS}\big|_{i+1/2,1}\left(\varphi^{[k-1]}, p^{[k-1]}\right)}{2}\right) \\ & \frac{+2\dfrac{\varphi^{[k]}_{i,2} - \varphi^{[k]}_{i,1}}{k_1}}{k_1} - n^{[k]}_{i,1} e^{\varphi^{[k]}_{i,1} - \varphi^{[k-1]}_{i,1}} + p^{[k]}_{i,1} e^{\varphi^{[k-1]}_{i,N_y} - \varphi^{[k]}_{i,N_y}} - c_{i,1} = 0 \end{aligned}} \tag{233}$$

Similarly, the continuity equations at the insulating boundaries become:

$$F^{II}_{G\,By1,i} = F^{II}_{G\,By1,i}\left(\varphi^{[k]}, n^{[k]}, p^{[k-1]}\right) \tag{234}$$

$$F^{II}_{G\,By2,i} = F^{II}_{G\,By2,i}\left(\varphi^{[k]}, n^{[k]}, p^{[k-1]}\right) \tag{235}$$

$$F^{III}_{G\,By1,i} = F^{III}_{GBy1,i}\left(\varphi^{[k]}, n^{[k]}, p^{[k]}\right) \tag{236}$$

$$F^{III}_{G\,By1,i} = F^{III}_{GBy1,i}\left(\varphi^{[k]}, n^{[k]}, p^{[k]}\right) \tag{237}$$

The following figure depicts the main steps of such algorithm:

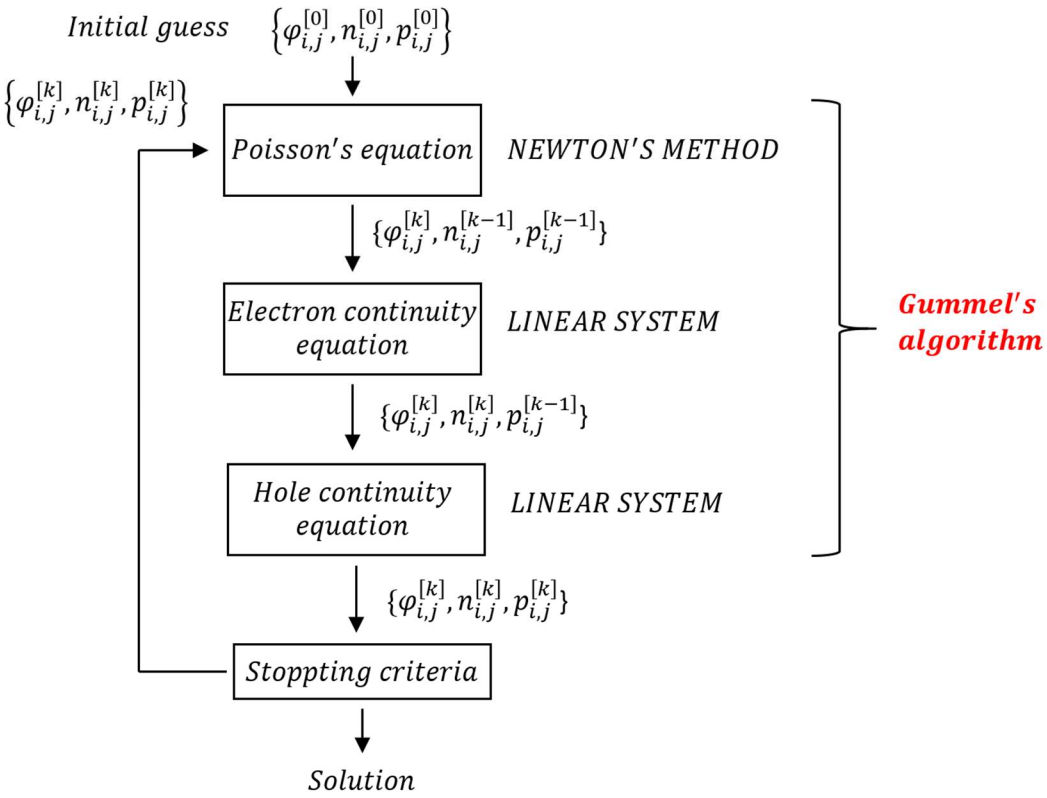

Fig. 12 Gummel's algorithm block scheme

4 Simulations and results

This section aims at presenting the main results of the entire task and it is divided in two parts: the first one deals with the simulation of what could be seen as diodes for signal applications, (i.e. a PN junction), the second one addresses the analysis of power diodes (i.e. a PIN junction); such devices are permeated by an ESMF in both cases.

In particular, the first section deals with a more simplified device. Firstly, this section aims at validating the model and the code. Secondly, it aims at showing which are the macro-effects of an ESMF on semiconductor technology based - devices.

As regards the second section, many approximations and simplifying assumptions are removed and the focus is shifted on power devices.

It is important to recall the simplifying assumptions that have been made in order to carry out the simulations (valid in both cases):

- The device is simulated in 2D on the x-y plane.
- The geometry of the device section is rectangular.
- The device is simulated in steady state operating conditions.
- All the dependencies of the parameters on the variables n, p, φ (electron concentration, hole concentration and electric voltage) are neglected, therefore, such parameters are assumed to be constant with respect to those quantities.
- The temperature is assumed to uniform throughout the device.
- The magnetic field is assumed to be uniform and parallel to the z-axis.
- The considered device is a diode.

It is crucial to notice that these assumptions are somehow consistent with one another, i.e. a rectangular geometry is a good approximation in simulating diodes in 2D, a uniform temperature is a good approximation in steady state operating conditions (as the current density is supposed to be uniform in the device) and finally, the assumption related to the magnetic field is a conservative assumption, (as conservative will be the values chosen for the parameters assumed to be constant).

Besides, it is fundamental to understand that although the device under consideration is a diode (i.e. a simple PN junction in signal applications and a PIN junction in power applications) the results obtained are significant also for many other types of semiconductor devices in general operating in steady state, like thyristors, GTO, IGBT, BJT etc. Indeed, their internal structure is built up on two

or more PN (or PIN) junctions, which then represent the basic element of such devices. Please refer to the following figures just as a simple explanatory example:

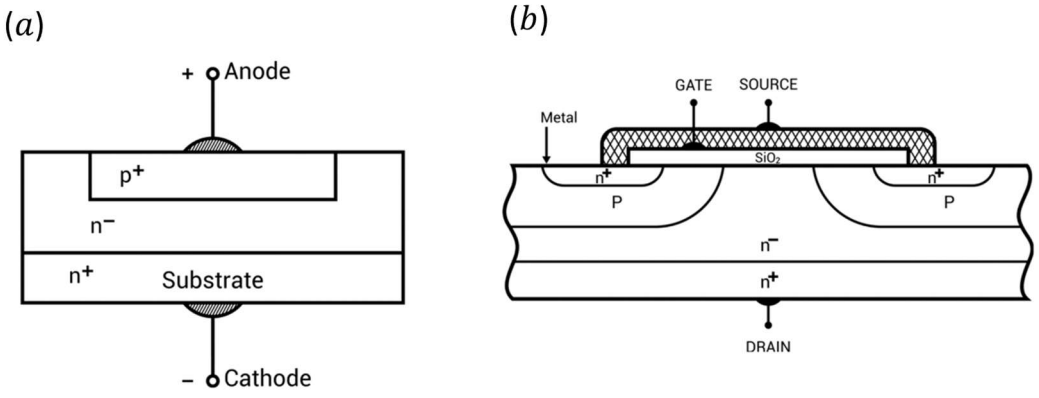

Fig. 13 Power Diode (a), Power MOSFET (b)

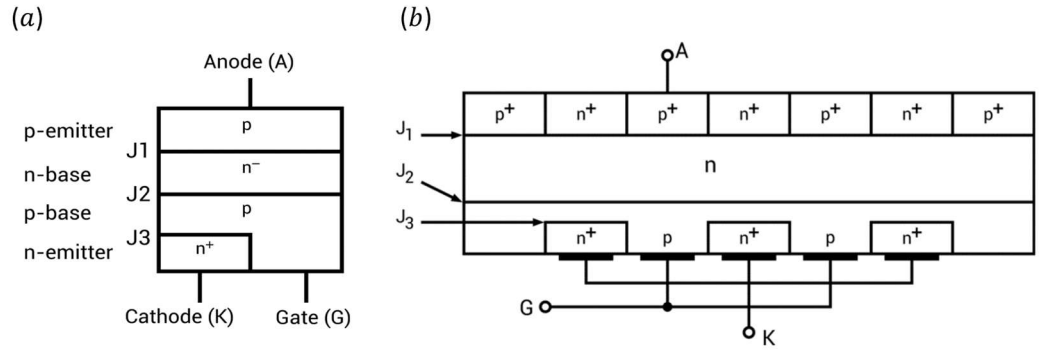

Fig. 14 Power Bipolar Transistor (a), Insulated gate bipolar transistor (IGBT)

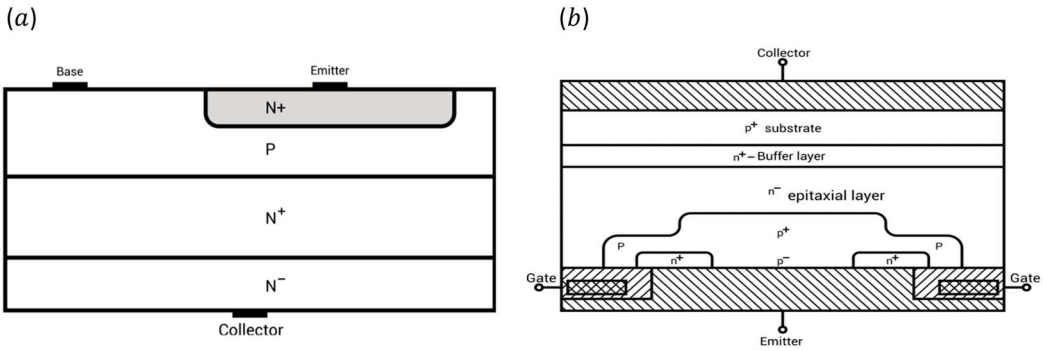

Fig. 15 Thyristor (a), Gate turn-off thyristor (GTO)

Indeed, except for merely analysing the behaviour of diodes affected by an ESMF, these simulations shed light on two main aspects:

- The basic phenomena which arise when a solid state device operates in a static magnetic field – polluted environment are explained (phenomena

which are not peculiar of the specific device, but more in general of the interaction between semiconductor technology and a static magnetic field).

- By addressing the basic element of the most common solid state devices (i.e. the PN or the PIN junction), at least in steady state, these results establish an order of magnitude of the impact of an ESMF on other typologies of devices, especially thyristors. However, it cannot be stated the same is true in a dynamic operating condition, where each case should be addressed independently, as many other factors come into play.

In addition, steady state simulations of rectifier diodes and thyristors are anyway meaningful, as their total power loss in normal operating conditions is mainly given by the on-state loss.

A final crucial remark must be made: understanding which are the main phenomena arising when a semiconductor device operates in an environment permeated by a static magnetic field leads the way in making meaningful experimental tests. As a matter of fact, it offers resourceful insights to design tests targeting specific phenomena, therefore, it enables the evaluation of their potentially critical impacts, which otherwise could be neglected or not even be taken in consideration without that "a-priori" knowledge.

4.1 PN junction simulations

This first set of simulation is carried out considering an operating temperature equal to what is considered the room temperature when the nominal carrier mobility value of Silicon are given [32]. A very precise value for the carrier lifetime is impossible to give, however, a reasonable order of magnitude is given in Table 3. Finally, in order to be able to make a fair comparison of the simulated I-V curves with the one obtained through the analytical formula, one has to choose a step dopant concentration profile of the form:

$$c(x)=\frac{1}{2}\left[N_d-N_a+\left(N_d+N_a\right)\mathrm{sgn}(x)\right] \tag{238}$$

Where $sgn(x)$ is the "sign" function defined as:

$$\mathrm{sgn}(x)=\begin{cases}1 & x\geq 0\\ -1 & x<0\end{cases} \tag{239}$$

Please note that (238) implies that the interface between the p-side and the n-side is at $x = 0$. Although usually N_d and N_a can be substantially different, the same value has been chosen for them in order to enhance the symmetry of the problem.

Another important remark regards the function (238). Usually, a uniform dopant profile is a quite rough approximation and generally Gaussian dopant profiles are assumed, however, as it is mentioned above, (238) is also the form assumed in the procedure to obtain the diode analytical formula, thus, a fair comparison requires it. This approximation is removed in the power diode section.

Table 3 Numerical values of parameters

Name	Symbol	Value
Device temperature	T	$25\ [°C]$
Electron mobility	μ_n	$1360\ [\frac{cm}{V \cdot s}]$
Hole mobility	μ_p	$495\ [\frac{cm}{V \cdot s}]$
Electron lifetime	τ_n	$5 \cdot 10^{-5}\ [s]$
Hole lifetime	τ_p	$1 \cdot 10^{-6}\ [s]$
Device length (x direction)	L_x	$2\ [mm]$
Device width (y direction)	L_y	$5\ [mm]$
Acceptor atom concentration	N_a	$10^{16}\ [cm^{-2}]$
Donor atom concentration	N_d	$10^{16}\ [cm^{-2}]$

Finally, the device length has been chosen such that the carriers recombine completely through the junction, leaving a negligible amount of carriers recombining at the metal contacts, i.e. a long base diode is chosen. The results are presented as follows: firstly the "internal behaviour" of device is described, secondly the "external behaviour" is analysed.

4.1.1 Internal Behavior

The dependent variables are shown first (i.e. the electric voltage, the electron concentration and the hole concentration), lastly the post-processed quantities are presented (i.e. the electron current density, the hole current density and the total current density).

A comparison between the operating condition at $B = 0\,T$ and $B = 2\,T$ for $V_{applied} = 0.55\,V$ is made.

It is clear to observe from the second panel Fig. 17 that the contour lines are characterized by a slight deflection compared to the second panel of Fig. 16, therefore, a Hall effect arises due to the presence of an ESMF.

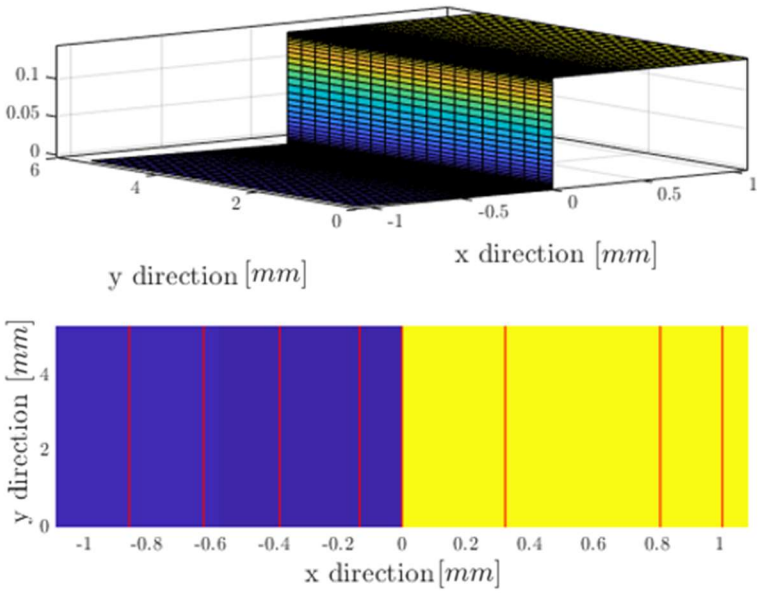

Fig. 16 Electric voltage for $\boldsymbol{V_{applied} = 0.55\,V}$ *and* $\boldsymbol{B = 0\,T}$

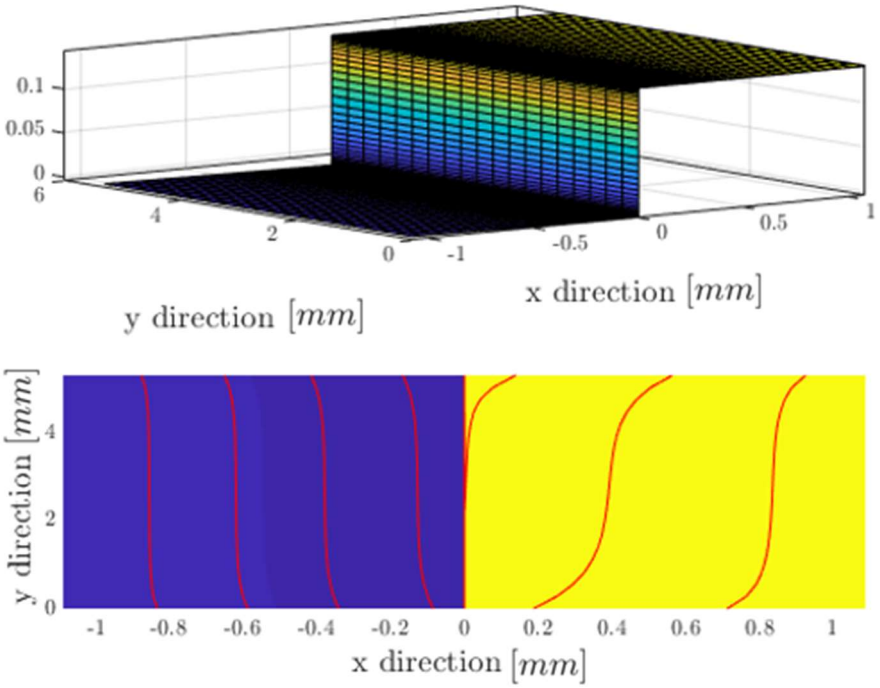

Fig. 17 Electric voltage for $\boldsymbol{V_{applied} = 0.55\ V}$ *and* $\boldsymbol{B = 2\ T}$

Analysing both the electron and the hole concentration one can appreciate what can be defined as a "magneto-concentration" effect. In other terms, in order to balance Lorentz's force acting on moving carriers, not only a Hall effect arises, but also, carriers are pushed towards one side of the device and their concentration increases there.

In particular, one can simply observe from Fig. 19 and Fig. 21 that the electron and hole concentration build up at the lower side of the device.

Again, in order to make a clear comparison, first the case is shown where no magnetic field is present and after, the operating condition at $B = 2\ T$. It has been chosen to show this particular operating condition, where the magnetic field is much greater than $70\ mT$ only because the magneto-concentration effect and the hall effect are graphically observable in in this situation.

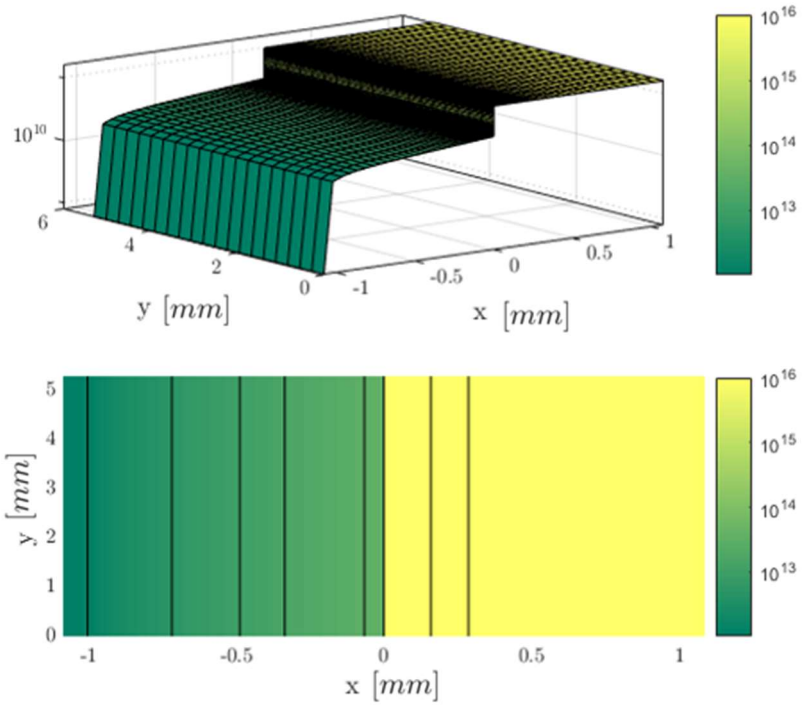

Fig. 18 Electron concentration in $\mathbf{1/cm^2}$ *for* $\boldsymbol{V_{applied} = 0.55\,V}$ *and* $\boldsymbol{B = 0\,T}$

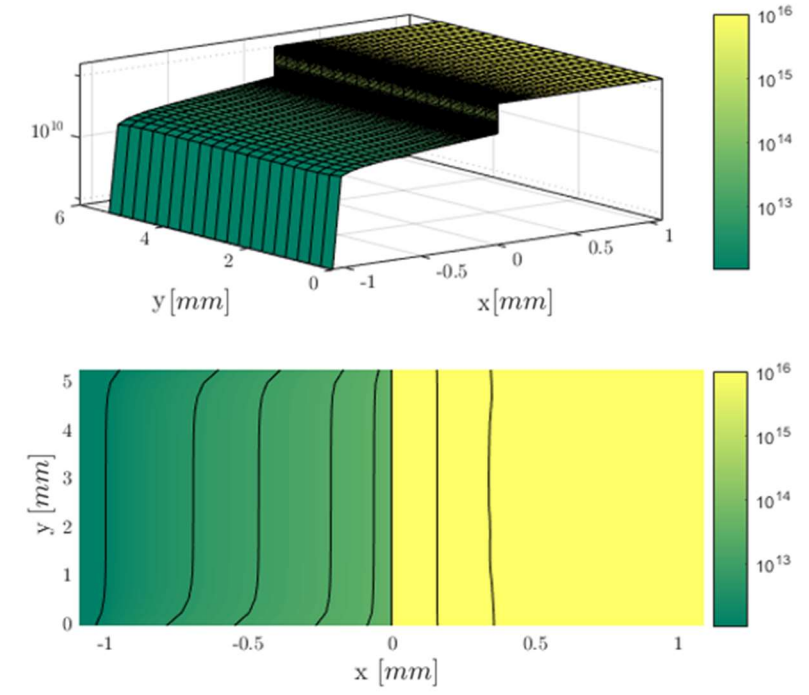

Fig. 19 Electron concentration in $\mathbf{1/cm^2}$ *for* $\boldsymbol{V_{applied} = 0.55\,V}$ *and* $\boldsymbol{B = 2\,T}$

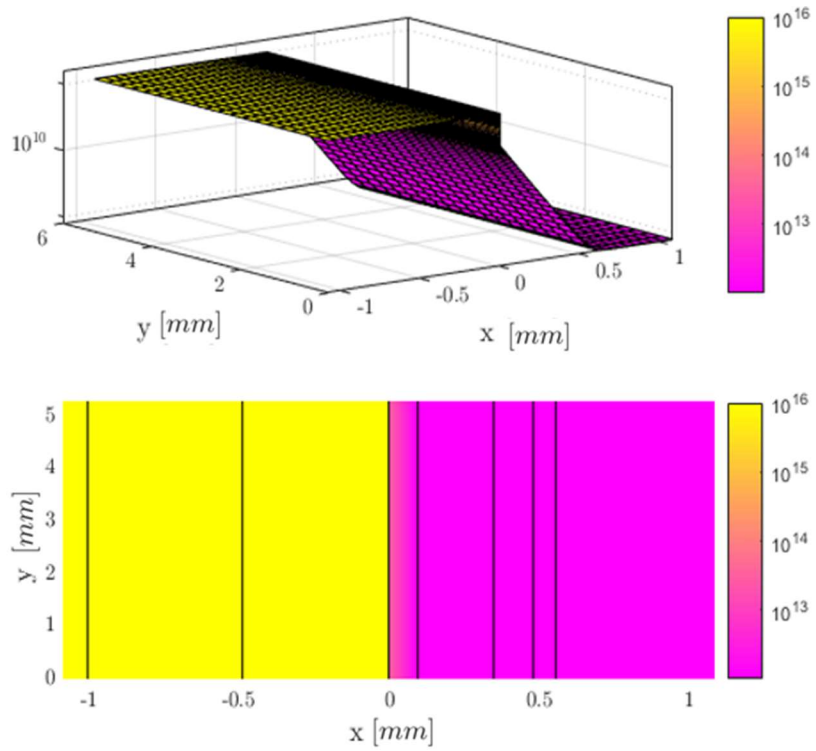

Fig. 20 Hole concentration in $\mathbf{1/cm^2}$ *for* $\boldsymbol{V_{applied} = 0.55\ V}$ *and* $\boldsymbol{B = 0\ T}$

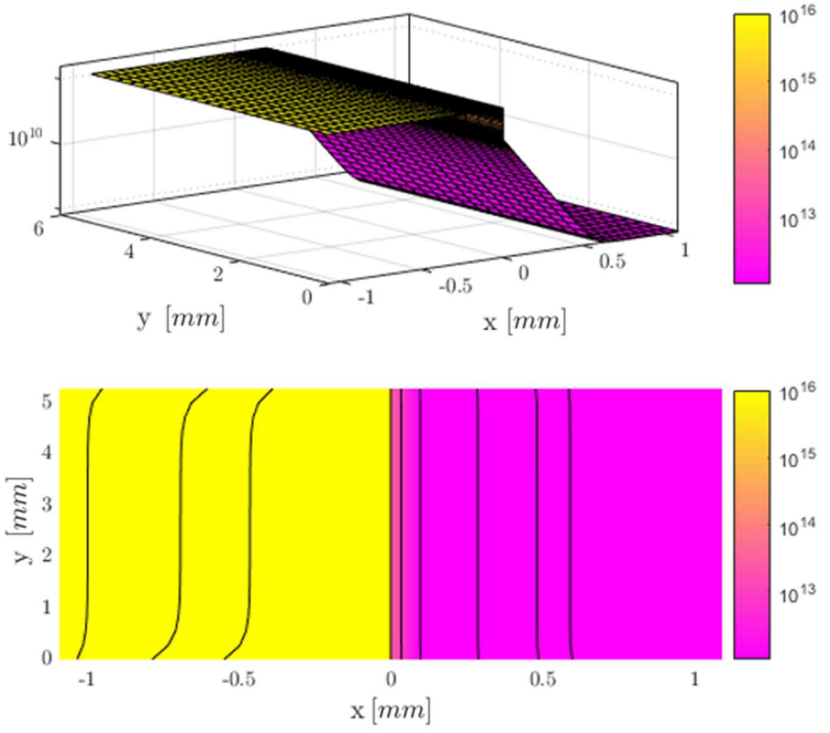

Fig. 21 Hole concentration in $\mathbf{1/cm^2}$ *for* $\boldsymbol{V_{applied} = 0.55\ V}$ *and* $\boldsymbol{B = 2\ T}$

As regards the current density, one can notice from Fig. 22 that the findings reported in [1] are confirmed. Indeed, a non-uniform current density flows through

the junction due to the ESMF (being not a meaningful plot, the uniform current density when no ESMF is applied is not shown).

As a matter of fact, such non-uniformity is due to the carrier deflection caused by Lorentz's force. More specifically, this becomes more relevant by looking at the current streamlines in the n-side, where the majority carriers are electrons whose mobility is here more than twice the holes. This fact confirms what has been previously anticipated, i.e. a smaller value of the carrier mobilities makes the entire device more immune to an ESMF. The particular "V" shape of the current streamlines is explained some pages ahead.

In addition to that, not only a potentially critical area of higher current density is caused by carrier deflection, but also, as the carriers take longer paths when flowing through the device the overall resistivity increases, giving birth to a phenomenon called "magneto-resistance" effect.

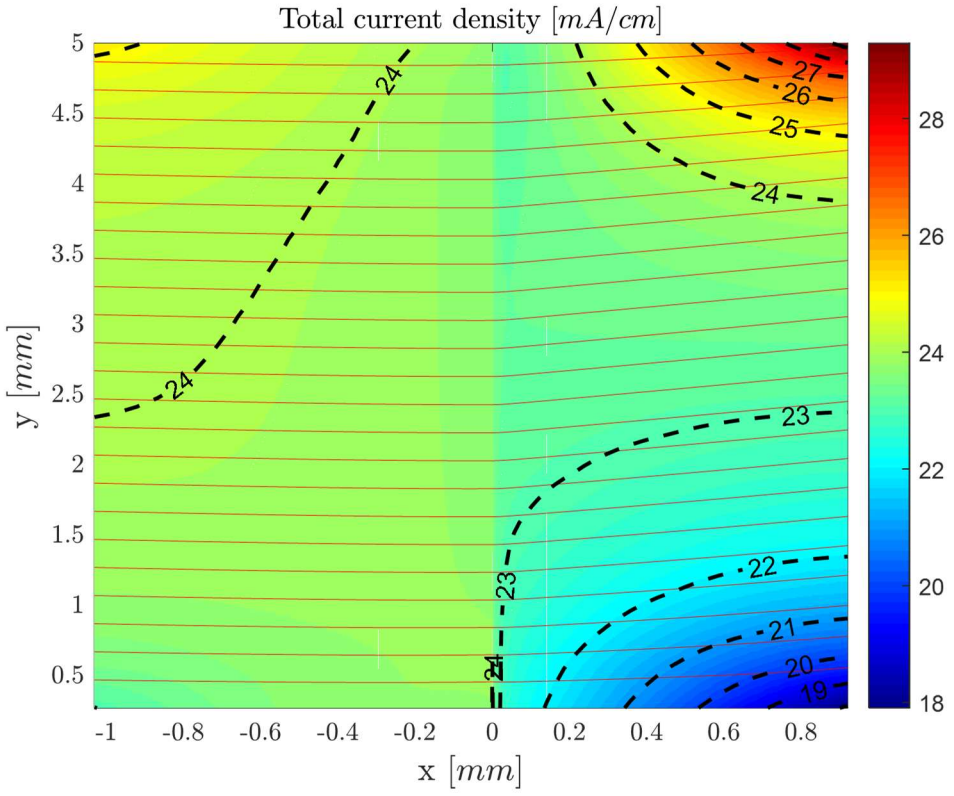

Fig. 22 Total current density for $\boldsymbol{V_{applied} = 0.55\ V}$ *and* $\boldsymbol{B = 2\ T}$

It is of primary importance to notice the "asymmetry" is due to the different mobility values of hole and electrons. More specifically, at room temperature and with light doping one has $\mu_n \cong 3\mu_p$, this implies that the portion of the device where electron carriers dominate, is more sensitive to the ESMF.

In other words, the impact of the magnetic field on that portion of device is roughly 3 times higher (at least in this simulation).

In other and more realistic conditions the values of carrier mobilities may vary significantly from the silicon "nominal" values and they also depend on the position considered inside the device. However, in general, electron mobility remains higher than hole mobility, making the electron-dominated areas more sensitive than others.

Electron and hole current densities are shown separately in Fig. 23. It is immediate to appreciate in this figure what is mentioned above. Indeed, the electron current density exhibits a higher non-uniformity in the n-side compared to the hole current density in the p-side, showing the higher sensitivity of electrons to the action of an external magnetic field.

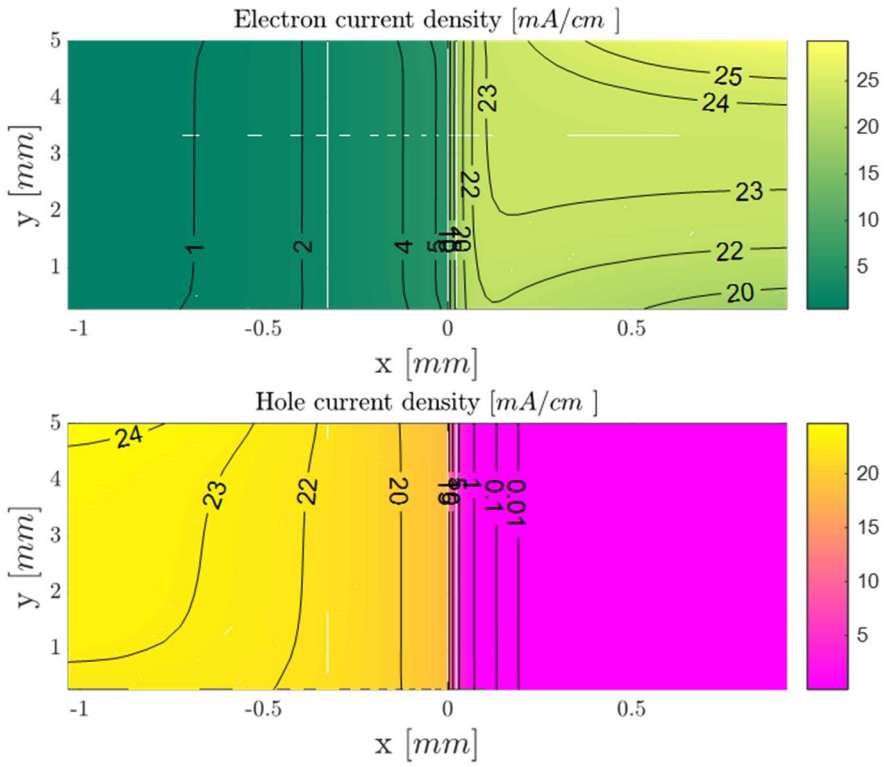

Fig. 23 Electron and hole current density for $\boldsymbol{V_{applied} = 0.55\ V}$ *and* $\boldsymbol{B = 2\ T}$

Being $\underline{B}$ positive and parallel to the z-axis, by simply applying the right-hand rule to identify the direction of Lorentz's force, it is immediate to verify that both holes and electrons are pushed towards the lower edge, as they have opposite sign and opposite speed direction (see Fig. 24 and Fig. 25).

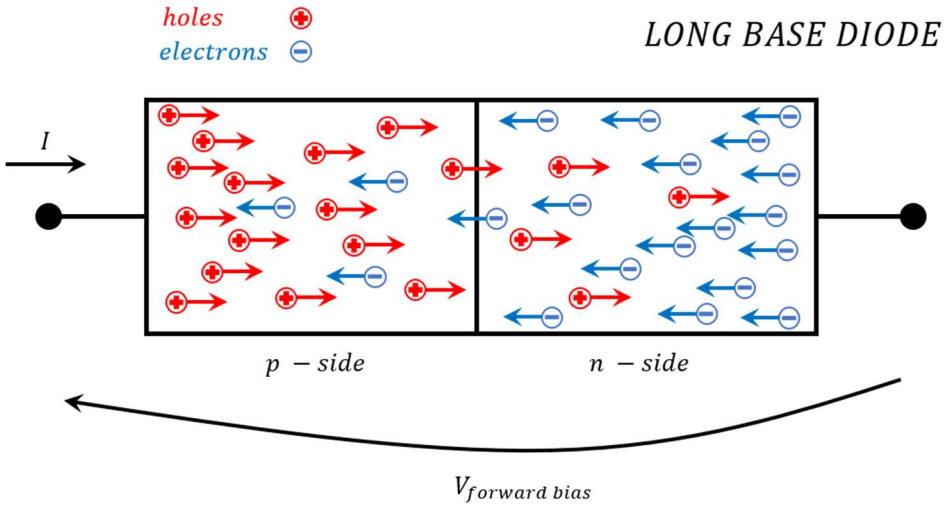

Fig. 24 Moving carriers in a long base PN junction in absence of any magnetic field

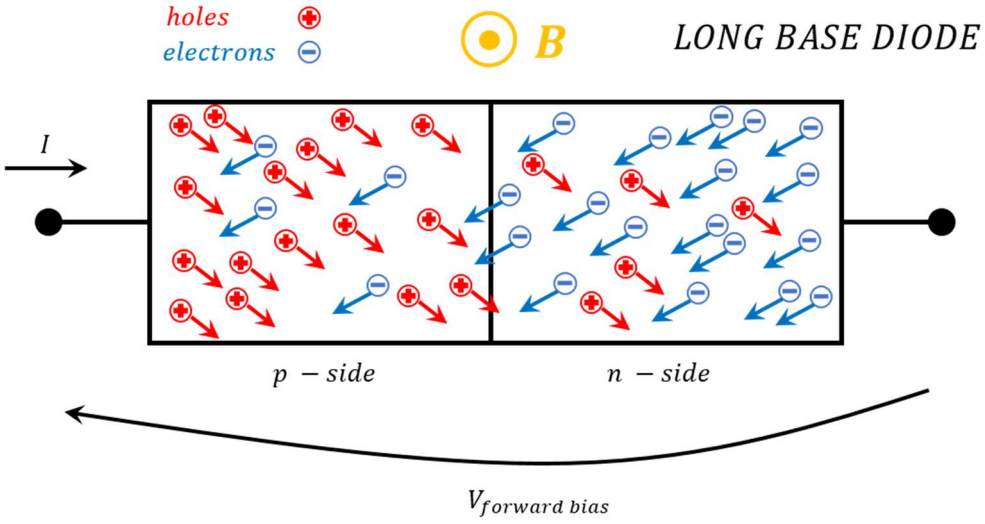

Fig. 25 Moving carriers in a long PN junction in the presence of an external magnetic field

Besides, that explains also why the current streamlines in Fig. 22 show a V-shape deflection. By simply summing the electron and hole current of Fig. 24, Fig. 26 is obtained, whereas, by summing the electron and hole current of Fig. 25, one has Fig. 27.

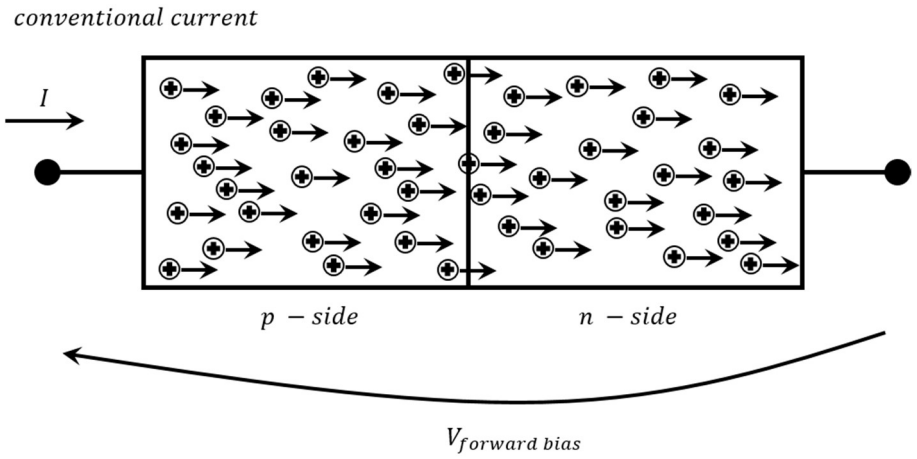

Fig. 26 Total current in a long base PN junction in absence of any magnetic field

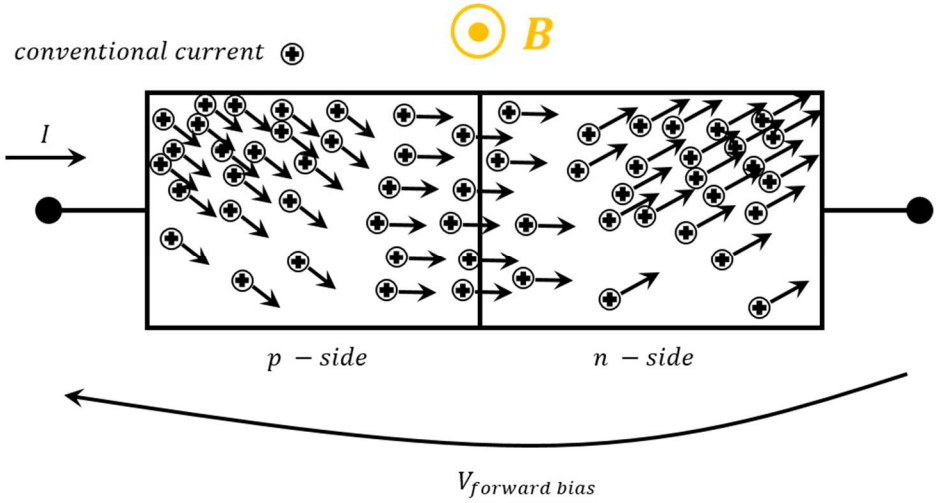

Fig. 27 Total current in a long base PN junction in the presence of an external magnetic field

Finally, Fig. 28 shows the adopted mesh. As it is mentioned above it presents a high non-uniformity along the x-direction, while it is kept uniform along the y-direction. This particular mesh is formed by $20 \times 13320 = 2660$ mesh points.

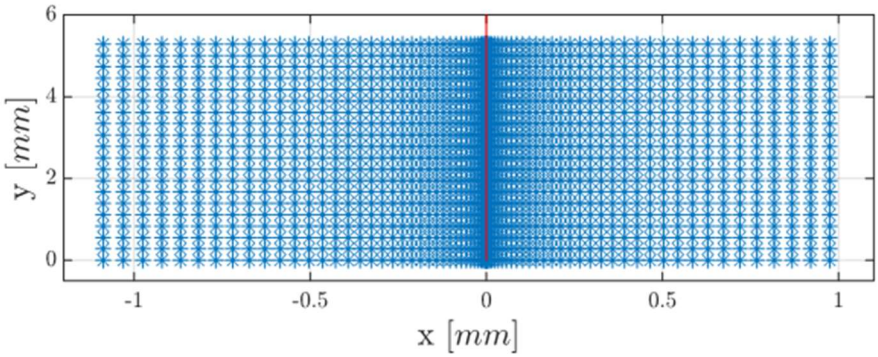

Fig. 28 Mesh

4.1.2 External Behavior

By applying different values of both external voltage, different I-V characteristics can be obtained, each one of them for a specific value of ESMF. Therefore, the first step is to set $B = 0$ and compare the simulated curve with the one given by the typical diode formula, in order to validate the results of the simulation itself. The I-V curves for 5 values of ESMF have been obtained thanks to 60 simulations in a row and they are shown in Fig. 29.

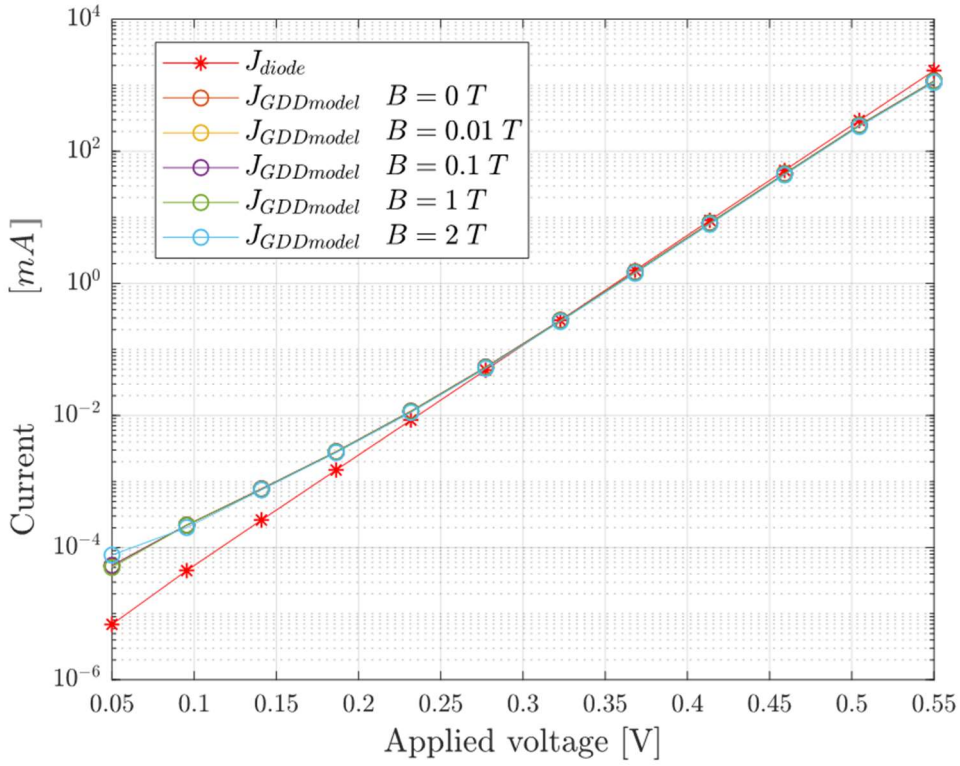

Fig. 29 I-V curves for different values of external magnetic field

Please note that the current density plotted in Fig. 29 is computed as follows:

$$J_{diode}\left(V_{bias}\right) = L_y \cdot J_s\left(e^{V_{bias}/U_t} - 1\right) \tag{240}$$

As far as the diode formula is concerned, where:

$$J_s = q\left[\frac{D_n n_{p0}}{L_n} coth\left(\frac{w_p}{L_n}\right) + \frac{D_p p_{n0}}{L_p} coth\left(\frac{w_n}{L_p}\right)\right] \tag{241}$$

While the total current flowing through the junction is simply:

$$J_{GDD\,\mathrm{model}} = \int_0^{L_y} J_x\left(x, y\right) dy \tag{242}$$

at any section of the junction. In particular J_x is the x-component of the current density vector $\underline{J}(x, y)$. However, being the current density $\underline{J}$ only defined on the mesh points, it implies that its x and y-components are matrices (respectively $\boldsymbol{J_x}$ and $\boldsymbol{J_y}$) whose number of elements is equal to the mesh point number. Thus, (242) becomes:

$$J_{GDD\,\mathrm{model}} = \frac{L_y}{N_y - 1}\sum_{j=1}^{N_y} J_x^{\{i,j\}} \tag{243}$$

Where $J_x^{\{i,j\}}$ is the (i, j) element of the matrix $\boldsymbol{J_x}$ where $i = 1,2, \ldots, N_y$ and $j = 1,2, \ldots, N_x$. Theoretically, the current computed thanks to (243) in a rectangular geometry should be the same, regardless of the section chosen (i.e. the continuity equation must hold), however, due to numerical errors, a better procedure is calculate the current in each section (i.e. for each column j of the matrix $\boldsymbol{J_x}$), and obtaining the final value thorough an arithmetic average, namely:

$$J_{GDD\,\mathrm{model}} = \frac{\sum_{j=1}^{N_x}\left(\frac{L_y}{N_y - 1}\sum_{i=1}^{N_y} J_x^{\{i,j\}}\right)}{N_x} \tag{244}$$

Nonetheless, it is of primary importance to verify that the current value computed in each section thanks to (243) does not deviate excessively from the mean (244). Suffice it to say, less the deviation the better, while the higher it gets, the poorer the accuracy of the solution.

Given the y-logscale, it is not possible to appreciate the small shifting of the curves in Fig. 29, however, the magnitude of this shifting becomes higher as the magnetic field intensity increases, indicating an increase in the device resistivity.

Perhaps, a more intuitive and handy way to evaluate this phenomenon is to compute directly additional the power losses determined by the magneto-resistance effect. Hence, thanks to the following simple calculation:

$$\Delta P\%_{loss}\left(B\right)=100\frac{P\left(B\right)-P\left(0\right)}{P\left(0\right)} \tag{245}$$

where $P(B)$ and $P(0)$ are the electrical power flowing through the device in the presence and in absence of an ESMF respectively, the following plot is achieved:

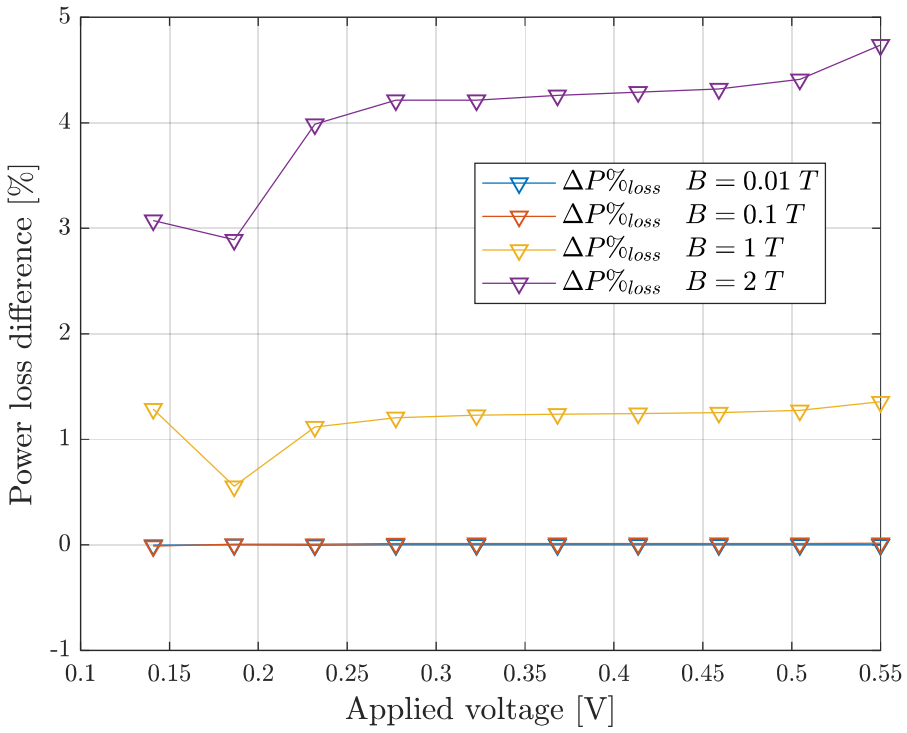

Fig. 30 Additional power loss determined by an ESMF permeating a PN junction in steady state

It is then confirmed that an ESMF determines additional power losses in a semiconductor device via the "magneto-resistance" effect. However, the entity of such effect appears to be negligible at this stage, for magnetic field intensities lower than 1 T.

Another crucial aspect to evaluate is the current density non-uniformity. Indeed, it is necessary to extract some numbers from the qualitative description of Fig. 22.

A simple and effective way to proceed is to identify the maximum value J_M among the elements of the $\boldsymbol{J}_{norm}$ matrix, which is obtained according to:

$$\mathbf{J}_{norm}=\sqrt{\mathbf{J}_x^2+\mathbf{J}_y^2} \tag{246}$$

where the calculation defined by (246) is intended to be element-wise and compare such value with the current density value J_u at the same operating condition with no ESMF (i.e. with the current density values associated with a uniform distribution, which is assumed to be the normal operating condition). Therefore, according to the following straightforward calculation:

$$\Delta J\% = 100\frac{J_M}{J_u} \tag{247}$$

The plot below is obtained:

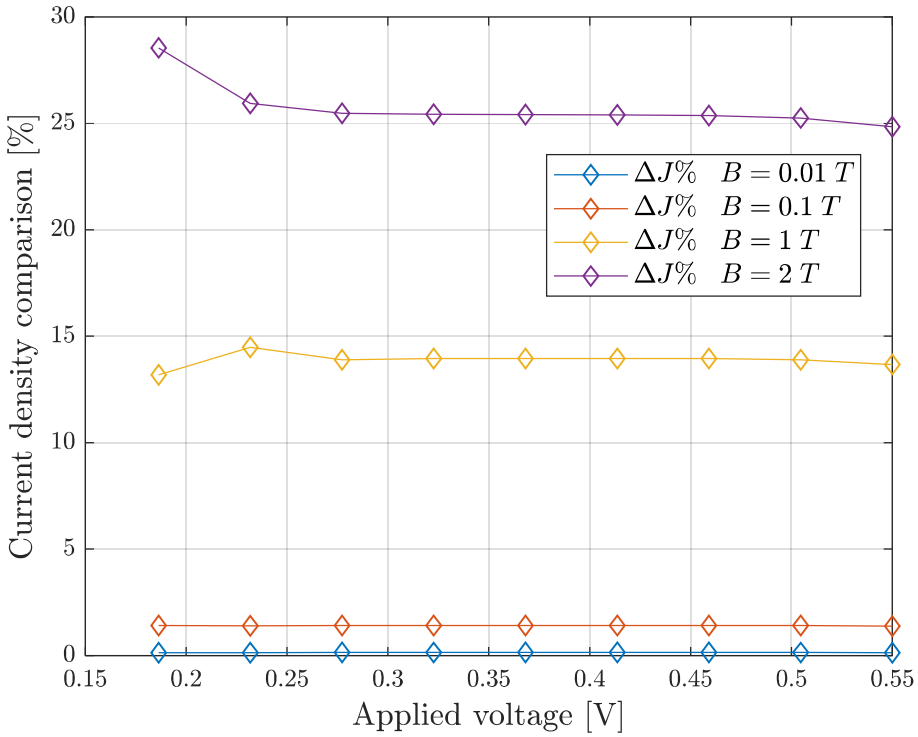

Fig. 31 Current density increase due to an ESMF

It is fundamental to bear in mind that the information available in Fig. 31 are conservative estimation, indeed, since (247) is computed using the maximum value J_M which corresponds to the current density value only on one mesh point. Therefore, by definition, all the other mesh points around it are characterized by a current density value which is lower.

Nevertheless, Fig. 31 (and the following plots obtained likewise) can be interpreted as follows: increased current density regions arise at the insulating boundary of the device, the magnitude of this phenomena primarily depends on the magnetic field intensity and on the carrier mobilities and in particular, conservative values quantifying such increase are given in the plot. More specifically, Fig. 31 shows the results for the PN junction under consideration.

4.1.3 Qualitative conclusions

On balance, as a specific manifestation of the Lorentz force acting on mobile electrons and holes, four basic effects can be assumed to be responsible for magnetic sensitivity in semiconductor devices:

- Hall effect: the production of a voltage difference across the device, transverse to the electric current and the applied ESMF.
- Carrier deflection: deflection of the normal path taken by the carriers in absence of the ESMF.
- Magnetoconcentration: compensation of the Lorentz's force by concentration gradients. This tends to be a greater and greater phenomenon in areas where there is a large build up of mobile charges (for instance at the edge of the depletion region in high injection conditions). On the contrary, no noticeable effect of the magnetic field on net space charge takes place in regions where there is a depletion of carrier concentration.
- Magnetoresistance: increase in the device resistivity. This effect is mainly a consequence of the effects described above. As a matter of fact magnetoresistance basically stems from a longer path taken by carriers through the device and a lower effective section given the accumulation of moving carriers on one side of the device.

All these effects have been found from the simulations described above, in accordance with the theory of "Hall effect devices" [13]. However, a very important aspect couldn't be verified or evaluated thanks to the previous simulation, i.e. the effect of the device geometry on the magnetoresistance effect.

This further phenomenon, known as "geometrical magnetoresistance" is treated in [13] and it is addressed in the next section regarding power diode simulations.

Given the non-realistic doping profile, not an extreme importance should be given to numbers (More quantitative and definitive conclusions are given in the next section where the simulations are characterized by higher degree of realness), however, the data available in Fig. 30 and Fig. 31 can give an order of magnitude of the impact of an ESMF on a semiconductor device.

Thus, it appears that not a serious effect is determined on power losses in steady state operating condition by an ESMF generally lower than $1\ T$, which is already a value more than 10 times higher than the maximum value of magnetic field expected in the crane hall of the Tokamak building. The same is not true if one looks at the current density increase at $1\ T$, however, this phenomenon is anyway greatly reduced at $100\ mT$, causing some current density increase not higher than 2% compared to the case where no ESMF is present.

4.2 PIN junction simulations in forward bias (on-state)

The goal of this section is to present the results related to the power diode simulations, in particular, in addition to quantifying the performance derating of a power diode due to the ESMF, the aim is to evaluate the role played by 3 main variables in affecting the device sensitivity to an ESMF. More specifically these parameters are: device operating temperature, doping levels, geometry.

Many of the simplifying assumptions used in the previous section are removed here, thus, the following phenomena are considered:

- Carrier mobilities and lifetime dependence on temperature (lattice scattering).
- Carrier mobilities and lifetimes dependence on doping concentration (impurity scattering).
- Series resistance effect.
- Gaussian doping profiles.

Therefore, the parameters $\mu_{n,p}$ and $\tau_{n,p}$ are not constant anymore but they change according to the position considered inside the device.

In addition, the mesh has been made non-uniform also along the y-direction in order to compute more accurately the "edge effects". This implies also a slight change in the discretized equations presented above.

Thus, in order to analyse the effect of temperature and device dimensions the following study cases are presented:

1st case: relatively small power device (small dimensions) operating at its max temperature with realistic mobility values conditions (realistic results).

2nd case: relatively small power device (small dimensions) operating at its max temperature with conservative mobility values conditions (conservative results).

3rd case: high power device (big dimensions) operating at its max temperature with realistic mobility values (realistic results).

4th case: high power device (big dimensions) operating at its max temperature with conservative mobility values (conservative results).

Among ones of the more realistic features introduced in the simulations is the gaussian profile of dopant concentration. The term "Gaussian" indicates a Gaussian space distribution of the implanted dopant atoms, which represents a far more realistic modelling of the outcome of this process.

In particular, according to the data provided by POSEICO power electronics, (Italian company manufacturing power diodes and Thyristors), the typical dopant profile of a power diode is the following:

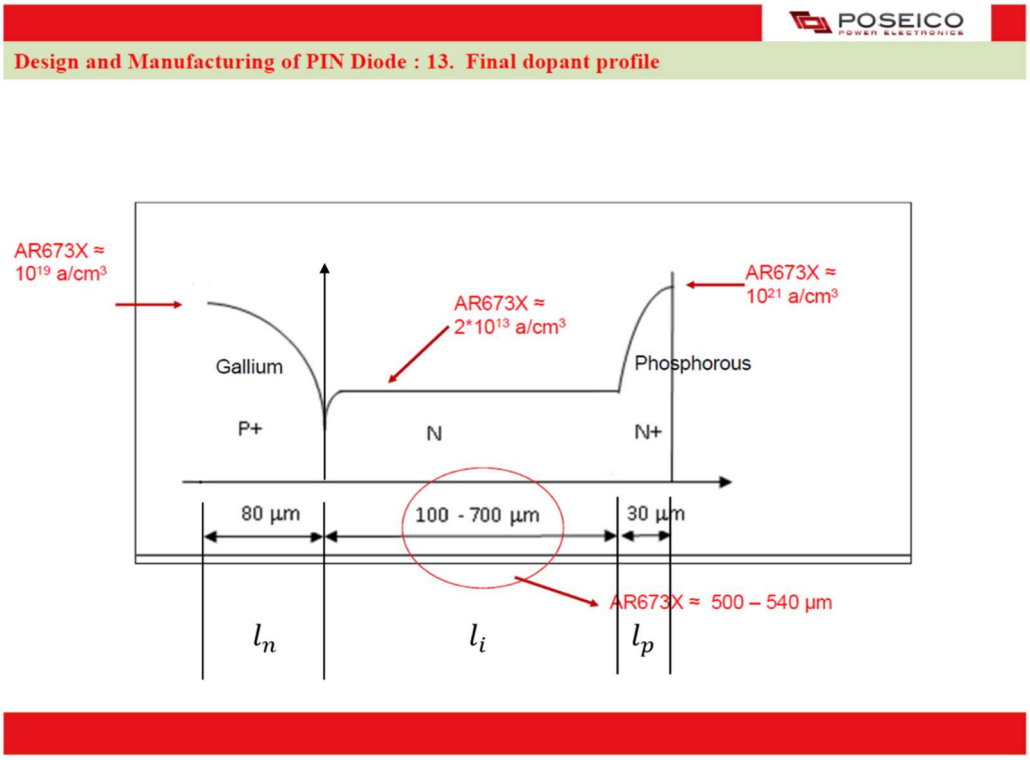

Fig. 32 Typical dopant profile of power diodes

Therefore, the function c in (145) is defined as:

$$c(x,y)=\begin{cases} c_P(x,y) & -l_p \le x \le 0 \quad \forall y \\ c_{N^-}(x,y) & 0 < x \le l_i \quad \forall y \\ c_{N^+}(x,y) & l_i < x \le l_i + l_n \quad \forall y \end{cases} \tag{248}$$

Where:

$$c_P(x,y) = -N_a e^{-B_p\left(x+l_p\right)^2} \tag{249}$$

$$c_{N^-}(x,y) = N_d^- \tag{250}$$

$$c_{N^+}(x,y) = N_d^+ e^{-B_n\left(x-l_i-l_n\right)^2} \tag{251}$$

In which:

$$B_p = \frac{\ln\left(N_a / N_d^-\right)}{l_P^2} \quad , \quad B_n = \frac{\ln\left(N_d^+ / N_d^-\right)}{l_n^2} \tag{252}$$

The mobility and carrier lifetime dependence on temperature and dopant concentration is modelled as follows [24]:

$$\mu_{n,p}^L = \mu_{0n,p}^L \left(\frac{300}{T}\right)^{\alpha_{n,p}} \tag{253}$$

$$\tau_{n,p}^L = \tau_{0n,p}^L \left(\frac{300}{T}\right)^{\gamma_{n,p}} \tag{254}$$

Where T is the temperature in K, $\mu_{0n,p}$ are the room temperature values of the electron and hole mobility, while $\tau_{0n,p}$ are the room temperature values of the electron and hole lifetimes. The final mobility and lifetime values, considering also dopant concentration are given by [24]:

$$\mu_n = \mu_{n,\min} + \frac{\mu_n^L - \mu_{n,\min}}{1 + \frac{\left(N_a + N_d\right)^{\beta_n}}{C_n^{ref}}} \tag{255}$$

$$\mu_p = \mu_{p,\min} + \frac{\mu_p^L - \mu_{p,\min}}{1 + \frac{\left(N_a + N_d\right)^{\beta_p}}{C_p^{ref}}} \tag{256}$$

$$\tau_n = \frac{\tau_n^L}{1 + \frac{N_a + N_d}{N_n^{ref}}} \tag{257}$$

$$\tau_p = \frac{\tau_p^L}{1 + \frac{N_a + N_d}{N_p^{ref}}} \tag{258}$$

Many references are available for the numerical values of the parameters $\alpha_{n,p}, \gamma_{n,p}, \beta_{n,p}, C_{n,p}^{ref}$ and $N_{n,p}^{ref}$. The following values are chosen here:

Table 4 Parameter values for the mobility and lifetime dependencies on temperature and dopant concentration

α_n	2.2	β_p	0.61
α_p	2.2	C_n^{ref}	$1.3 \cdot 10^{17}$
γ_n	2.5	C_p^{ref}	$2.4 \cdot 10^{17}$
γ_p	2.5	N_n^{ref}	$7.42 \cdot 10^{16}$
β_n	0.91	N_p^{ref}	$7.42 \cdot 10^{16}$

It is easy to observe that both the carrier mobilities and the carrier lifetimes decrease with increasing temperature and dopant concentration. For a clearer understanding of such phenomenon please refer to [24]. The following plots can perhaps show more intuitively the effect of temperature and dopant concentration on the hole and electron mobilities:

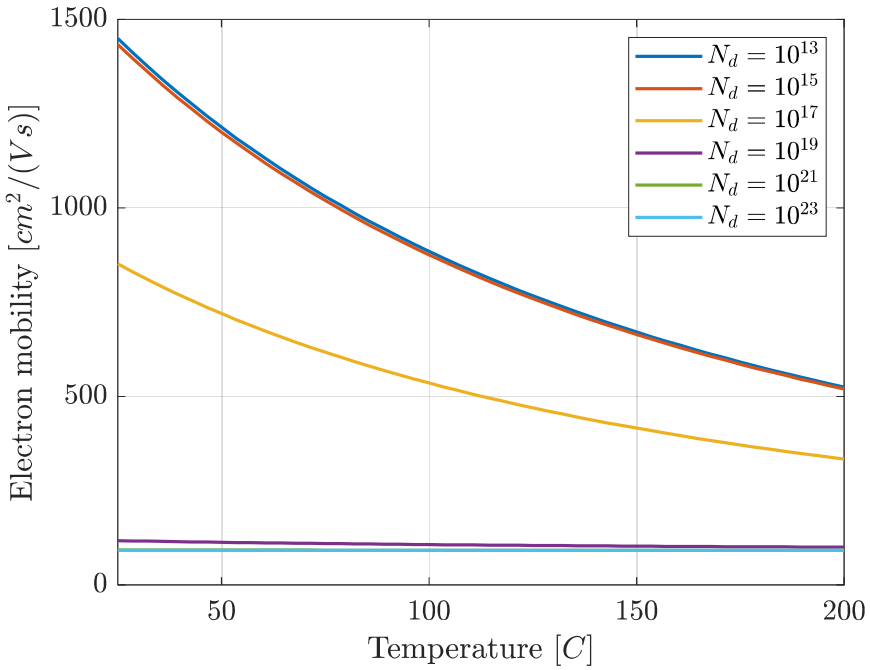

Fig. 33 Electron mobility as a function of temperature

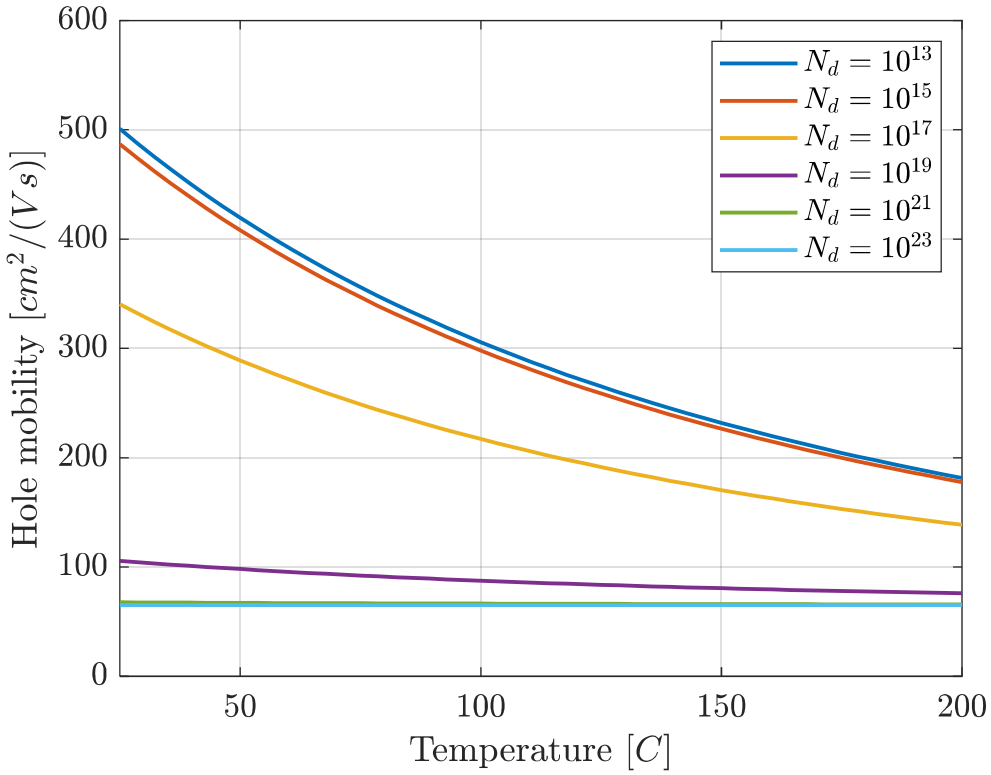

Fig. 34 Hole mobility as a function of temperature

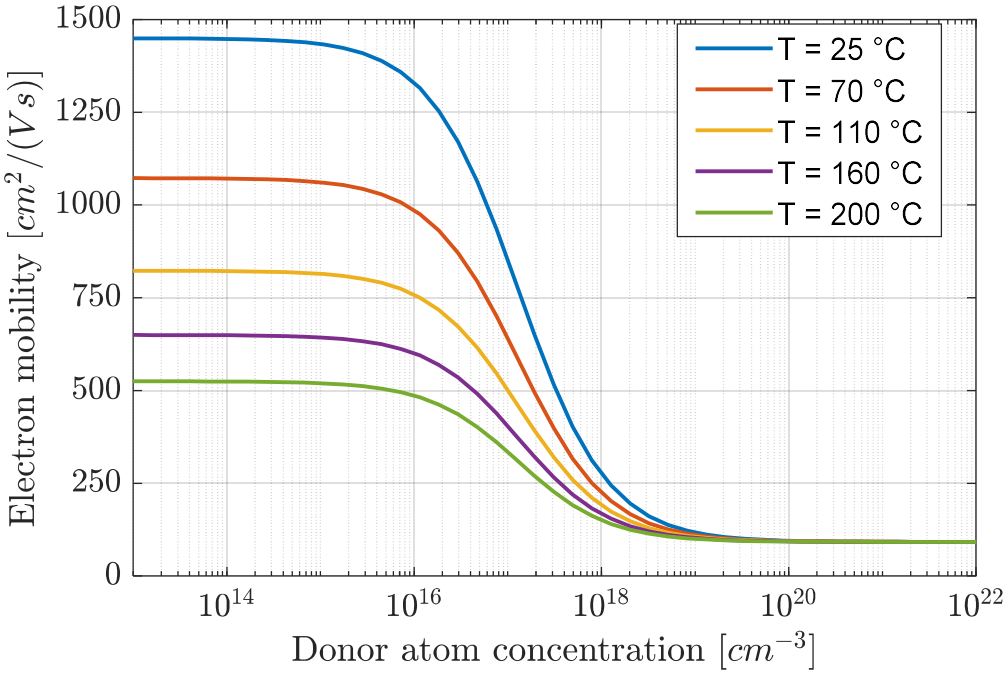

Fig. 35 Electron mobility as a function of dopant concentration

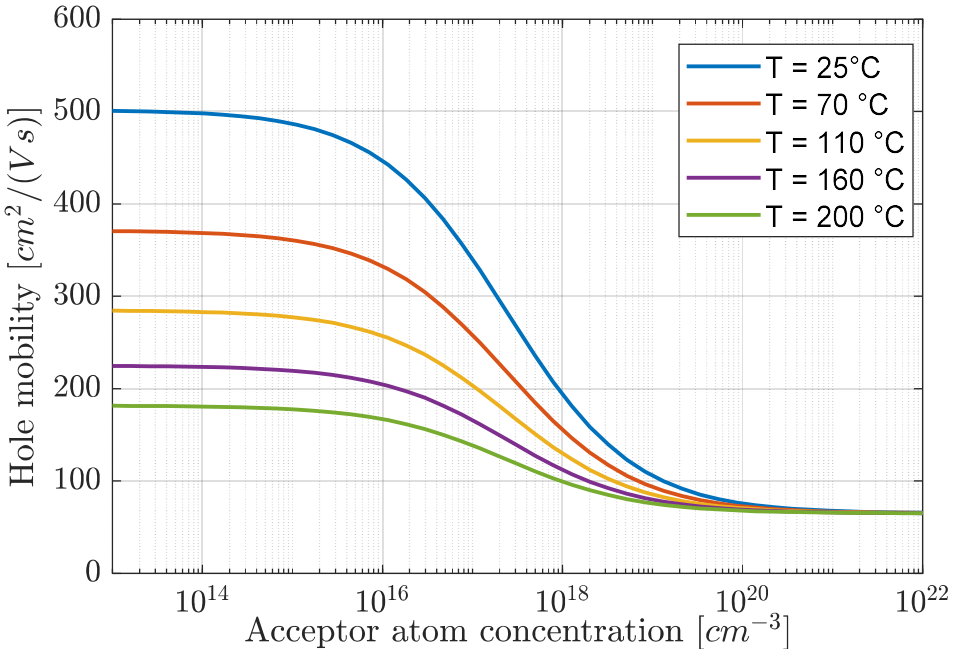

Fig. 36 Hole mobility as a function o dopant concentration

Modelling accurately carrier mobilities is extremely important as the magnetic field effect on the device its proportional to its value (see for instance equation (121) and (122)). Thus, given the same magnetic field intensity, different mobility values determine different impact magnitude.

A very rough estimation can be performed on the magnitude of the magnetic field effect on different semiconductor materials. Computing the arithmetic mean of all the mobility values proposed in [24] for three different materials at room temperature and low dopant concentration one obtains:

Table 5 Carrier mobility values for different materials in $\boldsymbol{cm^2/(Vs)}$

	Silicon	GaAs	Germanium
Electron mobility	1388	8420	3665
Hole mobility	481	383	1839
Mean mobility	934	4401	2752

If one assumes that the current inside the device is 50% due to electrons and 50% due to holes and that the impact of the magnetic field on silicon is equal to 1, then by looking at the mean mobility of GaAs and Germanium one can deduct that the magnetic field impact on GaAs is around 4.7 and 2.9 for Germanium.

This very simplified analysis shows that at least at low temperature and low dopant concentration the magnetic field impact on GaAs-based devices and Germanium-based devices is respectively almost 5 and 3 times stronger than on silicon-based devices.

4.2.1 Case study 1

The numerical parameters of the 1st case simulation can be listed in the following table:

Table 6 Numerical values of parameters adopted in case study 1

Name	Symbol	Value
Device temperature	T	160 $[°C]$
Electron mobility	μ_{0n}	1430 $[\frac{cm}{V \cdot s}]$
Hole mobility	μ_{0p}	495 $[\frac{cm}{V \cdot s}]$
Electron lifetime	τ_{0n}	$1.79 \cdot 10^{-4}$ $[s]$
Hole lifetime	τ_{0p}	$3.36 \cdot 10^{-5}$ $[s]$
p-side length	l_p	80 $[\mu m]$
Intrinsic side length	l_i	150 $[\mu m]$
n-side length	l_n	30 $[\mu m]$
Device width (diamater)	L_y	4 $[cm]$
Max acceptor atom concentration	N_a	10^{19} $[cm^{-2}]$
Max donor atom concentration	N_d^+	10^{21} $[cm^{-2}]$
Intrinsic donor atom concentration	N_d^-	$2 \cdot 10^{13}$ $[cm^{-2}]$

The simulation results are presented as follows. Only the most significant quantities are plotted in this section, (i.e. the I-V on-state characteristics, the power loss increase and the current density increase). The internal variables for one operating condition are shown in the end in order to confirm the occurrence of the same phenomena identified in the previous section.

Thanks to the introduction of more realistic modelling assumptions it is now possible to compare the I-V characteristics with the ones provided by manufacturers in datasheets. However, not a perfect match can be expected, most of all because the thickness of the p, n-minus and n-zones (i.e. l_p, l_i and l_n respectively) are not specified. Thus, thanks to the data provided by POSEICO (see Fig. 32) a value can be chosen for each of those parameters (the chosen values are shown in Table 6) which is reasonably close to the real one, but not exactly the same.

Thanks to the comparison at zero magnetic field with the curve provided by the manufacturer the validity of the model and of the simulation is proven and it forms a solid starting point, from which the magnetic field analysis can be carried out.

Fig. 37 shows the comparison between the I-V curve obtained through simulations (blue line) and the curve provided by ABB in [33]. As anticipated above, the match is not perfect but in simple terms, it is good enough to validate the model and the simulations.

Fig. 38 shows the increase in the conduction power loss due to the action of the magnetic field in all of the on-state area. These losses are totally negligible even in the case of much higher magnetic field intensity.

Fig. 39 shows the current density local increase as a function of the magnetic field intensity and the applied voltage. It appears to be a small effect at $B = 100\ mT$, but it is not as negligible as the power loss increases, as a matter of fact, it reaches already a 10% increase for $B = 500\ mT$.

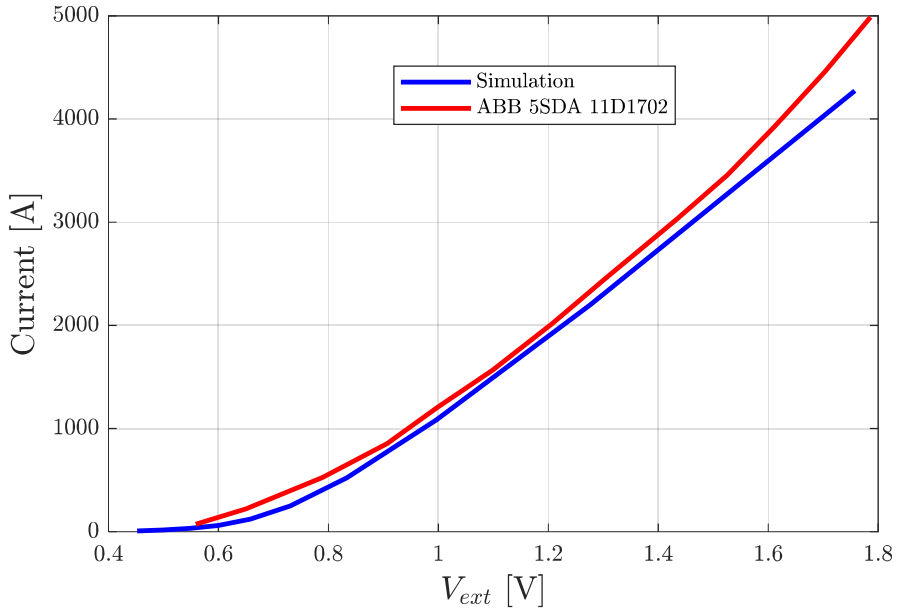

Fig. 37 on-state I-V characteristic comparison at B = 0 T with an ABB diode

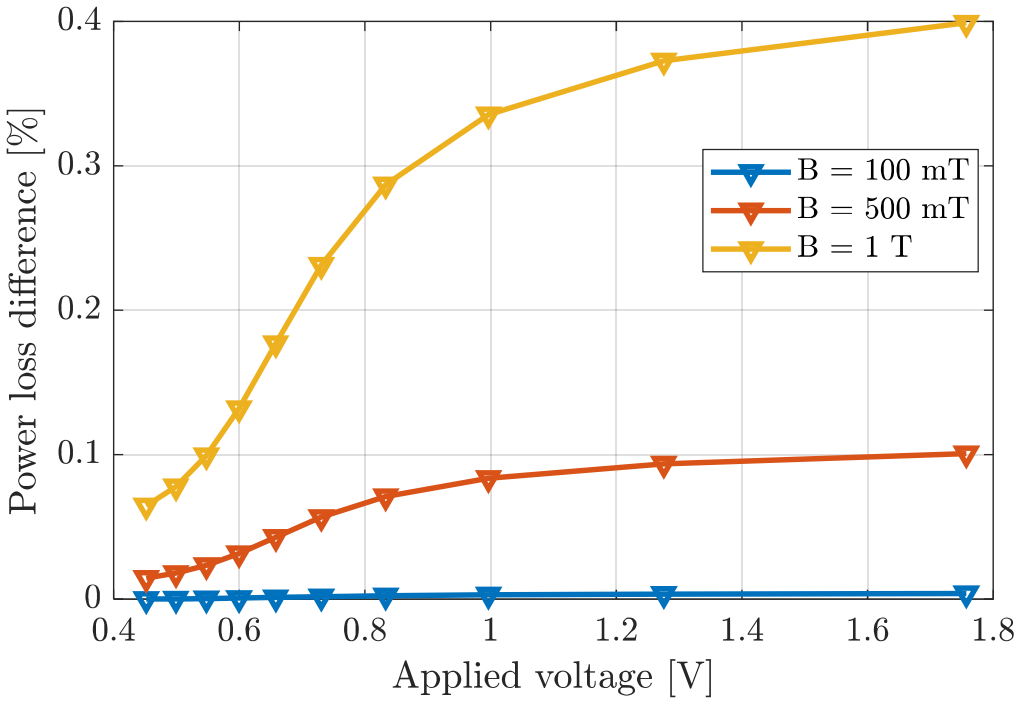

Fig. 38 Conduction power loss increase

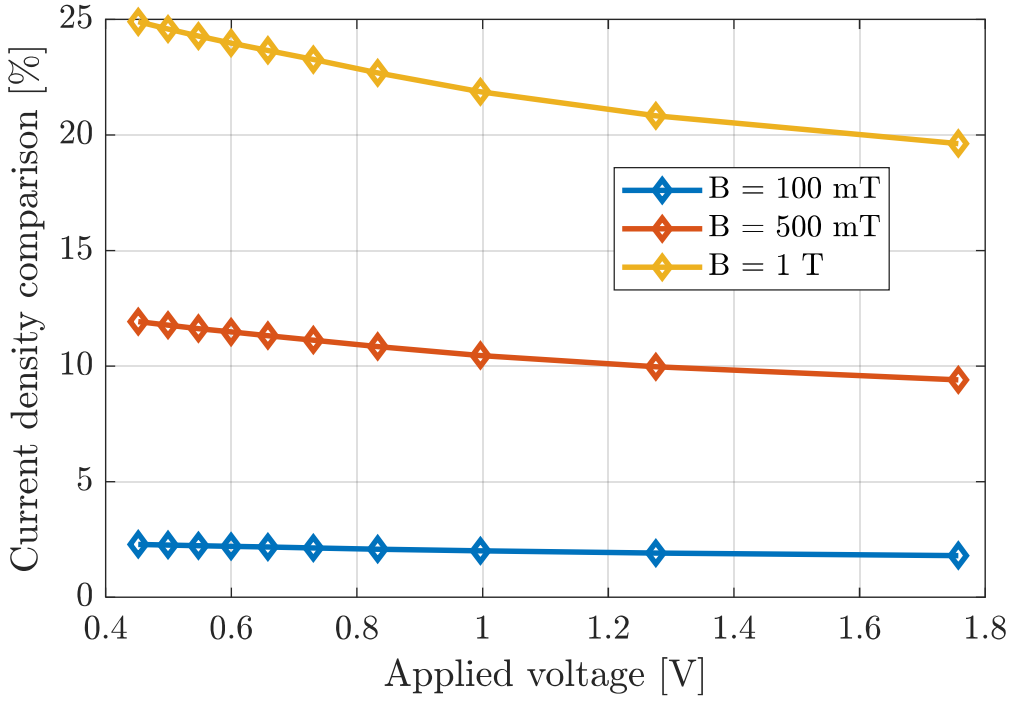

Fig. 39 Current density local increase

Even if their entity is totally negligible one can notice from Fig. 38 that power losses tend to increase for higher voltage, this fact has been attributed to the relative increase of electron carriers compared to holes in forming the total current density.

This phenomenon has not occurred in the PN-junction section because the length of the device was chosen such that the carriers could have recombined totally (or almost) within the device itself, giving birth to the following current profiles in every operating condition.

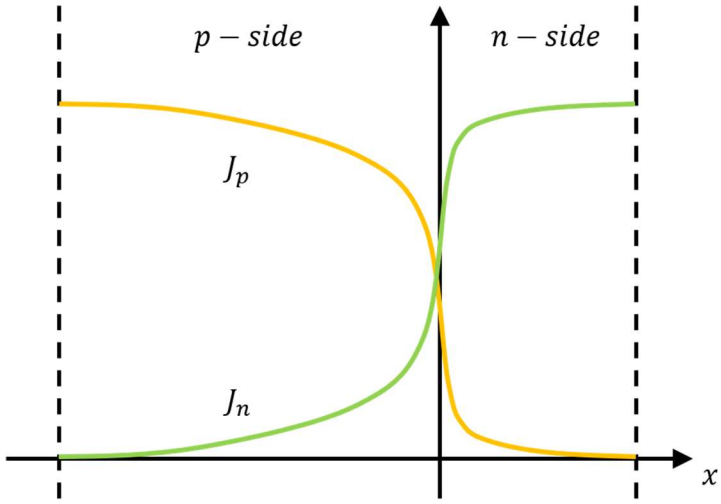

Fig. 40 Hole and electron current density profile in a long base diode

However, the length of the device chosen for these simulations (in compliance with the real data provided by POSEICO), is such that when higher voltages are applied all the carriers cannot recombine completely across the device (see Fig. 41 for instance).

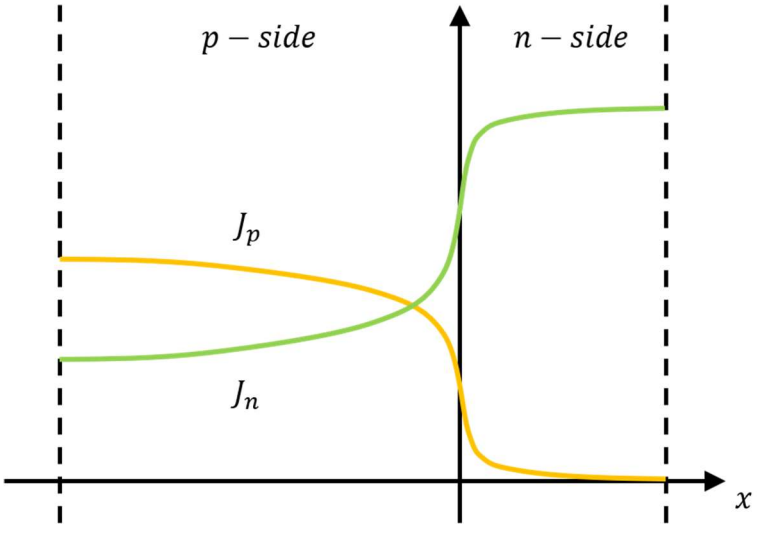

Fig. 41 Hole and electron current density profile in a short base diode

Therefore, the device behaves as a short base diode for higher applied voltage, leading to a "dominance" of a single type of carrier, electrons in this case, causing a higher sensitivity to the ESMF.

4.2.2 Case study 2

The same values shown in Table 6 are chosen except for the definition of the Hall mobility where the nominal carrier mobility at room temperature is considered, i.e. μ_{0n} and μ_{0p}. This choice enhances the effect of the magnetic field on the device, that is the reason why this simulation is considered conservative.

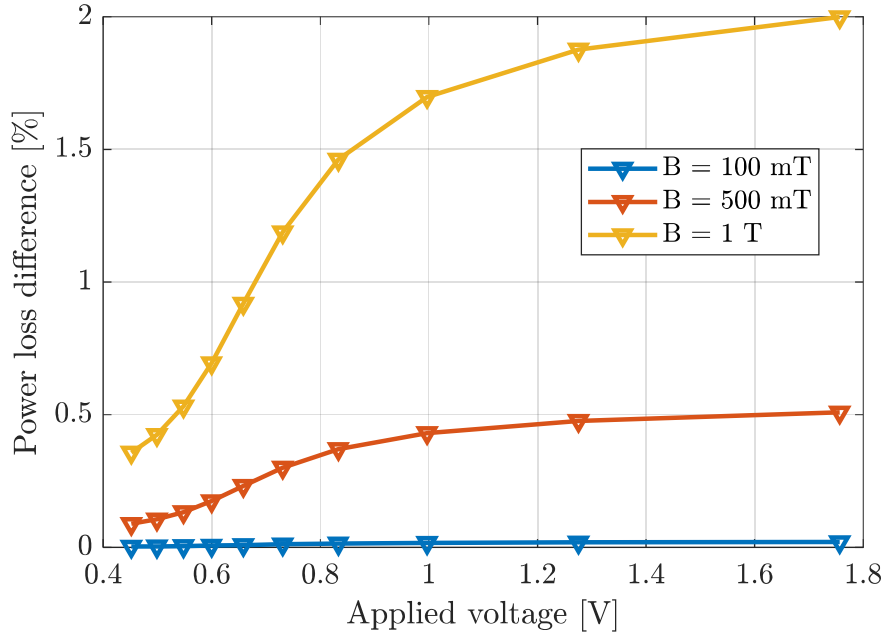

Fig. 42 Conduction power loss increase

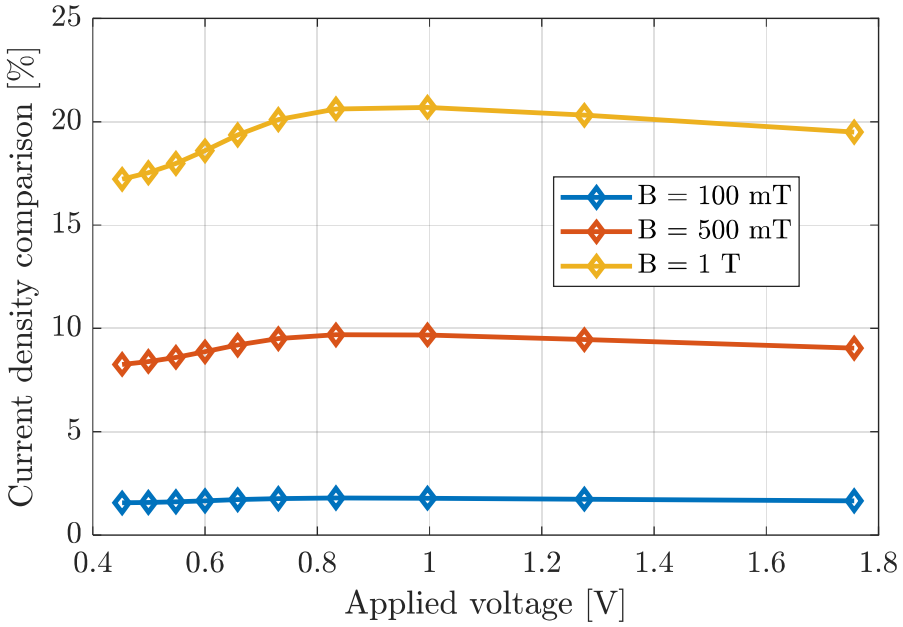

Fig. 43 Current density local increase

4.2.3 Case study 3

Table 7 Numerical parameters adopted in case study 3

Name	Symbol	Value
Device temperature	T	190 $[°C]$
Electron mobility	μ_{0n}	1430 $[\frac{cm}{V \cdot s}]$
Hole mobility	μ_{0p}	495 $[\frac{cm}{V \cdot s}]$
Electron lifetime	τ_{0n}	$1.79 \cdot 10^{-4}$ $[s]$
Hole lifetime	τ_{0p}	$3.36 \cdot 10^{-5}$ $[s]$
p-side length	l_p	80 $[\mu m]$
Intrinsic side length	l_i	100 $[\mu m]$
n-side length	l_n	30 $[\mu m]$
Device width (diameter)	L_y	11 $[cm]$
Max acceptor atom concentration	N_a	10^{19} $[cm^{-2}]$
Max donor atom concentration	N_d^+	10^{21} $[cm^{-2}]$
Intrinsic donor atom concentration	N_d^-	$2 \cdot 10^{13}$ $[cm^{-2}]$

A “bigger” device in terms of dimensions and power rating is simulated here, i.e. a rectifier diode available in POSEICO’s datasheet is considered (diode model AR709 [34]).

The same quantities are shown in the previous sections are plotted down below for comparison. The validation of the model is proposed in Fig. 44 where the simulated I-V curve is compared with the one shown in the datasheet.

What can be deducted from Fig. 45 is a lower power loss increase compare to Fig. 38, however this is most likely due to the higher temperature at which the diode from POSEICO operates (190 °C), which determines a further drop in the carrier mobilities, resulting in a less significant magnetic field effect.

The same comment can be made regarding the current density increase in Fig. 46.

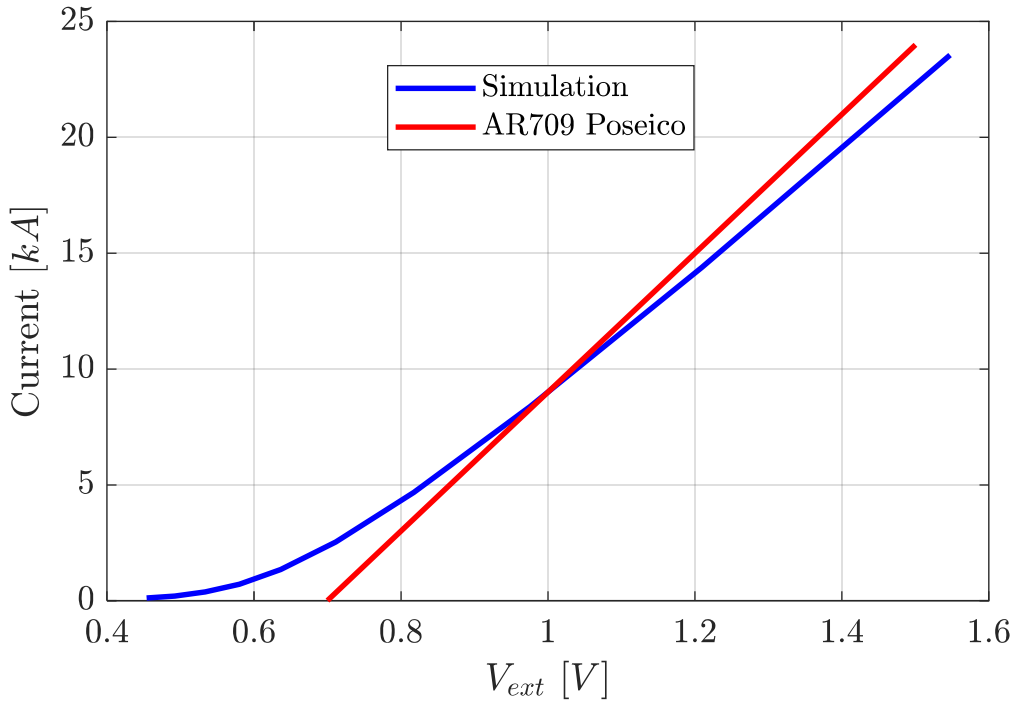

Fig. 44 I-V characteristics comparison

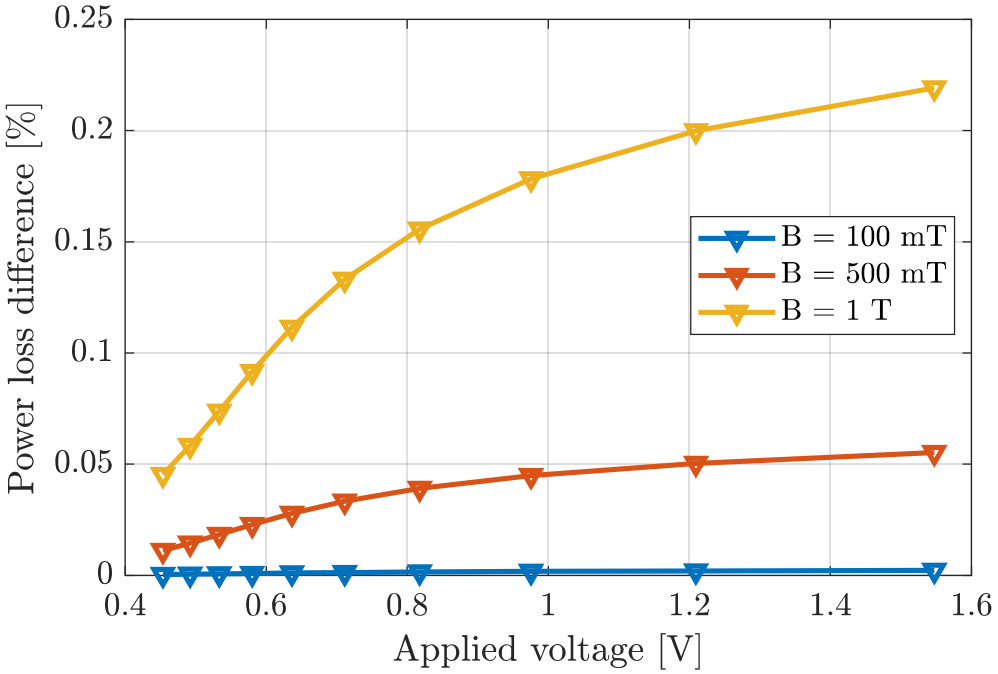

Fig. 45 Conduction power loss increase

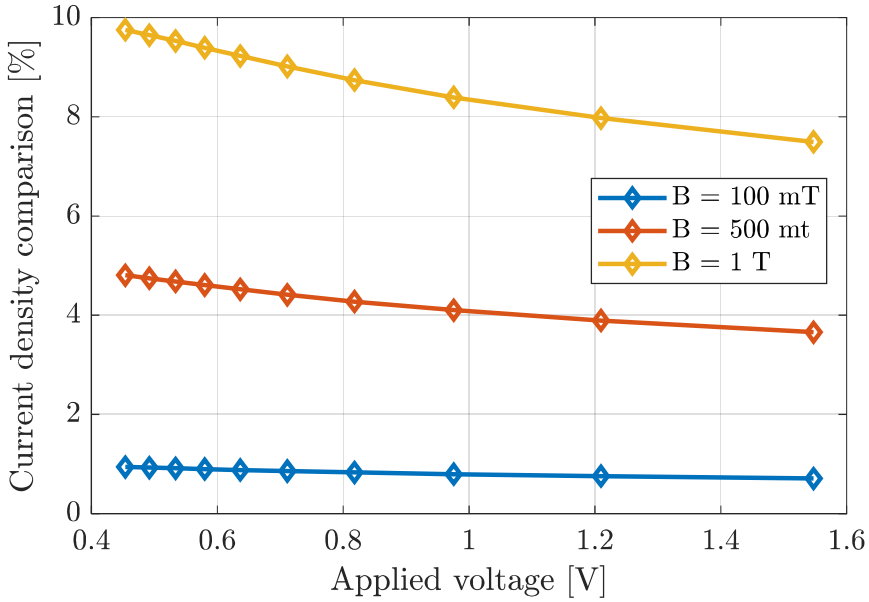

Fig. 46 Current density local increase

4.2.4 Case study 4

This final set of simulations replicates the same simulations presented in the previous study case with conservative parameters.

Therefore, the same values listed in Table 7 are adopted, except for the definition of the Hall mobility, where the nominal carrier mobility at room temperature is considered, i.e. μ_{0n} and μ_{0p}

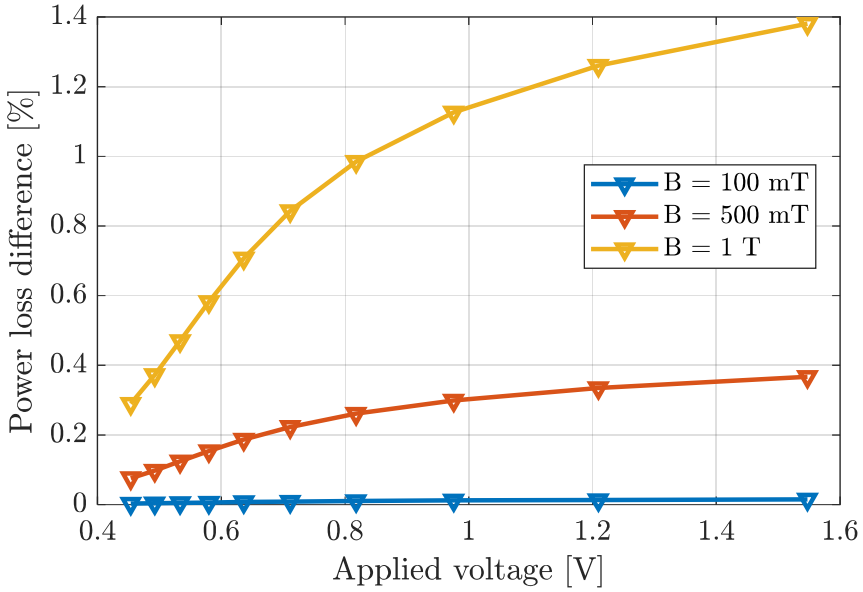

Fig. 47 Conduction power loss increase

Higher power losses and a higher non-uniformity in the current density is obtained, however, as regards power losses, they result totally negligible even at 1 T, while a more careful approach has to be taken as far as the current density is concerned.

Indeed, it still is negligible at 100 mT and with conservative parameters, however the margin does not look as high as the one of power loss.

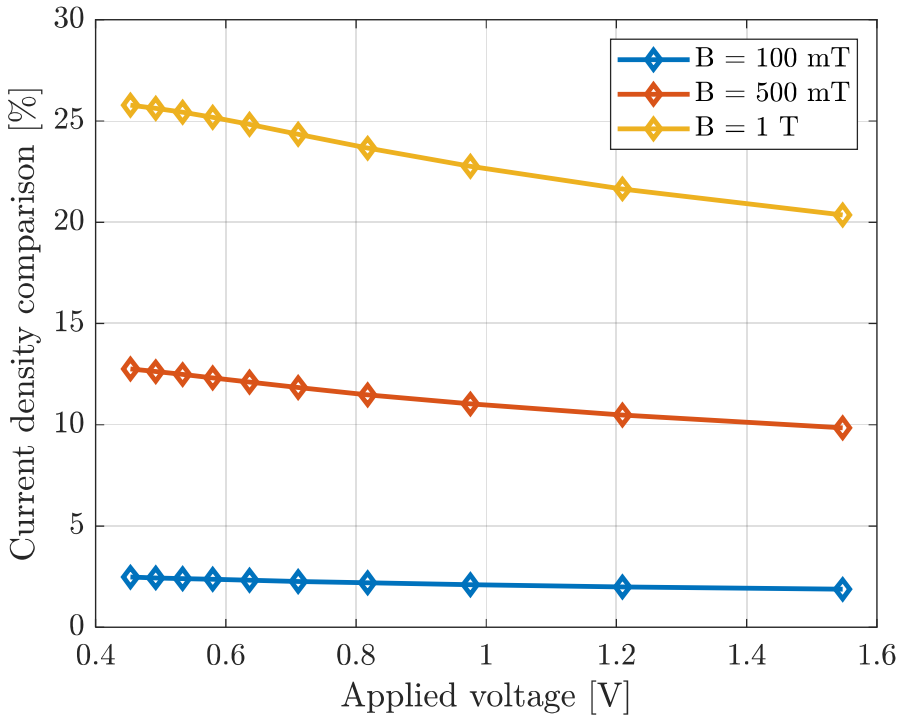

Fig. 48 Current density increase

4.2.5 Internal variables

The internal variables in one operating conditions of case study 2 are shown in this section as an example.

Please note that in order to carry out simulation of a real dimension power diode a slight modification to the code had to be implemented. As a matter of fact, a larger section of the device (i.e. a longer y-side in this case) would require a higher number of mesh point in order to be able to compute correctly the boundary effect determined by the ESMF. Indeed, these effects take place in a “thin” area close to the insulating boundary.

Therefore, in order to avoid an excessive number of mesh points, the mesh had to be made non uniform also along the y direction, with a higher density of points close to the insulating boundary.

Again, in order to show plots where the effect of the ESMF is "graphically appreciable" the extreme case $B = 1\,T$ and the operating condition at $V_{appplied} = 0.56\,V$ are selected The electric potential is shown in Fig. 49

The Hall effect is not particularly strong here, however, the magnetoconcentration is quite significant as it is shown in the zoomed areas of Fig. 50 and Fig. 52.

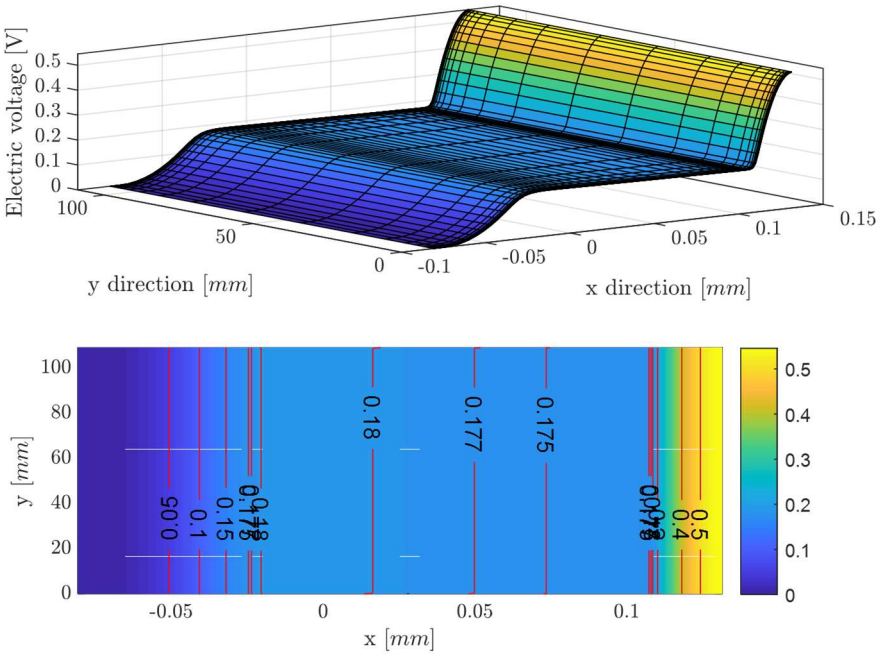

Fig. 49 Electric potential distribution

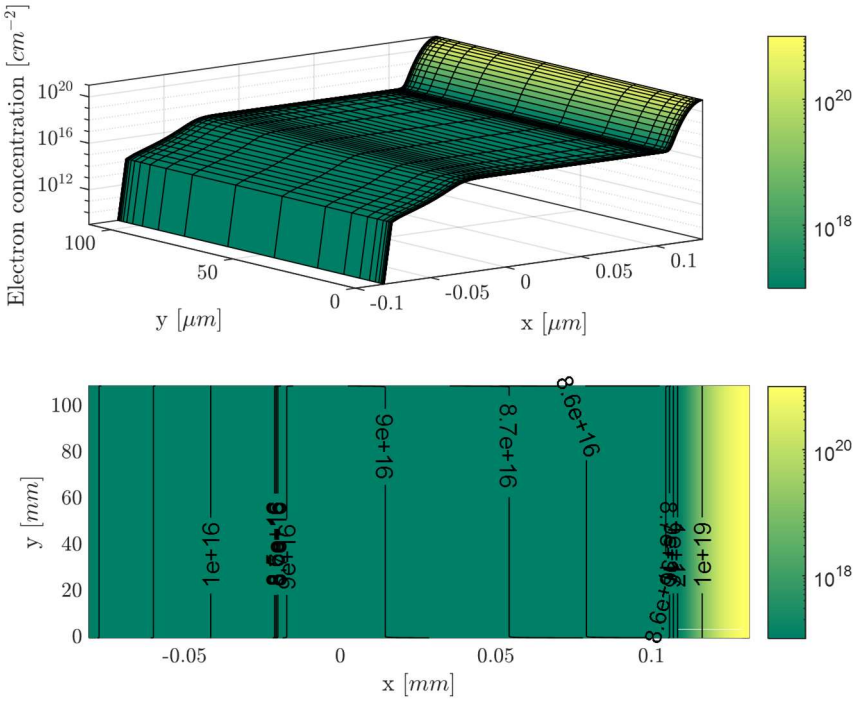

Fig. 50 Electron concentration distribution

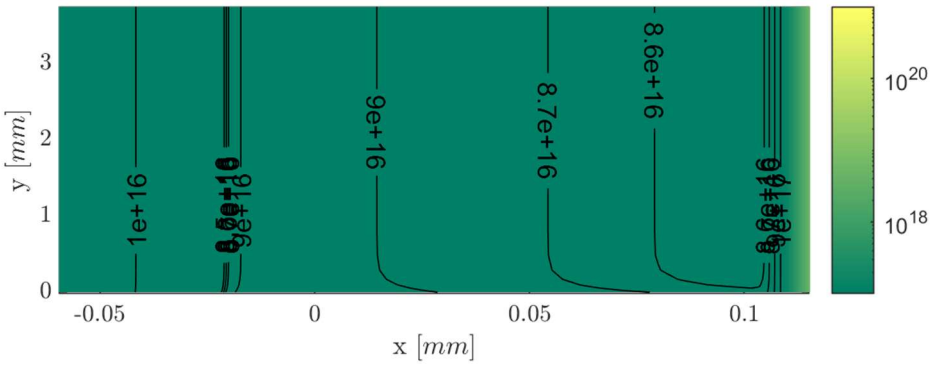

Fig. 51 Zoom of the electron concentration distribution at the lower boundary

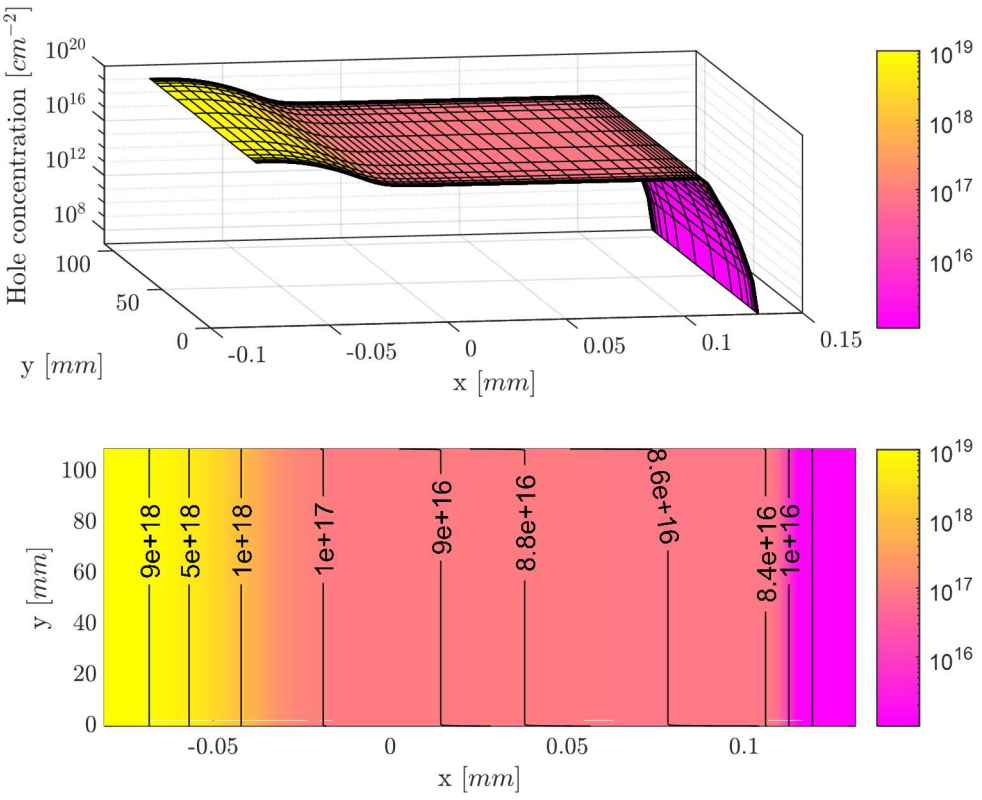

Fig. 52 Hole concentration distribution

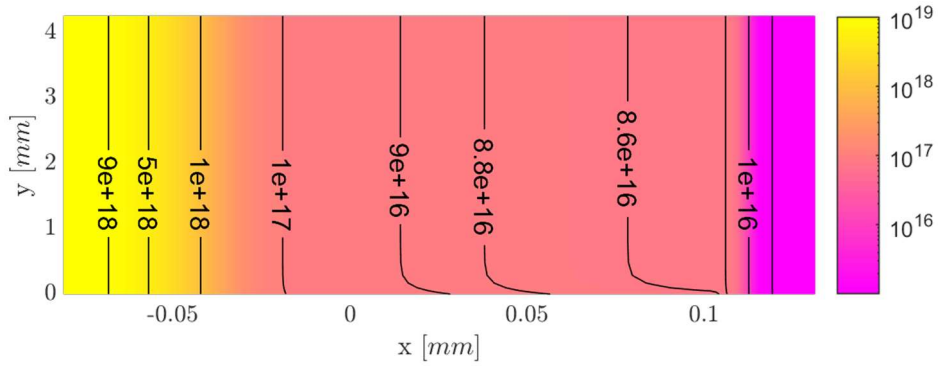

Fig. 53 Zoom of the hole concentration distribution at the lower boundary

The carrier concentrations are shown, it is easy to observe from Fig. 51 and Fig. 53 that charges are pushed towards the lower horizontal side of the device in order to balance Lorentz's force.

Finally, the current density distribution is shown in Fig. 54.

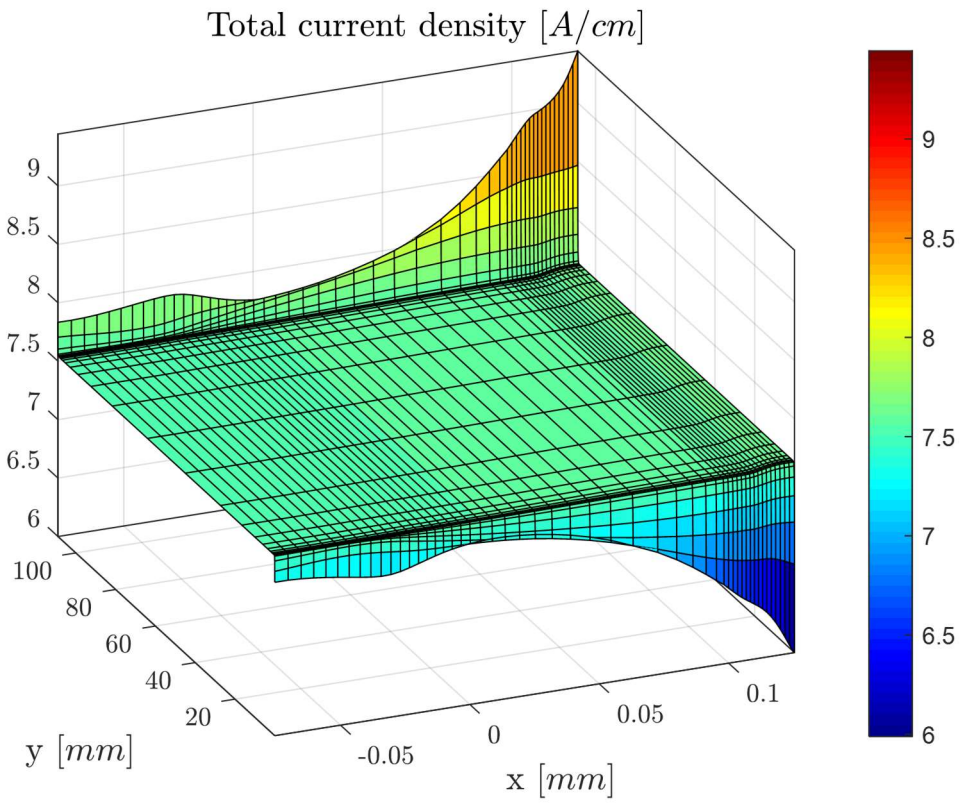

Fig. 54 Current density distribution

4.3 PIN junction simulations in reverse bias (blocking state)

The blocking state simulation aims at investigating if the magnetic field has an impact on the internal electric field, causing local high critical values potentially damaging the device. If that was the case, it would be necessary to de-rate the maximum voltage applicable to the device. These simulations do not require to obtain the I-V characteristics and computing power loss and current density, on the contrary, it is necessary to compare the electric field distribution in the worst case scenario (B = 1 T) with the electric field distribution at zero magnetic field when the max voltage is applied. The diode under consideration is the one from ABB simulated in study case 1 and 2.

The electric field distribution in the two cases is shown in Fig. 55 and Fig. 56, while their difference is shown in Fig. 57. It is possible to appreciate from Fig. 57 that a change in the electric field distribution arises due to the magnetic field (more precisely, this is attributed to the magnetoconcentration phenomenon determined in turn by the magnetic field). However, even if this rise is quite relevant (around 4 kV/cm) it takes place in a non-critical area. i.e. where the electric field is well below its maximum value.

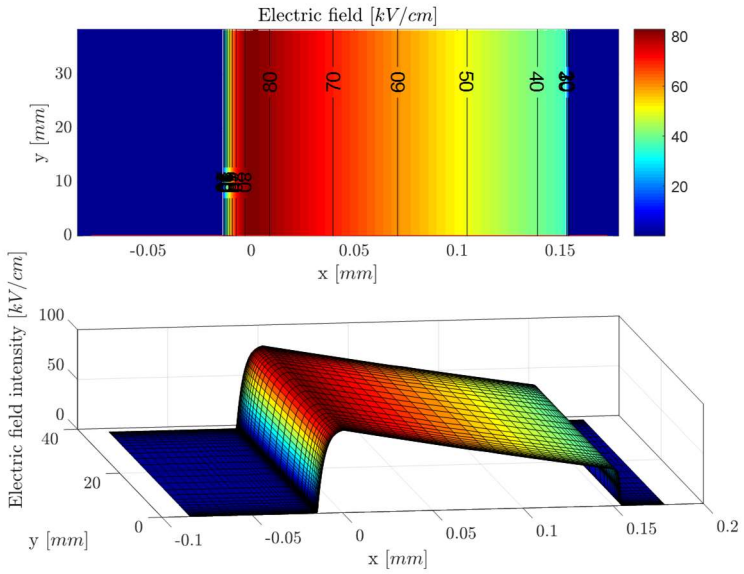

Fig. 55 Blocking electric field at $\boldsymbol{V = 1\ kV}$ *and* $\boldsymbol{B = 0\ T}$

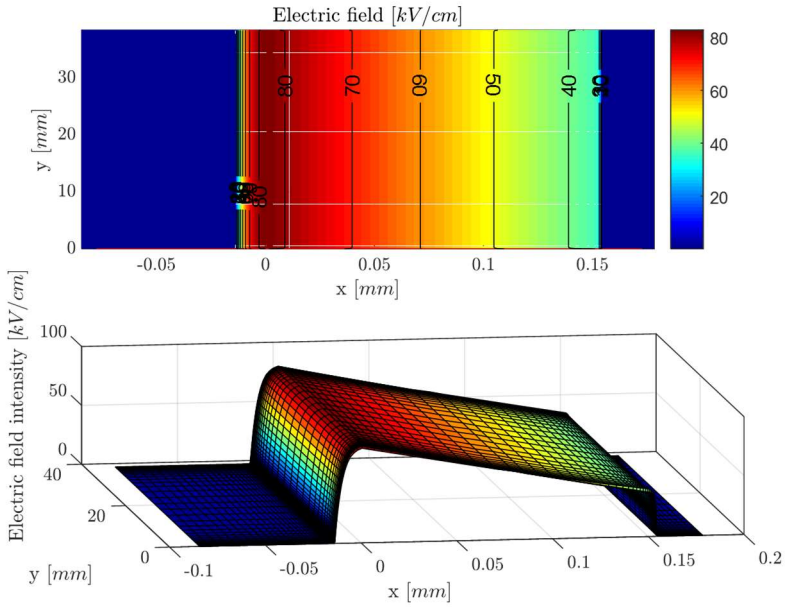

Fig. 56 Blocking electric field at $\boldsymbol{V = 1\ kV}$ *and* $\boldsymbol{B = 1\ T}$

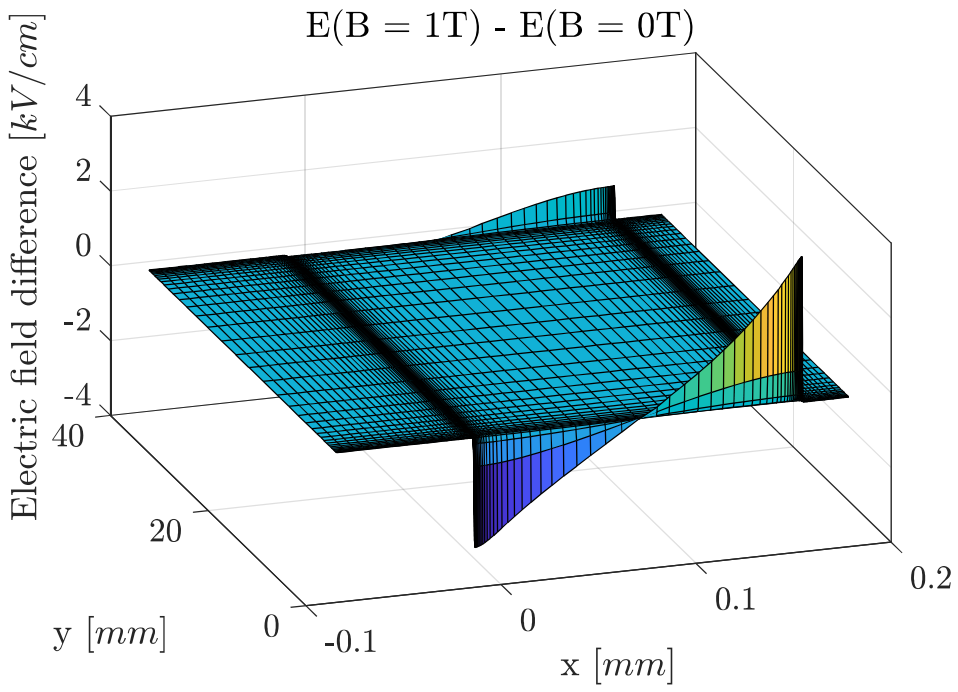

Fig. 57 Electric field difference

4.4 Conclusions

The model adopted in the simulation, and the development of the code dedicate to solve its equations is described in this report.

The simplifying assumptions on which the simulations are based are presented and extensively discussed.

The simulation analysis is divided in two main parts, the first one rotates arounds a simplified PN junction and aims at showing and describing the main effect of a static magnetic field on semiconductor technology. The second rotates around the study of power PIN junctions and it aims at providing more accurate and quantitative results.

On balance, thanks to the theoretical analysis and the simulation results, the following concluding remark can be made:

- A static magnetic field has an effect on conduction power losses of semiconductor devices, however, the order of magnitude of this effect is negligible and the safety margin is significant.
- A static magnetic field has an effect on the current distribution of semiconductor devices, causing carrier crowding at the edges of the device (the location of such crowding depends on the angle between the magnetic

field and the current direction). Such effect is negligible in steady state but the safety margin is not very significant.

- A static magnetic field alters the electric field distribution inside the device potentially affecting its blocking voltage capability. Since this phenomenon strongly depends on the geometry of the device, it is difficult to generalize the conclusions. However, at least in power diodes, it does not seem to represent a critical effect.
- A static magnetic field effect on the device switching remains unknown. Dynamic operating conditions have not been investigated as the complexity of the code would have been excessive. As a matter of fact, a 3D study should be performed in this case because geometrical effects play a fundamental role in this situations. For the very same reason, a simplified geometry would have been inappropriate for such study, making necessary a realistic representation of the device structure, hence complicating even more the code.
- Many characteristics parameters have been found to influence the impact of the magnetic field on the device, above all dopant concentration and operating temperature. Their effect is thoroughly described in this report.

Analysis of the effect of a static magnetic field on centrifugal pumps and on their shafts

5 Purpose

The purpose of this document is to describe the analysis that was carried out concerning the effect of a static magnetic field on rotating electrically conductive objects, more particularly, pump impellers and shafts.

The study was developed through different stages, starting from a simplified approach and converging towards more and more complex and realistic situations. The software tool adopted throughout the research was ANSYS Maxwell.

The chapter is structured as follows:

- Chapter 7 deals with an introductory study of the effect of the SMF on rotating disks. The aim of this section is to describe the simplest approach to this study and to obtain and investigate results which are useful for a clearer understanding of the findings presented in the successive sections.
- Chapter 8 deals with an analysis regarding how a pump impeller can be modelled such that the simulations can provide conservative results and be executed in a shorter time.
- Chapter 9 presents the result regarding the analysis of real impellers, also including the associated shaft. Two pump impellers are considered, a low power and a high power one in order to investigate the different relative impact the magnetic field on the two.

Electric motors can be set in a direct or indirect drive configuration, depending on the application. This study takes into account only the direct drive configuration as shown in Fig. 58

While the effect of the SMF on electric motor is analysed already in previous studies at ITER, no results are currently available as regards the two other main rotating component of the entire system, i.e. the connecting shaft and the pump impellers.

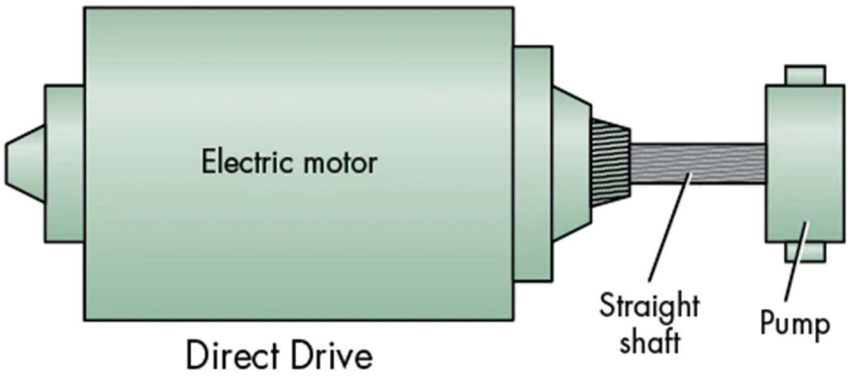

Fig. 58 Direct drive configuration

The impellers studied here are of the centrifugal type, intended to operate in water cooling applications.

6 Analysis of conductive disks rotating in a uniform static magnetic field

The elementary geometry which resembles the most to a pump impeller is a disk, therefore, the study of such objects was chosen to be first step to approach the problem.

The main problem associated with spinning conductive objects inside a magnetic field is the insurgence of parasitic forces which oppose to the motion and caused by induced Eddy's currents flowing inside the component.

Such scenario is conceptually equivalent to a magnetic brake, thus, the key parameter that is investigated throughout the study is the magnetic braking torque.

The first set of simulations aims at investigating the braking torque on a rotating disk and at evaluating the impact of the main geometric parameters on the braking torque itself.

In particular, Fig. 59 shows the parameters involved in the analysis: ω is the rotational speed, R is the disk radius, t is the disk thickness whereas α is the angle between the magnetic field lines and the axis around which the disk revolves.

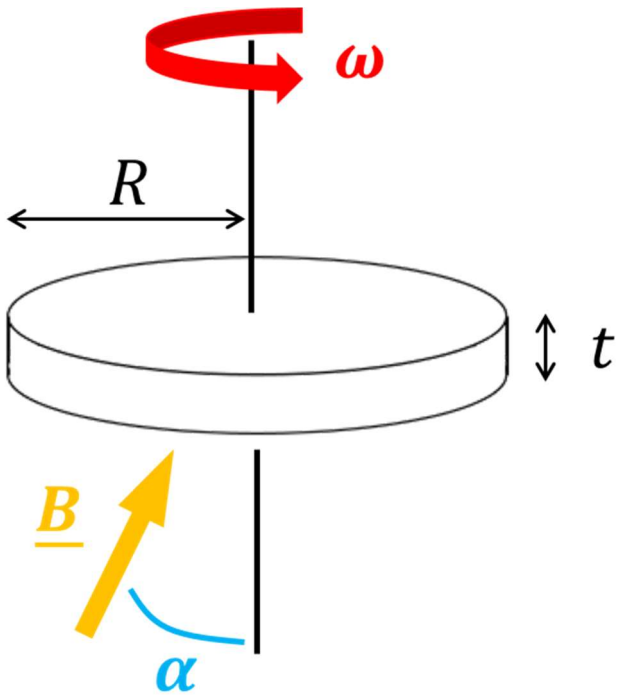

Fig. 59 Conductive disk rotating in a uniform SMF

6.1 The impact of orientation

The goal of the first simulation is to identify the α angle which maximizes the braking torque, such that all the subsequent simulation can be performed in the worst case scenario and therefore provide conservative results.

Thus, the braking torque on a copper disk rotating at 1500 rpm was calculated for different values of α and the results are shown in Fig 60.

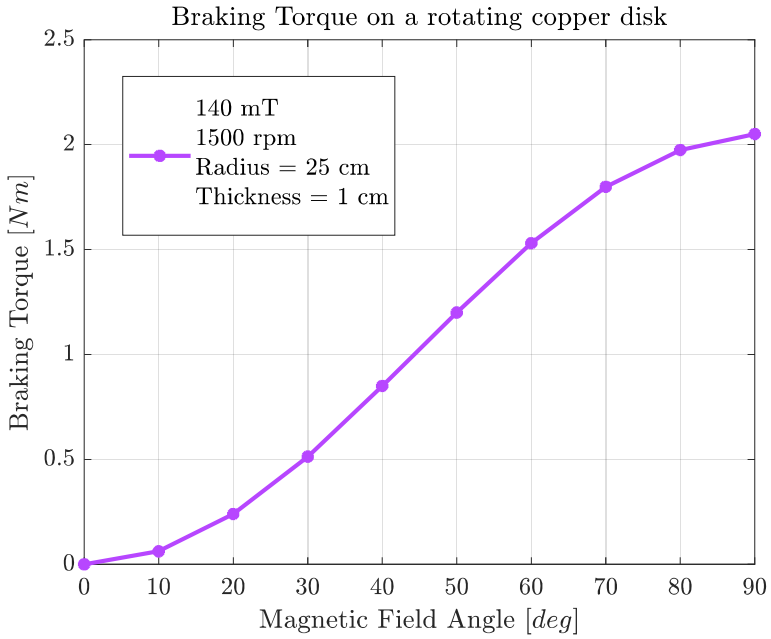

Fig. 60 Magnetic braking torque dependence on the angle between the magnetic field lines and the rotation axis

From the plot it is easy to observe the torque is maximized when the magnetic field is perpendicular to the rotation axis, while it is minimized if they are parallel, in particular for a perfect circular disk, the braking torque is exactly zero. Indeed it easy to prove that for in circular disk whose rotation axis is parallel to the flux lines of a uniform SMF a radial electric field able to cancel out in steady state the radial Lorentz force builds up.

Due to Lorentz's force, electrons which are moving at a distance r from the center with tangential velocity $v = r\omega$ (due to rotation of the disk) experience a radial force $\underline{F}_{Lorentz} = q\underline{v} \times \underline{B}$, which in this particular case becomes:

$$F_{Lorentz} = er\omega B \tag{259}$$

where B is the field and e the electrons charge.

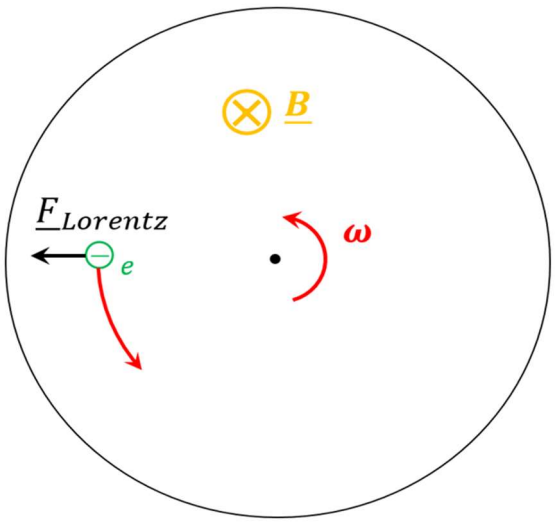

Fig. 61 Top view of conductive rotating disk with axes parallel to the magnetic field

This leads to electrons moving towards the periphery which creates a radial charge distribution, therefore a radial electric field $E(r) = dV/dr$ and a radial voltage $V(r)$. The fact that $\mathrm{E}(r) = dV/dr$ is due to the symmetry of the problem: all other components of the gradient vanish as the field only variates in the radial component.

In the steady state the electric ($F_E = eE = e\frac{dV}{dr}$) and Lorentz forces cancel out as nothing should move at equilibrium. Thus:

$$er\omega B = e\frac{dV}{dr} \tag{260}$$

and this gives the equation for the voltage which when integrated leads to:

$$V(r) = \frac{B\omega r^2}{2} \tag{261}$$

with respect to the center of the disk where $V = 0$. Between the edge of the disk the absolute value of the voltage difference is:

$$V(R) = \frac{B\omega R^2}{2} \tag{262}$$

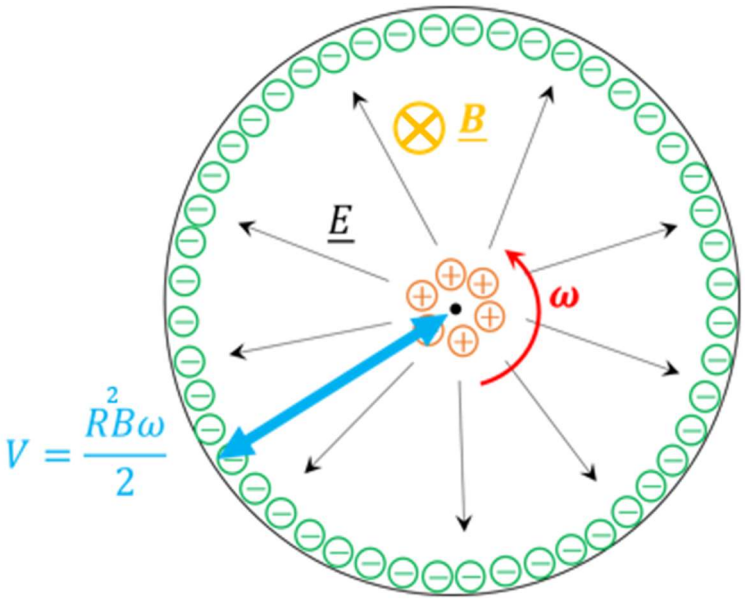

Fig. 62 Charge separation in steady state

(For instance, a disk with a radius of 30cm rotating at 3000 rpm permeated by a 100mT induction field determines a voltage difference from its centre to the periphery equal to 1.4 V).

Therefore, this implies that there is no current circulation in steady state, hence, no braking torque arises.

On the contrary, the braking torque is maximized when $\alpha = 0$. The current path in this case is intuitively less simple to understand, it is shown for a particular case in Fig. 63.

In order to explain the current path shown in Fig. 63 the Lorentz's force approach has to be used, indeed when the magnetic field is static and objects are moving within it, the electromagnetic induction is only due to the motional contribution, as the magnetic field is not time-varying, which in turn is caused by Lorentz's force [35, 36].

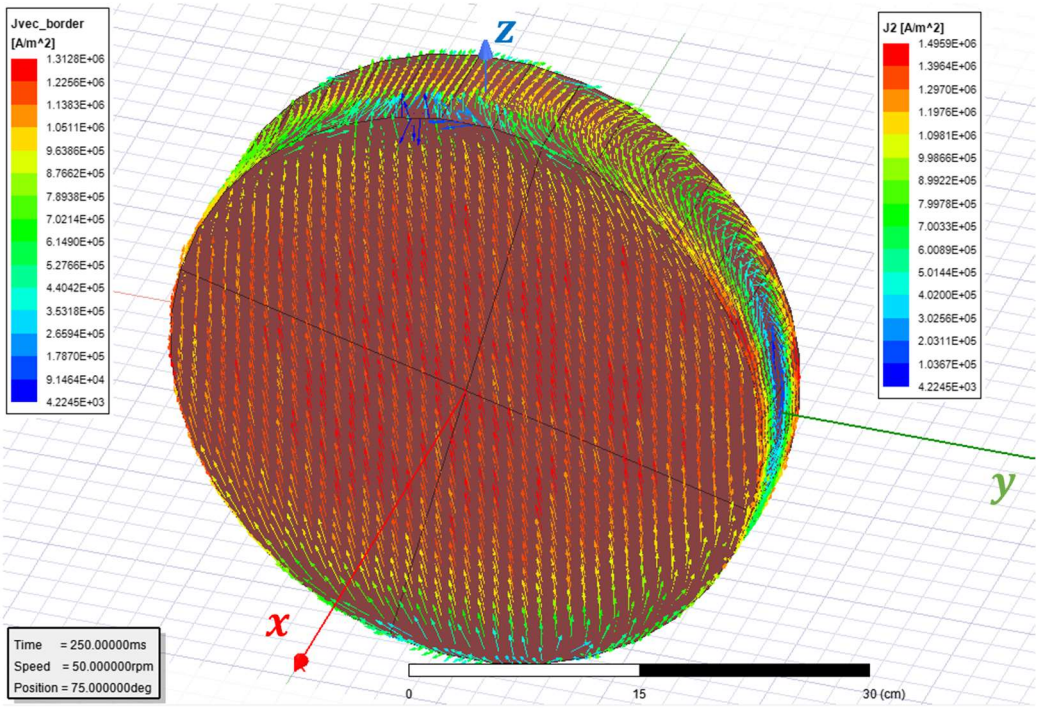

Fig. 63 Current flowing in a copper disk rotating at low speed (50 rpm) with a magnetic field (along Z) perpendicular to the rotation axis (along X)

Applying Lorentz's force on a disk rotating at low speed, one easily obtains the situation described in Fig. 64 and Fig. 65. In particular, by looking at Fig. 65, one can easily observe that electrons are "pushed" along –Z on the light blue half portion of the disk, while the are pushed along +Z on the other half portion. Besides, the force at a fixed radius reaches it maximum value along the Y-axis and it becomes zero along the X-axis due to the angle between the magnetic field and the electron tangential speed.

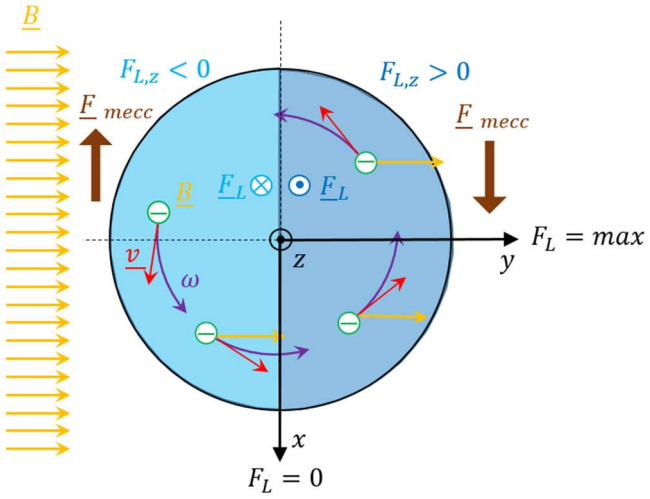

Fig. 64 Disk view on the plane XY

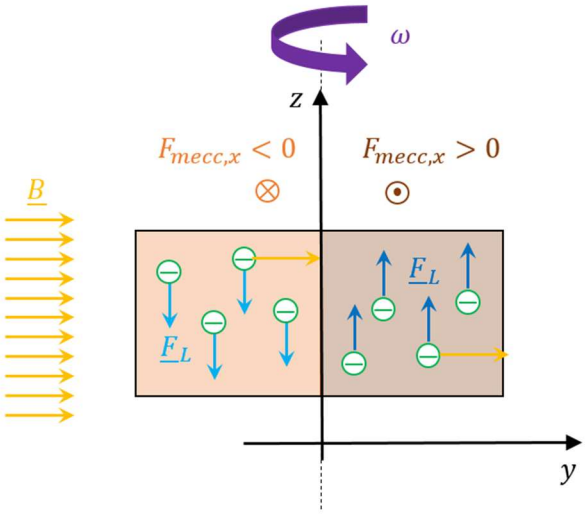

Fig. 65 Disk view on the plane ZY

Furthermore, helped by the ZY-plane view, and thanks to the formula:

$$\underline{F}_{mecc} = i\underline{L} \times \underline{B} \tag{263}$$

It is immediate to observe that the half portion of the disk on the negative Y-axis is affected by a mechanic force directed along -X while the opposite occurs on the other half portion. Thus, a torque which opposes to the rotational movement of the disk arises. Let us now complete the description of the current paths. It has been established that charges move in disk along the Z axis due to Lorentz's force, however, due to the interface condition (zero normal component of the electric field on the disk faces) the electric field becomes tangential and drives the charges along the Y direction. On balance, at low speed, the current path inside the disk is the one shown in Fig. 66:

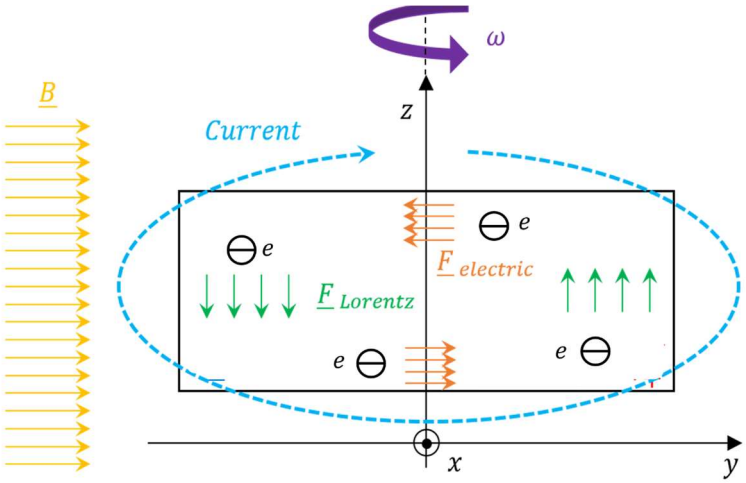

Fig. 66 ZY-plane view

When the rotational speed increases, the current path changes as it can be appreciated from Fig. 67:

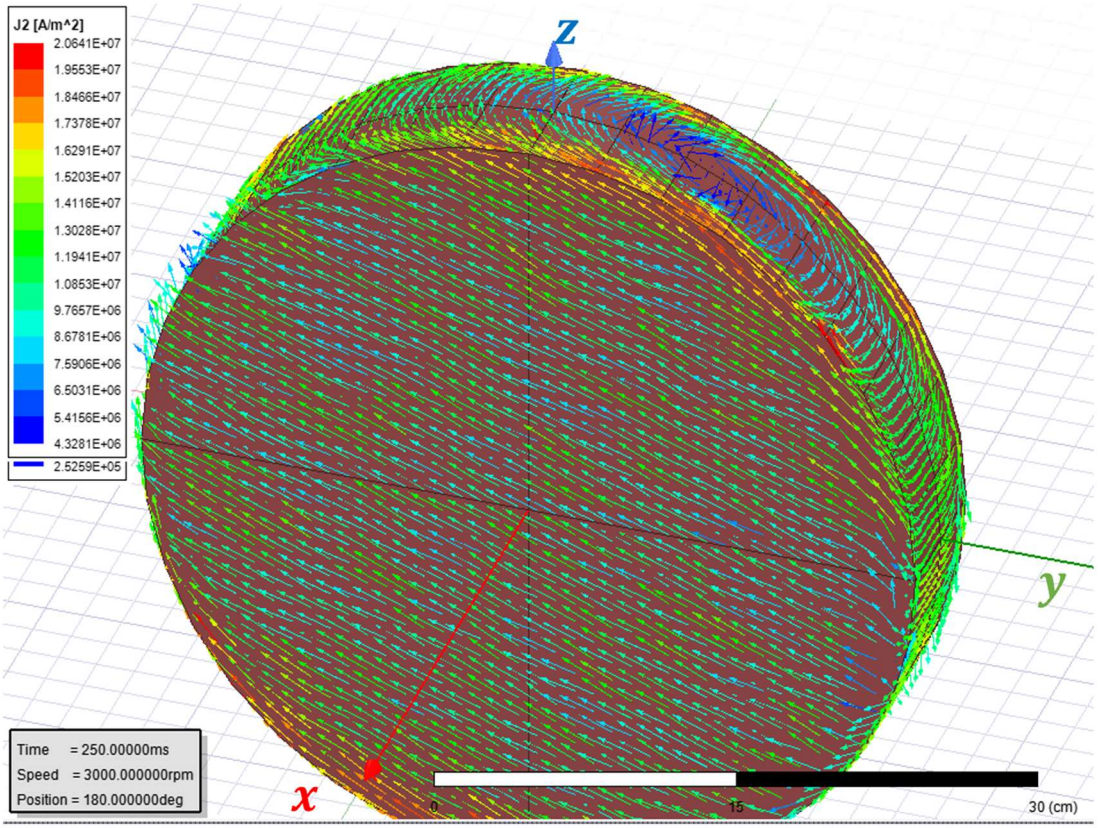

Fig. 67 Current flowing in a copper disk rotating at high speed (3000 rpm) with a magnetic field (along Z) perpendicular to the rotation axis (along X)

The explanation of this behaviour can be given referring to classical concepts of electrodynamics where any current distribution in an external magnetic flux is subject to a force driving the momentum of the distribution to the position where it is aligned with the induction field [37].

As previously described, Lorentz's force determines an electric field whose flux lines lie on the XZ plane (i.e. an electric field with no y-components). It is commonly known that any distribution of current inside a magnetic field is subject to a torque/force which tends to drive the distribution to the lowest potential energy position, i.e. in a position where the magnetic momentum of distribution is aligned with the external magnetic field [37]. In addition, such force/torque increases with the current intensity.

Therefore, with a higher speed, thus, with a higher induction effect, therefore with a higher current, the torque above mentioned becomes higher driving the current distribution to a position where its magnetic momentum is more and more aligned with the external magnetic field.

This situation is depicted in Fig. 68 and Fig. 69 (please notice that the arrows in the current paths indicates the movement of the electrons, therefore the real current direction is the opposite of the one depicted).

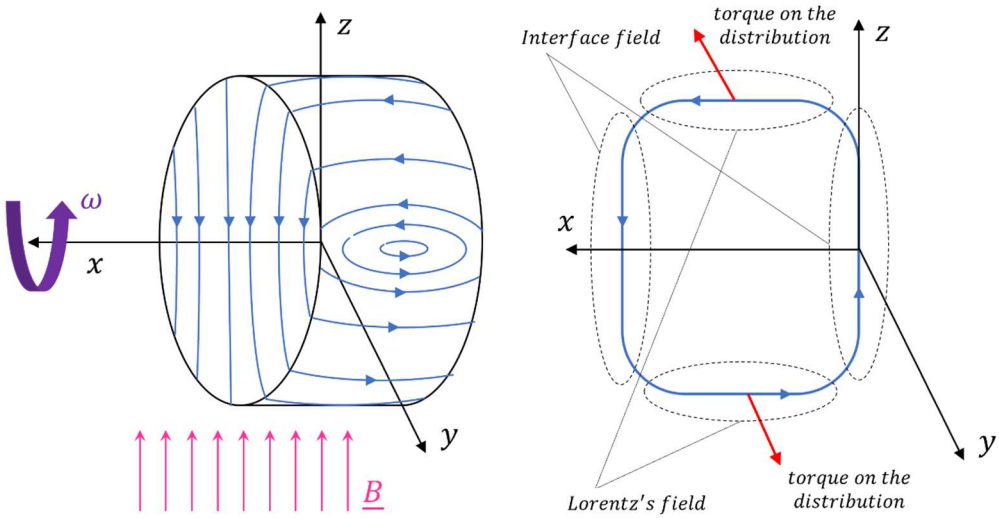

Fig. 68 Low speed current path

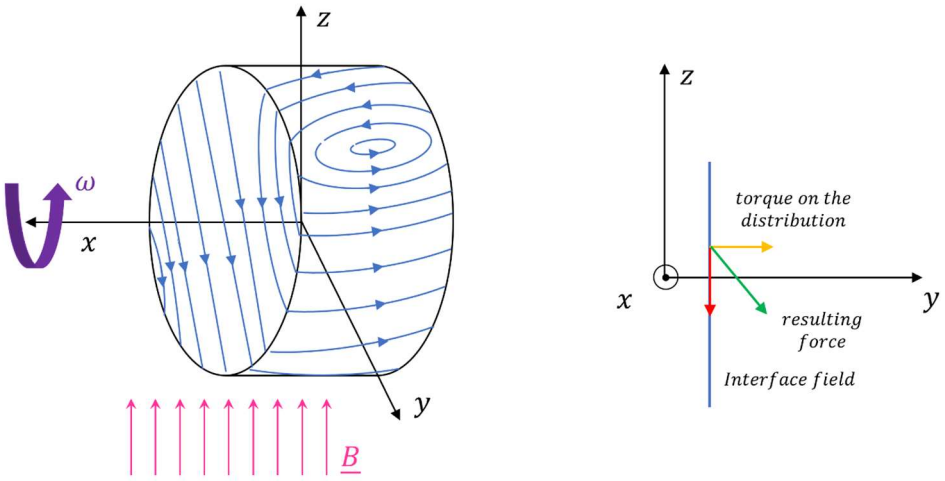

Fig. 69 High speed current path

6.2 The effect of speed and magnetic field intensity

Having found that the worst case scenario corresponds to the condition $\alpha = 90°$, all the simulations from this point on are performed under this assumption in order to obtain conservative results.

The next parameters analysed are the rotational speed of the impeller and the magnetic field intensity itself.

In particular Fig. 70 shows the effect of speed on the braking torque magnitude where a fairly linear profile can be appreciated, while Fig. 71 shows the effect of the magnetic field intensity.

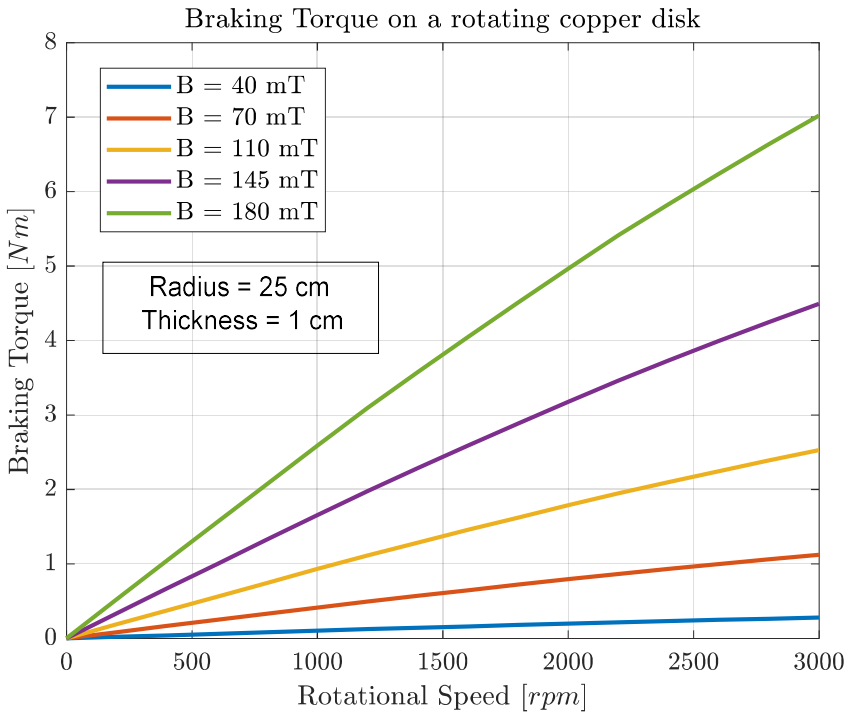

Fig. 70 Speed dependence of the braking torque on a copper disk

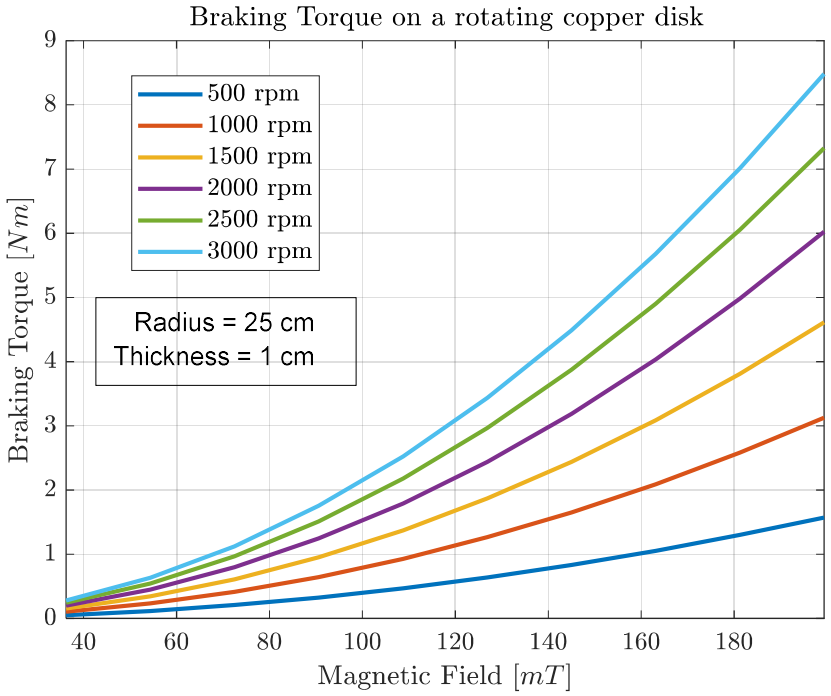

Fig. 71 Magnetic field intensity dependence of the braking torque on a copper disk

6.3 The effect of dimensions

The effect of the disk radius and thickness (respectively Fig. 72 and Fig. 73) is analysed in this paragraph at a fixed magnetic field intensity and rotational speed. It can be appreciated from both from the following figures that the increase of the linear dimensions of the disk determines a quadratic increase in the braking torque.

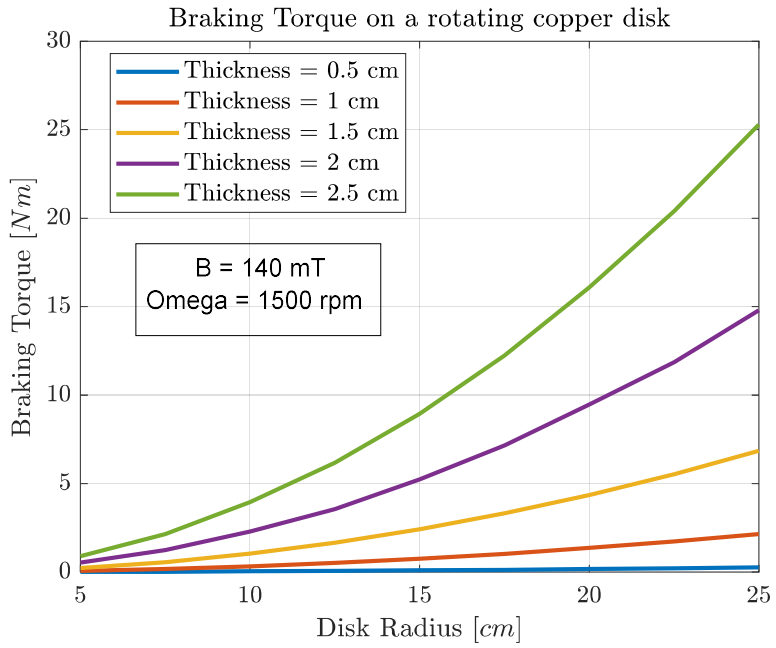

Fig. 72 Radius dependence of the braking torque on a copper disk

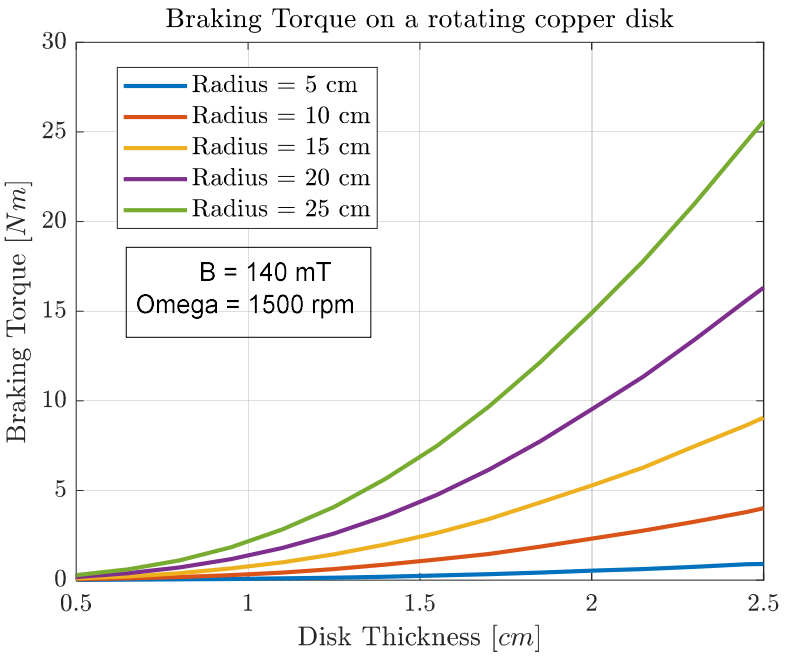

Fig. 73 Thickness dependence of the braking torque on a copper disk

6.4 Constant cross section analysis

The previous section showed that increasing dimensions of the disk implies increasing the braking torque, as a matter of fact this results obvious as a larger conductive object determines on the one hand a lower electrical resistance and a larger cross section on the other hand.

Therefore, it is interesting to study what happens to the braking torque on the disk when its cross section is kept constant and its ratio radius over thickness varies.

Indeed, one should expect that a particular ratio r (denominated here critical ratio r_c) maximizes the braking torque and for values greater and smaller than r_c the braking torque decreases.

Hence the simulations were performed at a fixed magnetic field intensity equal to 100 mT , for an aluminium disk rotating at different speeds and according to the sketch depicted in Fig. 74:

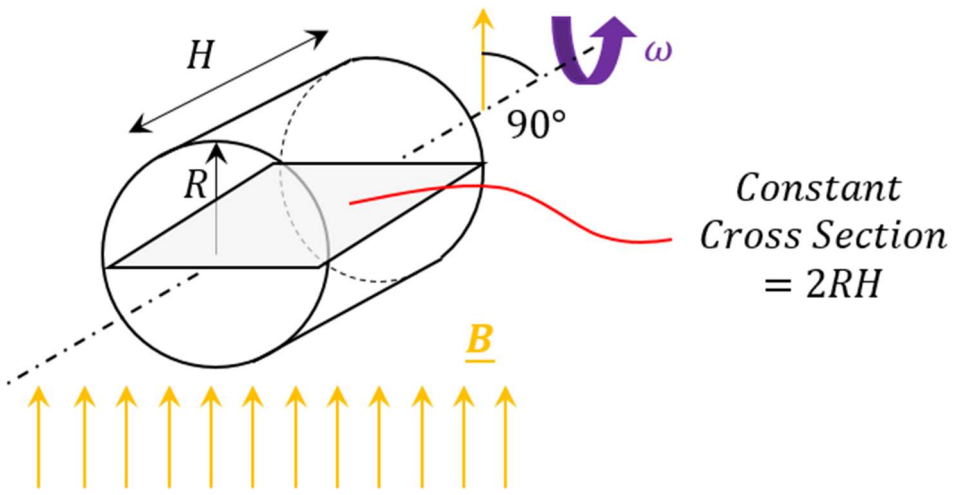

Fig. 74 Simulation sketch of a conductive disk rotating in a uniform SMF with constant cross section and varying radius and thickness

The first set of simulations was carried out adopting a 40 cm^2 cross section; such value is changed in the 2nd and 3rd set of simulation in order to compare the effect of the cross section itself on the critical ratio r_c.

It is easy to notice from Fig. 75 that there exist a critical ratio r_c which maximizes the braking torque and more specifically, this ratio depends on the speed.

On the other hand Fig. 76 and Fig. 77 show that the qualitative profile of the braking torque as a function of the ratio R/H is qualitatively the same for different cross sections, i.e. there exist always a critical ratio r_c, however, such ratio furtherly

depends on the cross section itself as the curves are characterized by a “smoother” profile at a fixed x-scale.

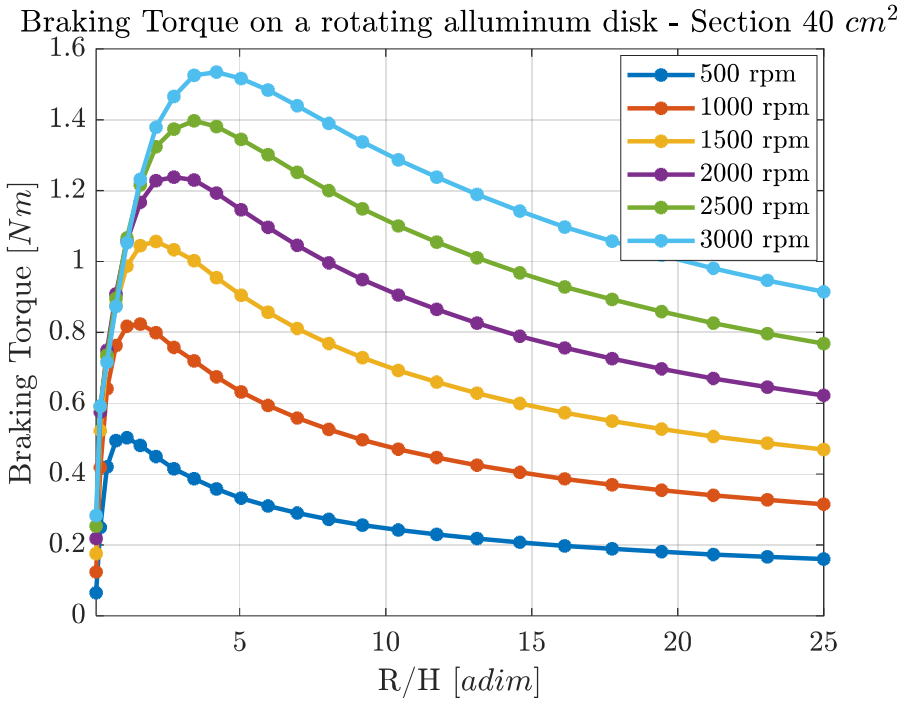

Fig. 75 40 cm^2 constant cross section simulation of an alluminum disk rotating inside a magnetic field

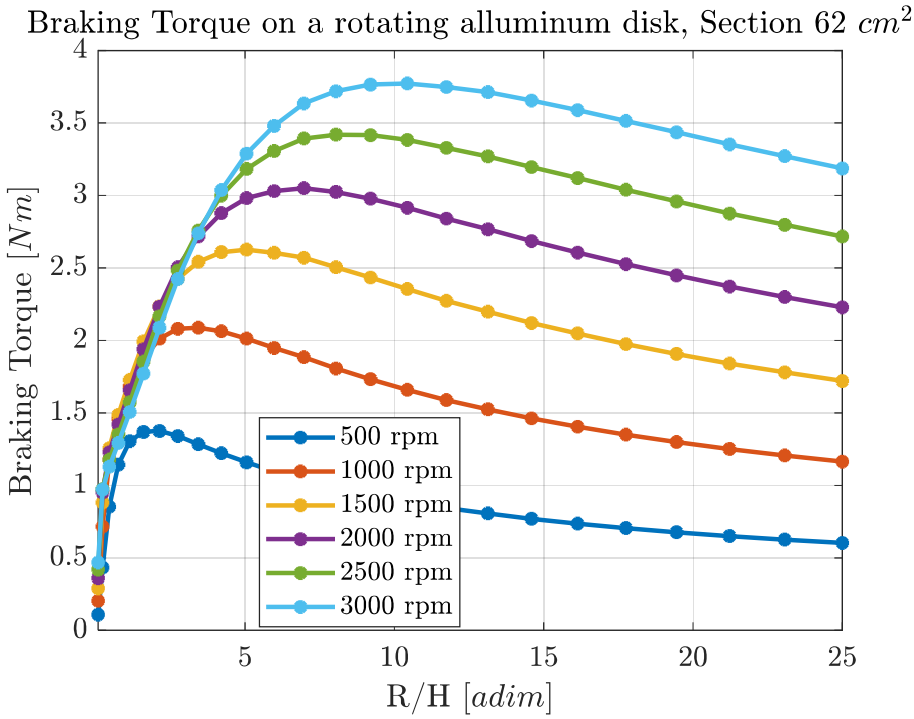

Fig. 76 62 cm^2 constant cross section simulation of an alluminum disk rotating inside a magnetic field

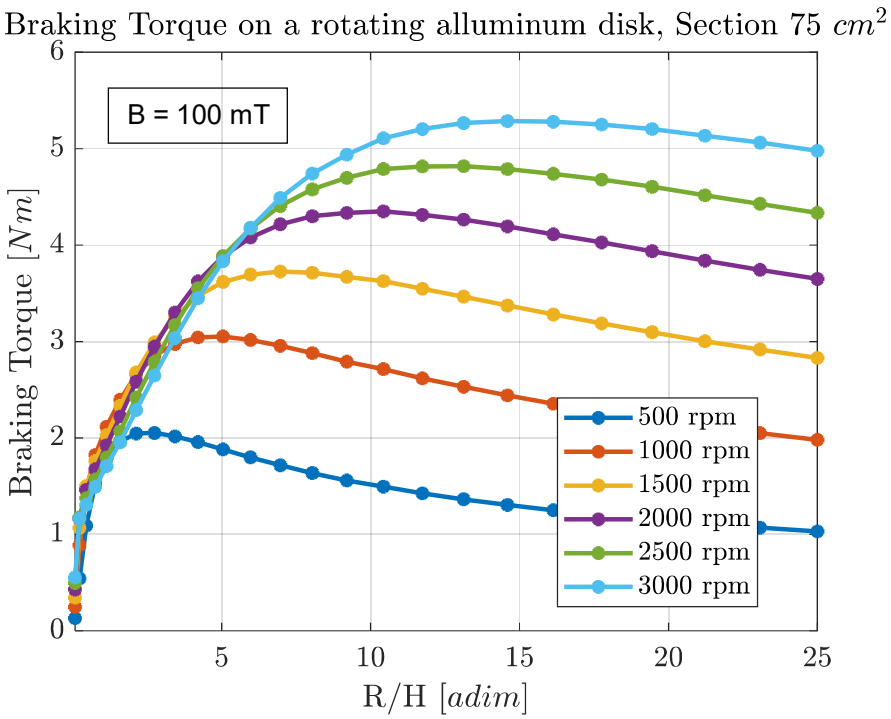

Fig. 77 75 cm^2 constant cross section simulation of an alluminum disk rotating inside a magnetic field

Finally, both the dependence of r_c on speed and cross section in shown in Fig. 78:

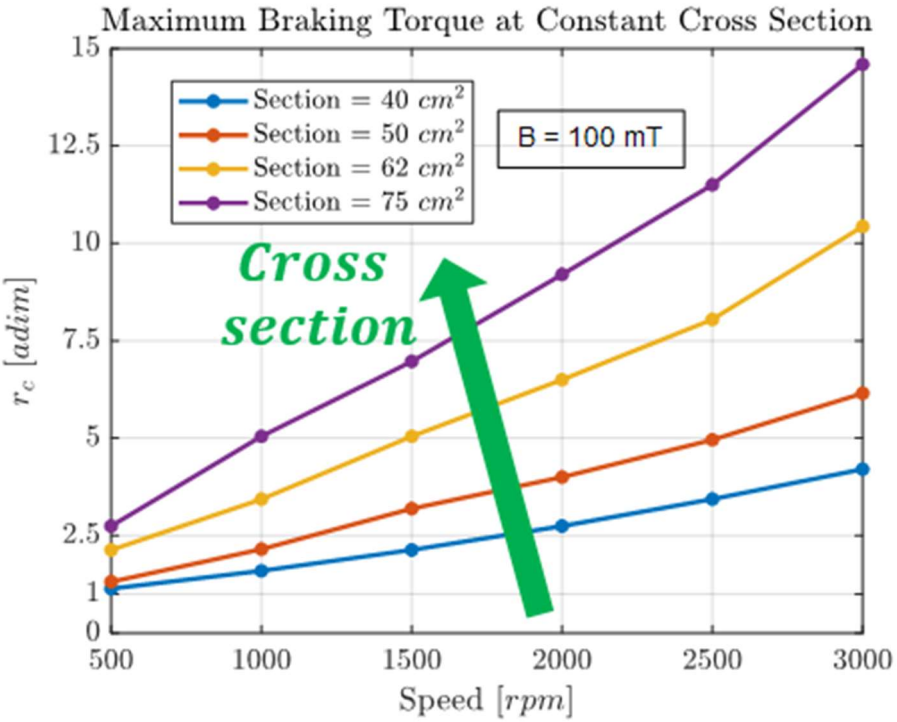

Fig. 78 r_c dependence on speed and disk cross section

On balance, the larger the disk and the faster it rotates the torque is maximized (at constant cross section) by cylinders whose radius is far greater than its thickness.

6.5 Summary

Some basic and useful information can be drawn from these preliminary results:

- The physical mechanism causing the eddy current circulation in the disk is explained
- The braking torque increases linearly with the speed.
- The angle between the magnetic field lines and the rotation axis which maximizes the torque is equal to 90 deg.
- The braking torque dependence on the magnetic field intensity is quadratic. This means that magnetic field variations at higher values have a higher impact than magnetic field variations at lower values.
- The physical coherence of the simulations has been verified thanks to the constant section analysis, indeed the braking torque profile as a function of R/H goes to zero for $R >> H$ and $R << H$ as the equivalent electrical resistance goes to infinity. At the same time the torque is maximized for an intermediate value of R/H, depending on the speed and the cross section itself.

7 Analysis of simplified impeller geometries

Thanks to the use of Maxwell/ANSYS it is possible to simulate objects characterized by a very complex geometry, however meshing operations becomes more complicated and the overall computation time, necessary to obtain the results, might excessively increase.

This is the reason why studying which simplified impeller geometries are able to reduce the complexity of meshing operation, reduces the computational effort and provides conservative results at the same time, represents an interesting aspect worthy of evaluation.

Therefore 3 different geometries (shown in Fig. 79) were selected and compared. In particular, impeller 3 is the "reference" (as it represents a more realistic impeller) to which the other two are compared.

Impeller 1 was obtained maintaining the volume of each blade of impeller 3 constant, but changing their shape in order to achieve the maximum degree of simplification (i.e. making them rectangular).

Finally, Impeller 2 has always blades whose volume is equal to the one of the blades of impeller 1 and 2 and it represent a middle ground between the other two solutions

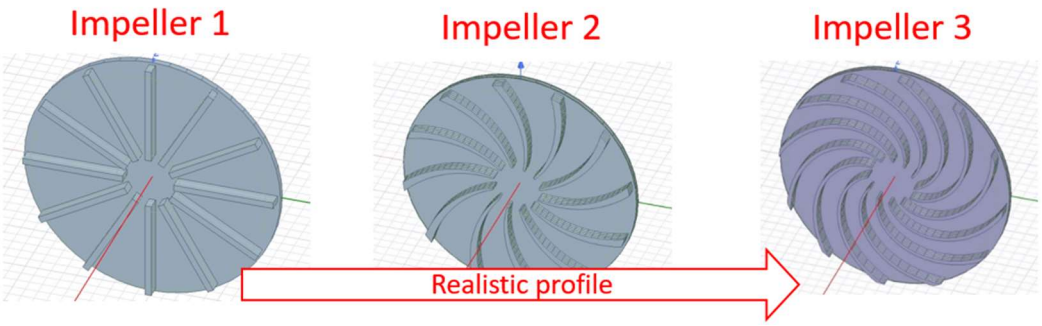

Fig. 79 Impeller geometries selected for the study

In this particular analysis the impellers are left "open" as the upper part closing the channels (equal for the 3 cases) would only add a braking torque offset identical for each geometry.

The braking torque on impeller 1, 2 and 3 are respectively shown in Fig. 80, Fig. 81 and Fig. 82.

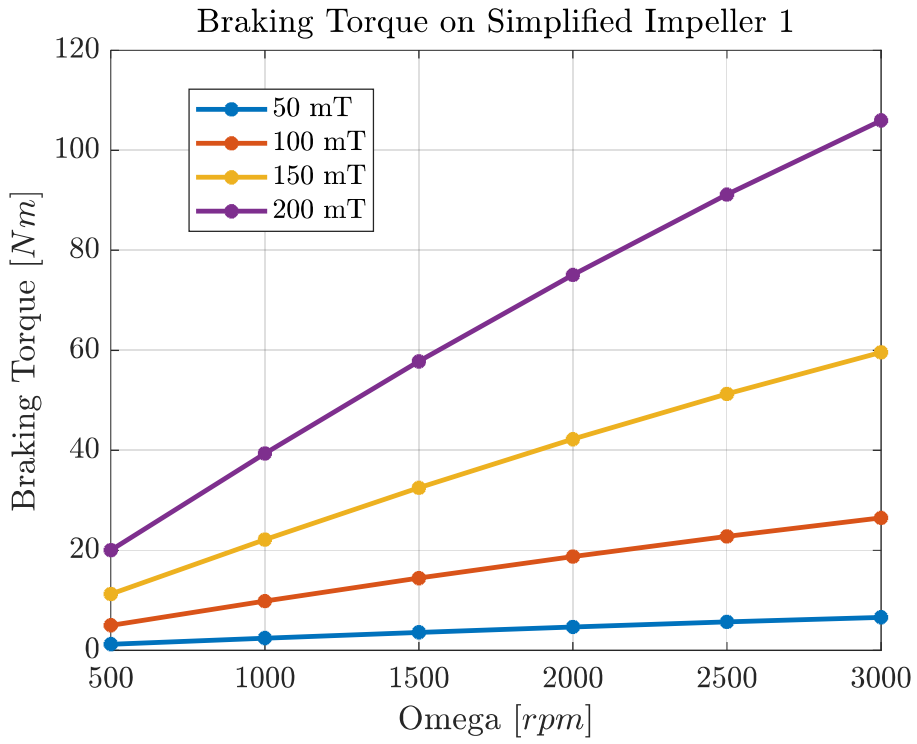

Fig. 80 Braking torque on impeller 1

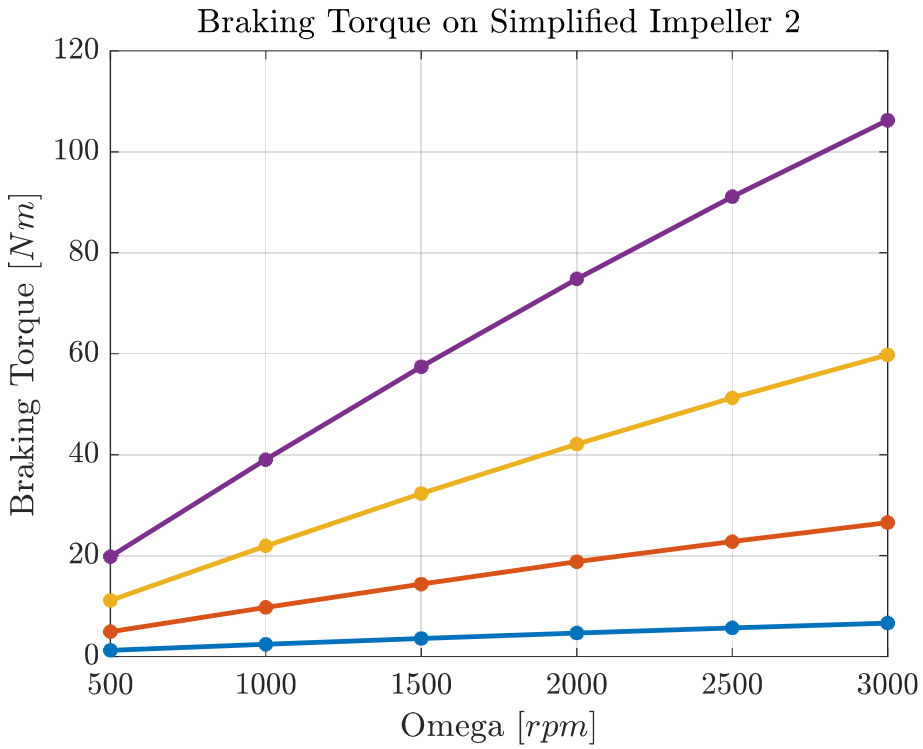

Fig. 81 Braking torque on impeller 2

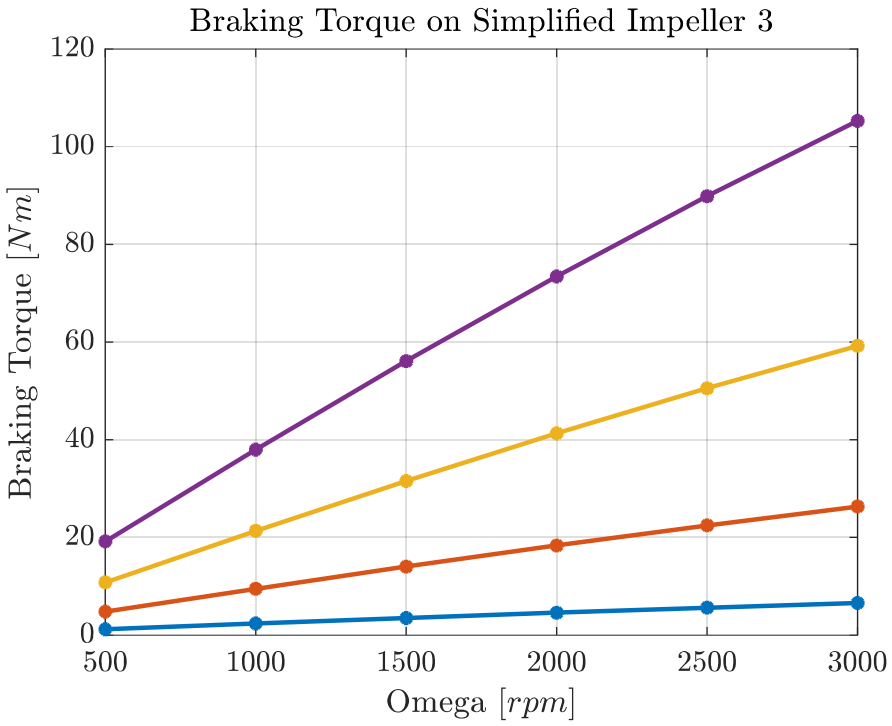

Fig. 82 Braking torque on impeller 3

From these plots it is difficult to quantify the differences between the braking torque values on each impellers, therefore, Fig 83 shows the difference in percentage with respect to impeller 1.

It is immediate to observe that impeller 2 and 3 have a lower braking torque (negative percentage difference) in the speed range 0 rpm – 3000 rpm.

The plot continues for higher speed in order to show the physical correctness of these results as the curves approach to zero, as a matter of fact it would have been unrealistic if the linear trend would remain unchanged after 3000 rpm (i.e. it would not be physically sensible if the braking torque associated to the impellers characterized by more straight blades becomes lower after a certain speed value).

As a final remark the fluctuation of the results after 3000 rpm is due to numerical errors, as the percentage difference of the braking torque between the impellers is significantly low.

On balance, what Fig. 83 states is that in speed range 0 rpm – 3000 rpm the simplified impeller with straight blades is subjected to a higher braking torque, therefore it represents a conservative impeller geometry and simpler to simulate at the same time.

The reason behind these results is given by the different electrical resistance of the impellers due to the different blade shapes, indeed as the blades become more and more “realistic” (i.e. going from impeller 1 to 3), they become thinner and longer

at constant volumes, therefore increasing the electrical resistance of the impeller, determining lower eddy currents and thus a lower braking torque.

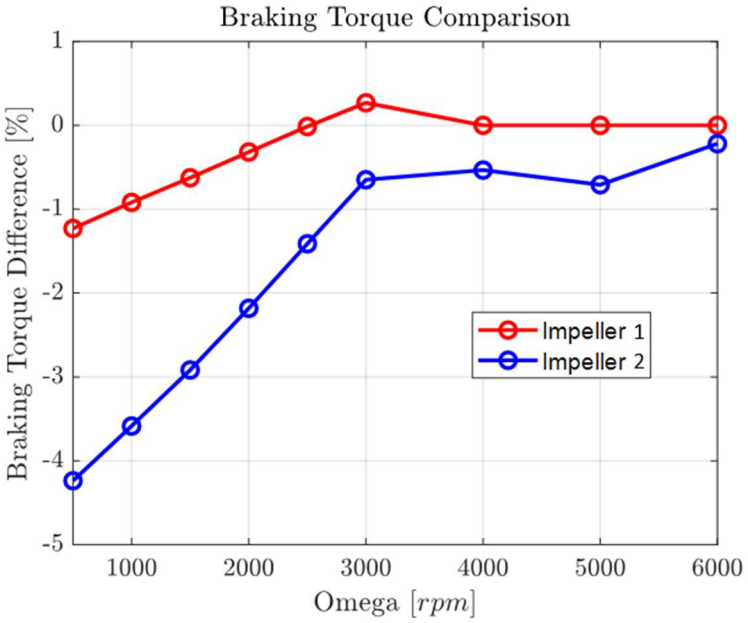

Fig. 83 Breaking torque percentage difference of impeller 2 and 3 compared to impeller 1

Finally Fig. 84 shows the current path inside impeller 2 at 1000 rpm:

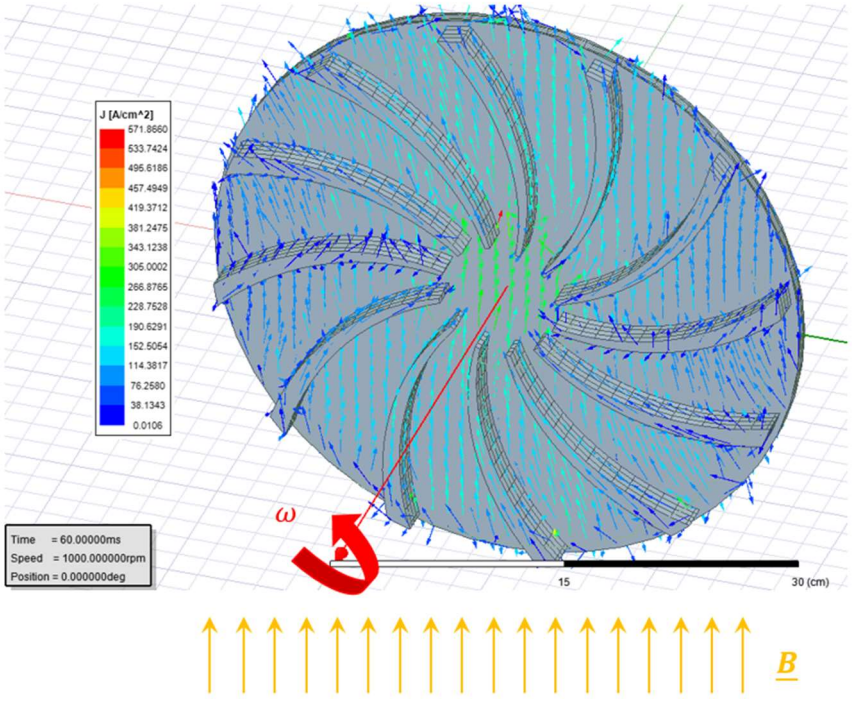

Fig. 84 Current path inside impeller 2 at 1000 rpm

8 Study of real impellers

This section is dedicated to the analysis of real impellers operating in a uniform SMF, the presence of the shaft is neglected in the first approach, while it is taken into account in the second part of this section.

Please notice that unless specified differently, all the simulations are carried out with a magnetic field perpendicular to the rotation axis.

8.1 Analysis of impellers with no shaft

The study rotates around two main impeller models, a low power one – 4kW and a high power one - 200kW. Both models and their relative data were provided by the company Termomeccanica Pompe.

In particular, the main data necessary for the simulations are listed in Table 8 where μ_r is the relative magnetic permeability and σ is the bulk conductivity:

Table 8 Pump Data

Pump 1		Pump 2	
Power	4 kW	Power	200 kW
Speed	2950 rpm	Speed	2950 rpm
Material	Cast Iron $\mu_r = 60, \sigma = 1.5 \cdot 10^6\ S/m$	Material	Cast Iron $\mu_r = 60, \sigma = 1.5 \cdot 10^6\ S/m$

8.1.1 Low power pump

The 4kW pump is analysed here, its impeller 3D model is shown in Fig. 85:

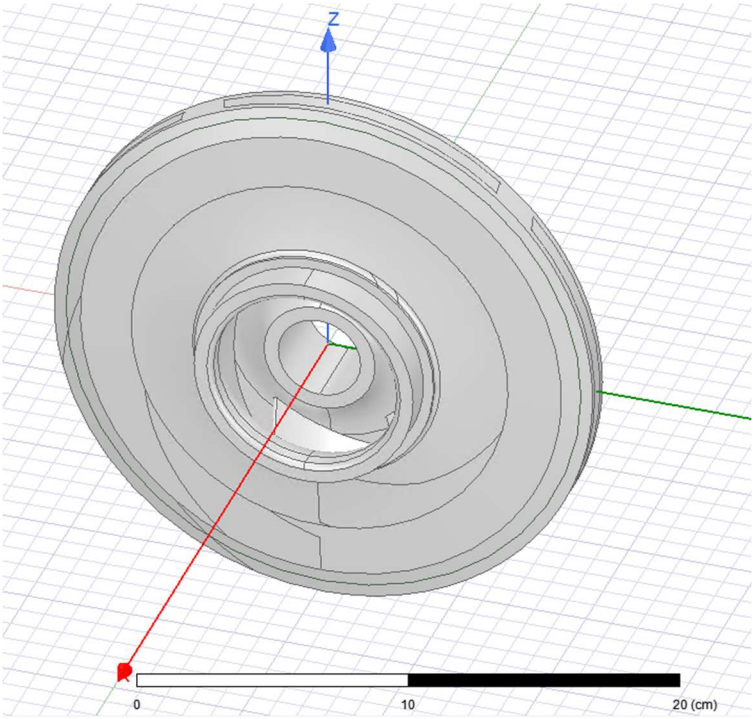

Fig. 854kW Termomeccanica Pompe impeller

While its braking torque and the consequent braking power are shown in Fig. 86 and Fig. 87.

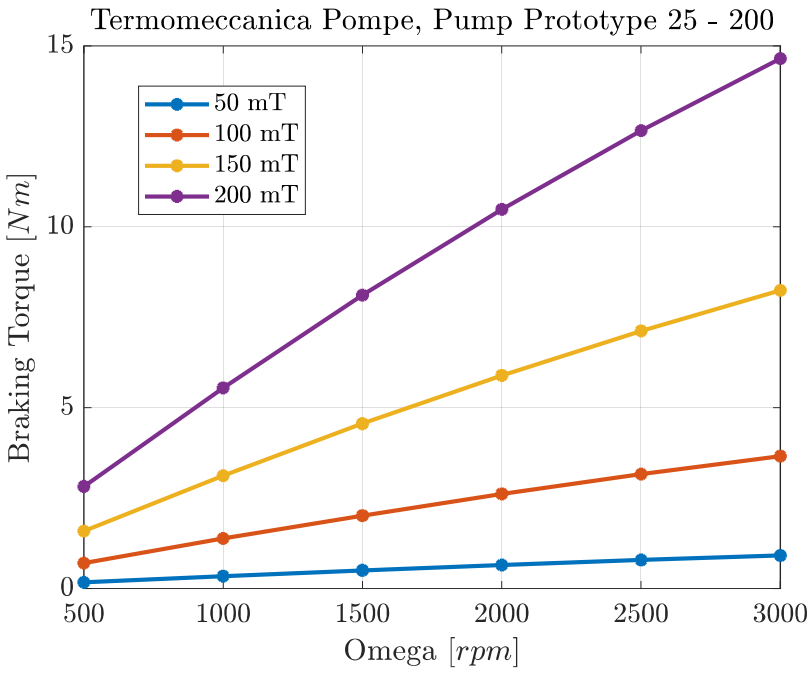

Fig. 86 4kw Pump braking torque

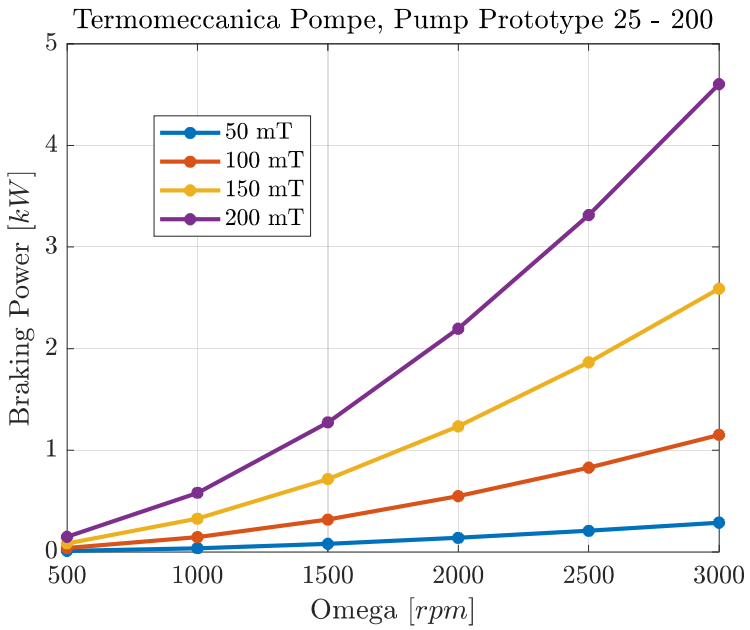

Fig. 87 4kw Pump braking power

However, what is meaningful in this situation is the extra load compared to pump rated power determined by the magnetic field in all the working conditions. Thus, this quantity was computed and plotted in Fig. 88. However, perhaps the most informative result is the maximum load to which the pump is subjected to as a function of the magnetic field intensity. In particular, the maximum load is obtained considering a 3000 rpm speed and a perpendicular magnetic field; the resulting curve is plotted in Fig. 89.

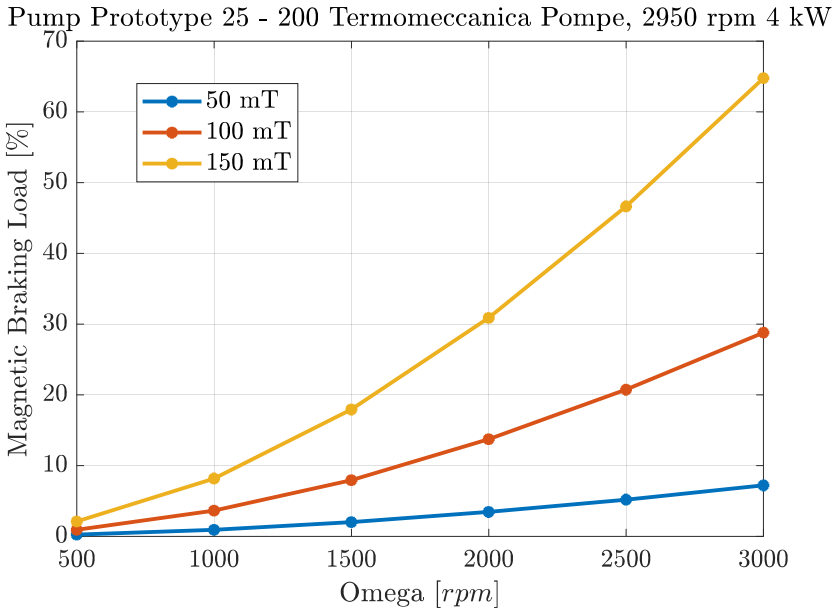

Fig. 88 Relative load for the 4kW pump as a function of speed for different values of magnetic field

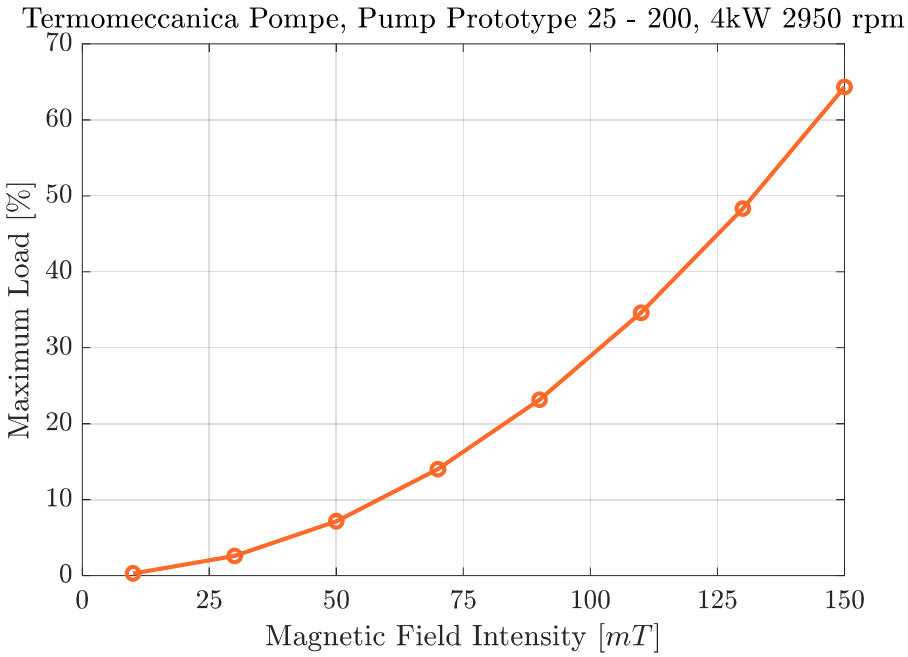

Fig. 89 Maximum load for the 4kw pump

From a quick look of Fig. 89 the following rough but meaningful information can be acquired:

- The maximum load on the analysed pump is less than 10% for a magnetic field intensity up to 50 mT
- The maximum load on the analysed pump is less than 20% for a magnetic field intensity up to 75 mT
- The maximum load on the analysed pump is around 30% for a magnetic field intensity around 100 mT

Finally, a sensitivity analysis is performed. The parameters under observations are the electrical conductivity and magnetic permeability (the same 4kW cast iron impeller is analysed, please refer to Table 9 for the material properties). The results are shown in Fig. 90:

What can be observed from these results is that the electrical conductivity represent a more critical parameter compared to the magnetic permeability as its increase determines a greater increase in the braking torque.

Roughly for this pump model, a 5% increase in the conductivity determines a 4% increase in the braking torque, a 10% determines an 8% increase and a 20% causes a 15% increase.

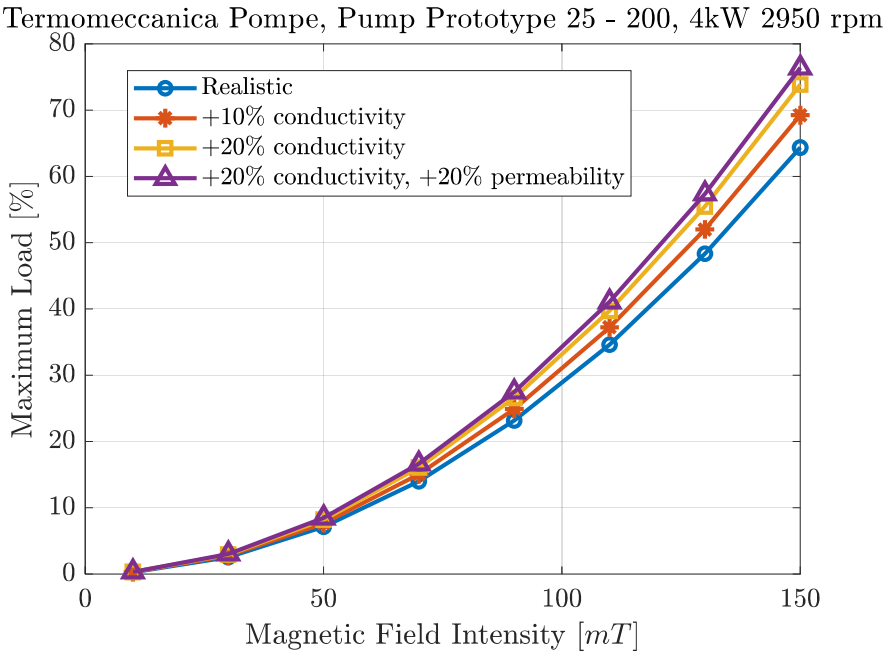

Fig. 90 Sensitivity analisys

8.1.2 High Power Pump

The 200kW pump is analysed here, its impeller 3D model is shown in Fig. 91:

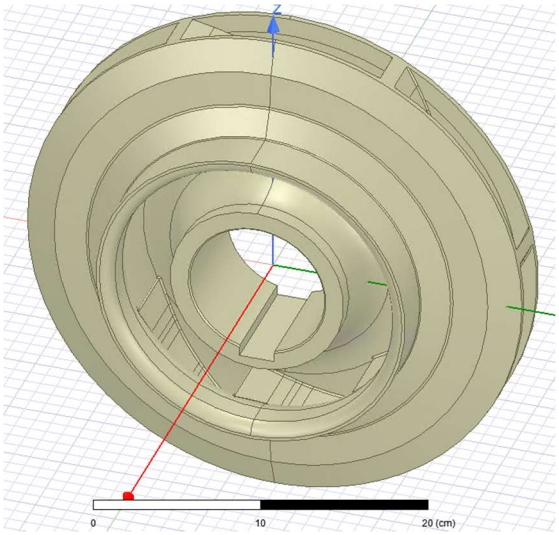

Fig. 91 Termomeccanica Pompe impeller

The braking torque absolute value is not shown here for brevity's sake, while the stress is put on the relative load as it represents a more meaningful quantity. Hence, Fig. 92 shows the relative load as a function of the speed and the magnetic field intensity as parameter:

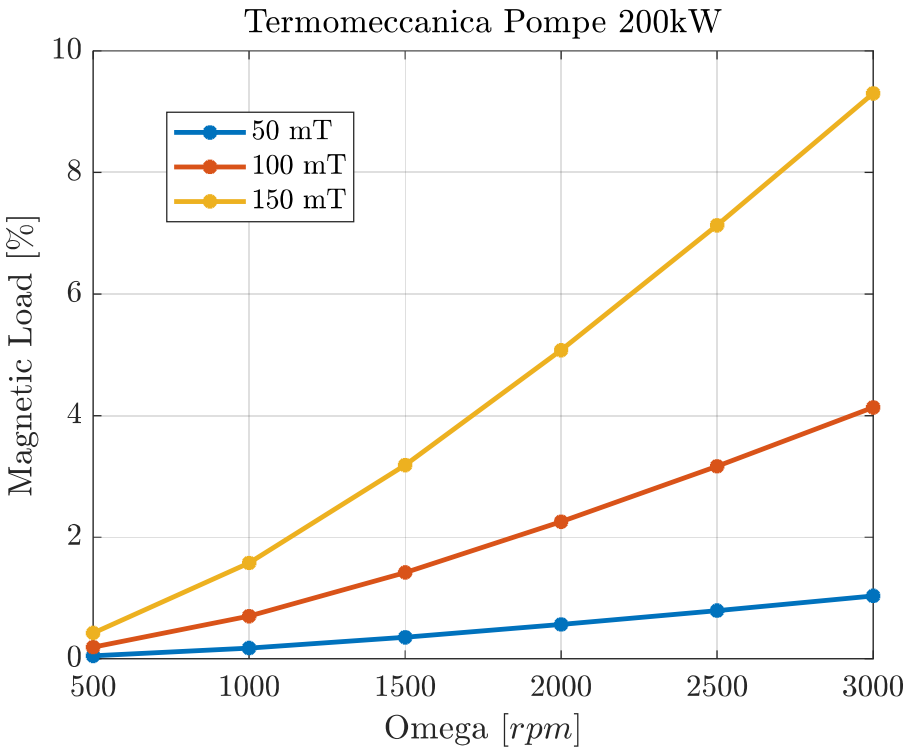

Fig. 92 Relative load for the 200kW pump

While Fig. 93 shows the 200kW pump maximum load compared to the one already presented for the 4kW pump.

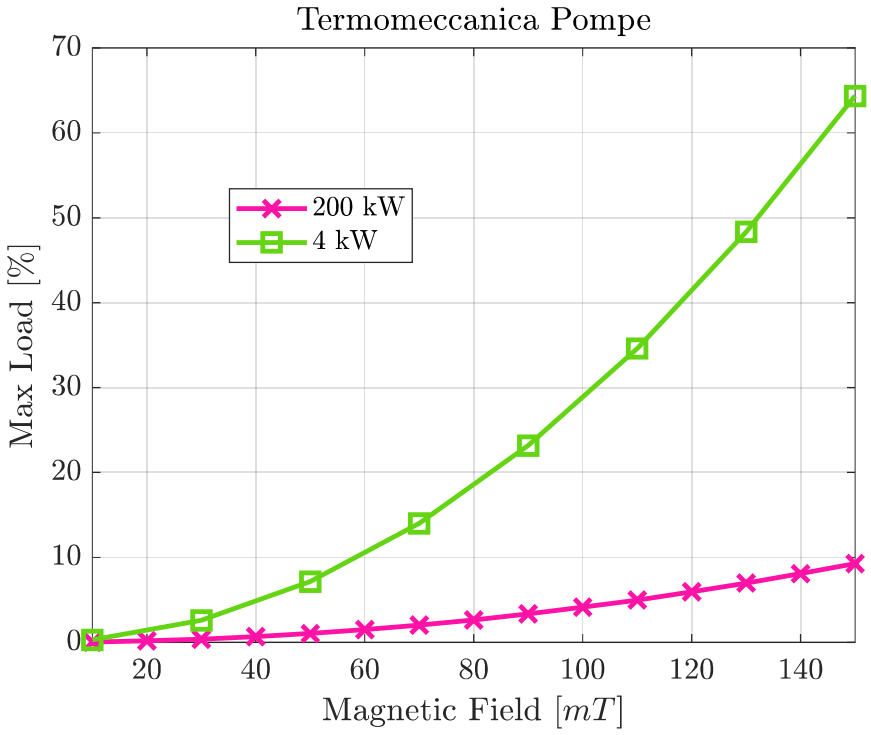

Fig. 93 Maximum load comparison

Observing the pink curve from Fig. 93 one can roughly estimate that:

- The maximum load on the analysed pump is less than 5% for a magnetic field intensity up to 100 mT
- The maximum load on the analysed pump is around 10% for a magnetic field intensity around 150 mT

In addition, it is evident that the maximum relative load for the high power pump is remarkably lower the one for the low power pump.

In order to provide a physical explanation for this fact, the dependence of the braking torque and the power of the pump on the impeller dimension has to be known.

It is known that the power P delivered from to impeller to the fluid at constant speed is proportional to the product of the flow rate Q and the head weight H (i.e. $P \propto HQ$). In addition, the head weight is proportional to the square of the impeller diameter, while the flow rate is proportional to the diameter for radial flow centrifugal pumps with trimmed impellers (i.e. $H \propto D^2$ and $Q \propto D$).

Thus, the pump power is proportional to the cube of the impeller diameter (i.e. $P \propto D^3$).This is true provided that the two pumps or fans are dynamically similar, see [38] for any reference.

On the contrary, it can be verified with some quick simulations that the magnetic braking power P_B at constant speed is proportional to the square root of the diameter (i.e. $P_B \propto D^{1/2}$).

As matter of fact, one can verify easily that a constant speed, for a conductive disk with a fixed thickness, the braking torque increases linearly with the volume (see Fig. 94), meaning it increases linearly with the diameter squared root.

Therefore, making the assumption that real impellers can be approximated to disks, the power of the pump increases far faster with the diameter than the braking torque determined, making high power pump less influenced by the magnetic field.

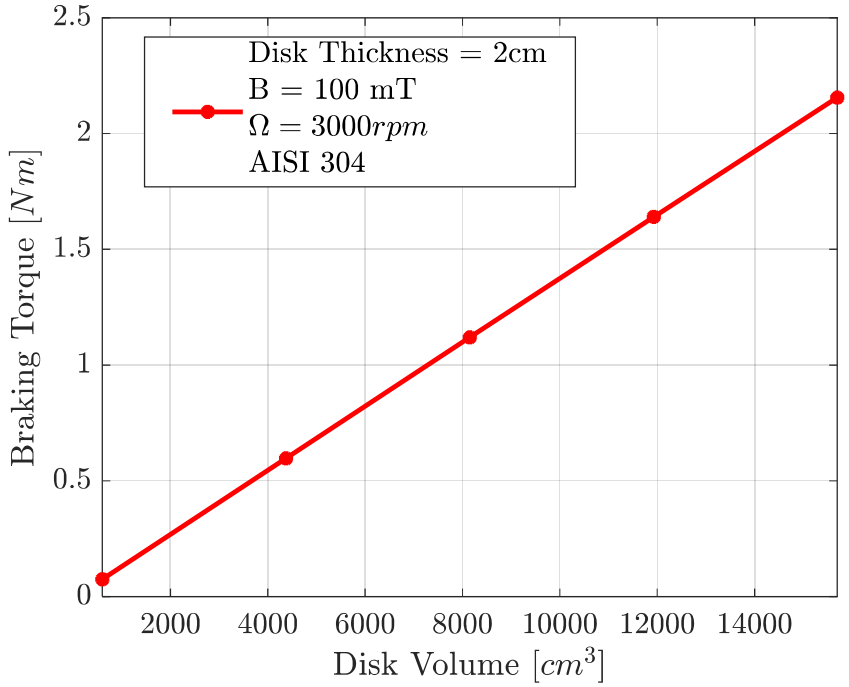

Fig. 94 Disk braking torque dependence on its volume at constant thickness

8.2 Analysis of impellers with shaft

In this section the analysis is made more realistic by adding the shaft to the 3D impeller models. In particular the goals here are:

- Quantify the impact of the shaft on the overall braking torque.
- Study the dependence of the overall braking torque on the shaft length.

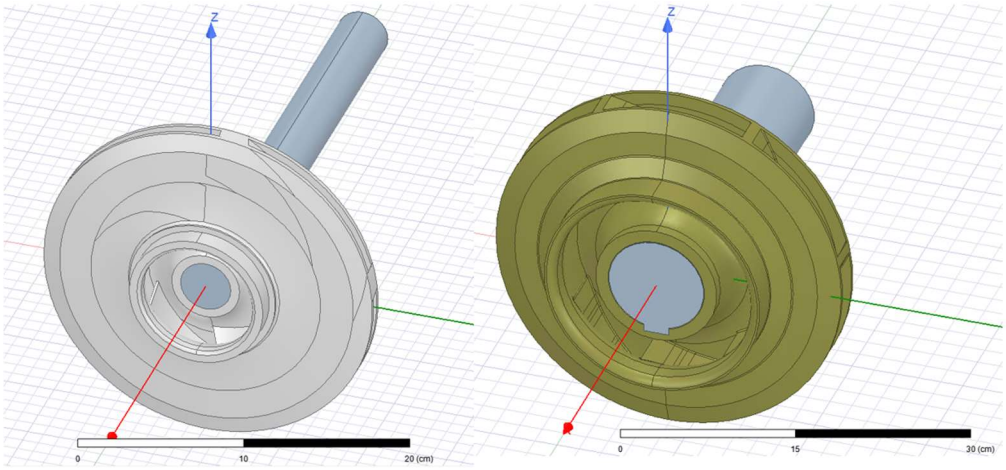

- *Fig. 95 Termomeccanica pomper impellers 3D models with shaft*

The properties of the materials simulated are listed in Table 9:

Table 9 Material properties

	Material	**Relative Permeability**	**Bulk Conducitivity [S/m]**
Impellers	Cast Iron	60	1.5 · 10^6
Shafts	AISI 304	1.008	1.38 · 10^6

The results of the simulations are shown in Fig. 96 and Fig. 97 respectively for the 4kW and 200kW pump.

One can notice comparing Fig. 96 with Fig. 89 and Fig. 97 with Fig. 92 that the presence of the shaft has negligible influence on the braking torque value. Besides, from Fig. 96 and Fig. 97 one can notice that all the curves are all overlapped, meaning that the braking torque associated to shaft is far lower than the braking torque associated to the impeller even when the shafts length is significantly increased.

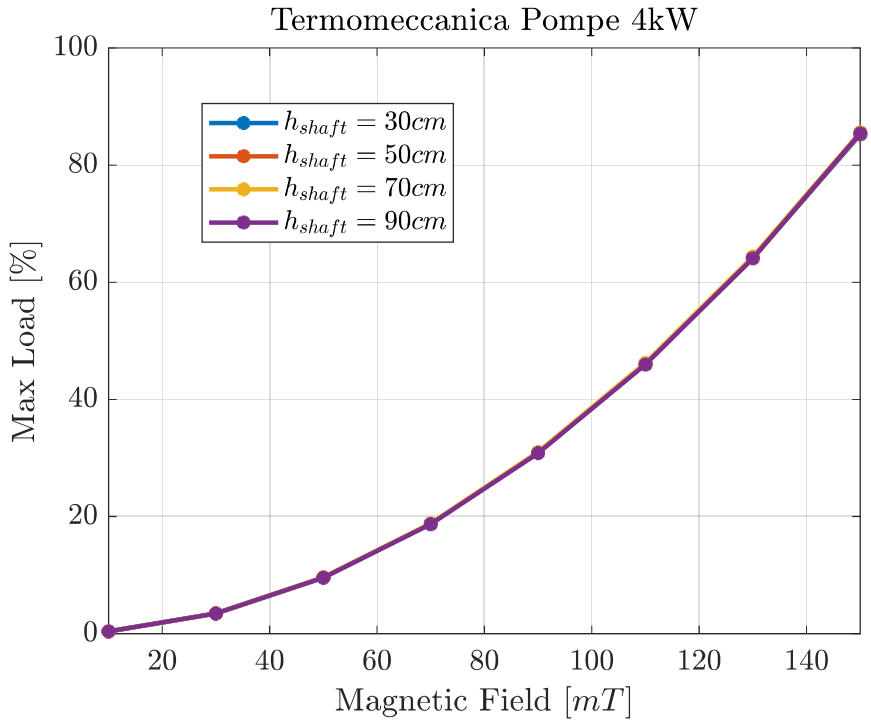

Fig. 96 Maximum load of the 4kW pump with shaft:

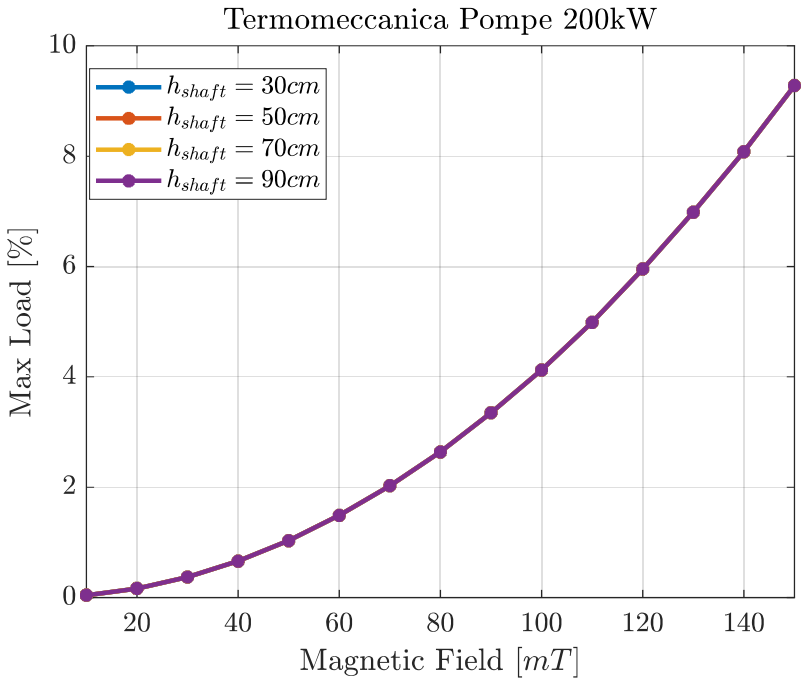

Fig. 97 Maximum load of the 200kW pump with shaft

In order to further analyse this aspect, only the shaft was simulated in order to obtain the braking torque only related to this component. The shaft of the 4kW pump was considered. The results are shown in Fig. 99:

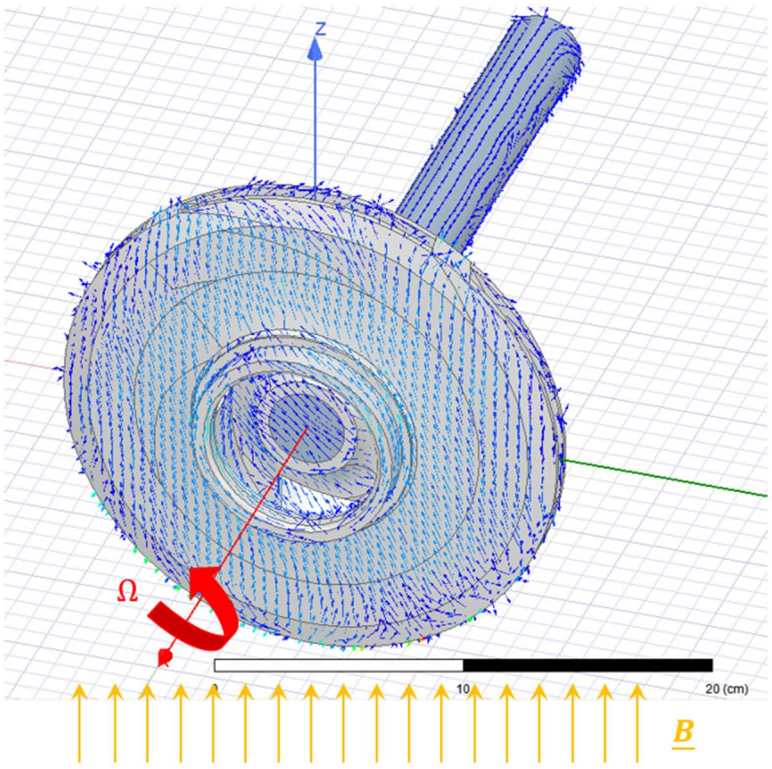

Fig. 98 Current path in 4kw impeller with shaft

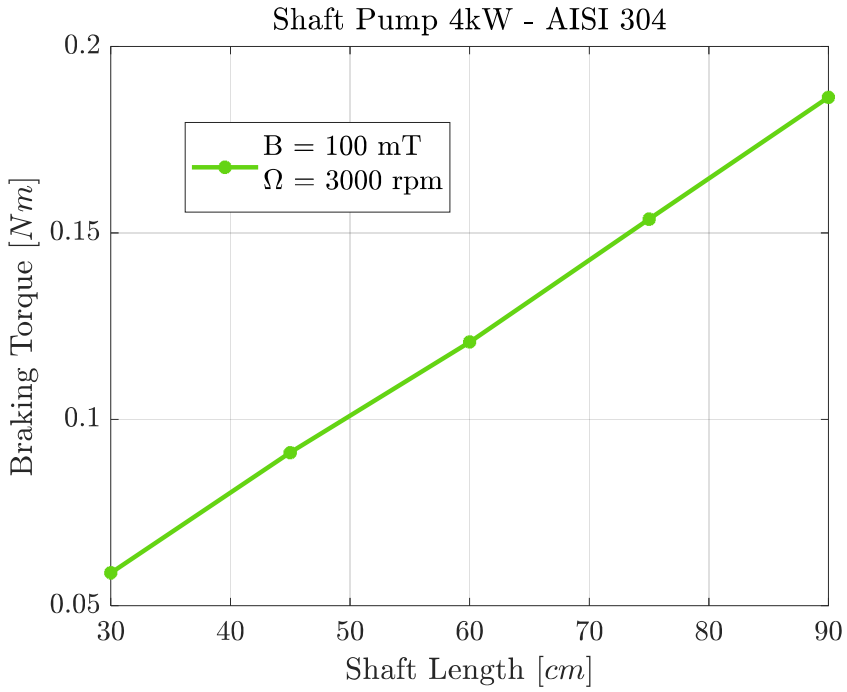

Fig. 99 Braking torque on the shaft of the 4kW pump

Already from Fig. 99 one can observe that the braking torque values are one order of magnitude less than the results for the impeller, in particular, this is even clearer if one compares the two results in the same operating condition (i.e. at 3000 rpm and 100 mT) with Fig. 100 (last orange dot).

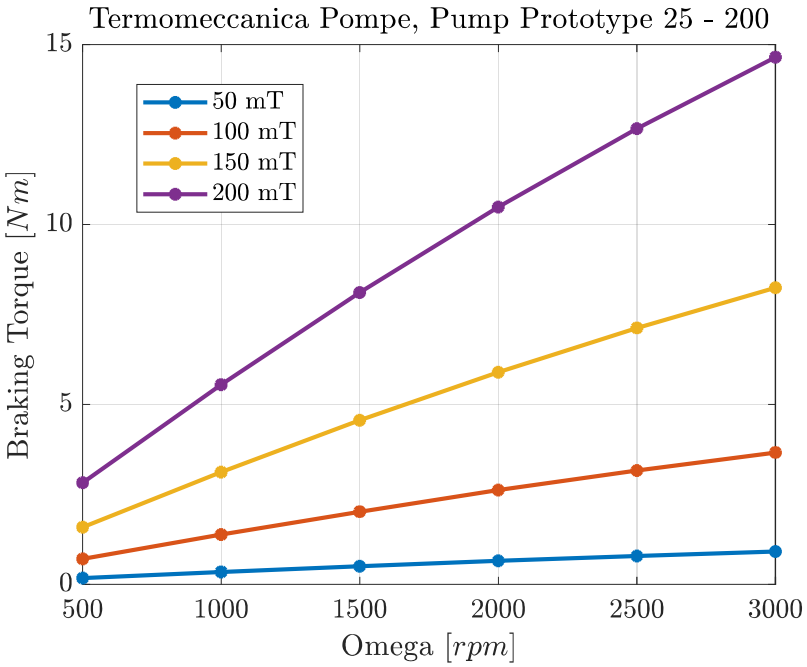

Fig. 100 Braking torque on the 4kW pump

The reasons for this difference in the braking torque values can be attributed to three causes:

- The conductivity of the shaft is lower than the one of the pump (shaft material AISI 304)
- The shaft material is not ferromagnetic (i.e. it is characterized by a 60 times lower magnetic permeability in this case)
- The ratio r is far lower than 1.

8.3 The importance of orientation

It is already shown in this report that the braking torque on a perfect circular disk rotating in a uniform magnetic field parallel to its axes is zero. One can expect therefore that the braking torque is minimized for a real impeller when its axes is aligned with the magnetic field.

Thus the following simulation was performed in order to evaluate the impact on the braking torque that has the angle between the magnetic field and the rotation axis of real impellers.

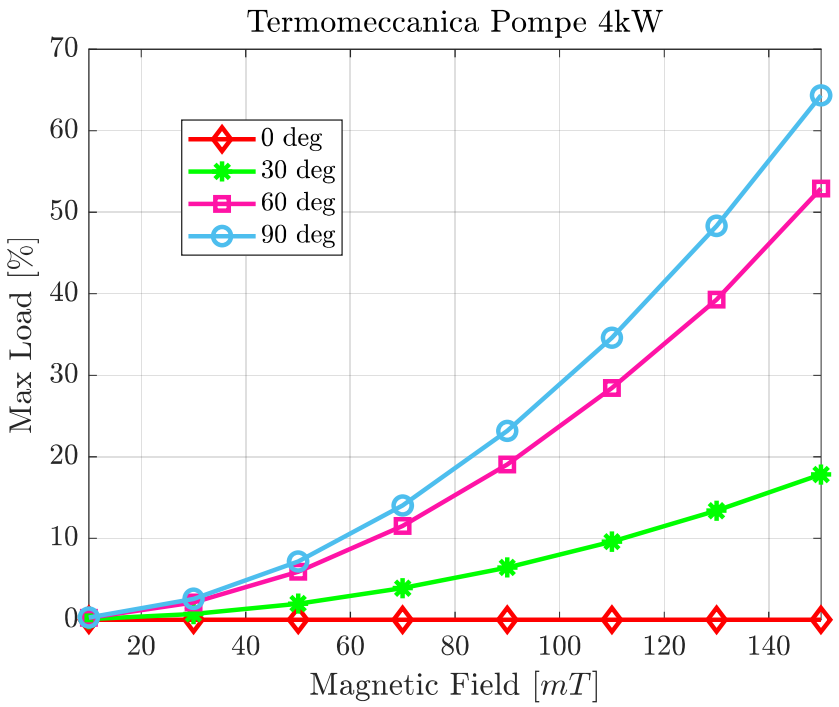

Fig. 101 Maximum load for the 4kW at specific angle values

Again, it is confirmed that effect of the magnetic field even for real impellers is negligible if its axes is parallel to the magnetic field.

Besides, as already noticed from Fig. 2 for disks and deductible from Fig. 101 for a real impeller, the dependence of the braking torque on the orientation of the magnetic field is proportional to $\sin(\alpha)$, where α is the angle between the impeller axes and the magnetic field lines (the magnetic field assumed to be uniform).

9 Study of an equivalent model for real impellers

Finally, a study on the real impeller geometry simplification is carried out in this section. The main goal is to reduce the real impeller to an equivalent disk and quantify the differences in the braking torque between the two.

The results of this study, not only allow to perform faster simulations and obtaining conservative results, but by eliminating the need of having the CAD drawing of the impeller to calculate the braking torque, they allow to estimate the magnetic load of future pumps only with a handful of simple data, before the entire impeller geometry is even designed.

The simplification procedure is very straightforward, the equivalent disk dimension is obtained as follows: 1) the diameter D is the same as the one of the impeller, 2) its thickness H is obtained from the diameter and the impeller mass M according to $H = 4M/(\rho\pi D^2)$ where ρ is the material density. Finally, in the simulation, the material of the disk obviously has to be the same as the one of the impeller.

Once the disk simplification is obtained the braking torque difference with the real impeller can be evaluated.

Table 10 Equivalent Disk Dimensions

Impeller	Diameter [cm]	Thickness [cm]	Material
4kW Termomeccanica	10.5	1.3295	Cast Iron
200kW Termomeccanica	15.6	2.2844	Cast Iron

The braking torque comparison between the real impellers and their equivalent disk can be observed in Fig. 102 and Fig. 103 for the 4kW and 200 kW respectively.

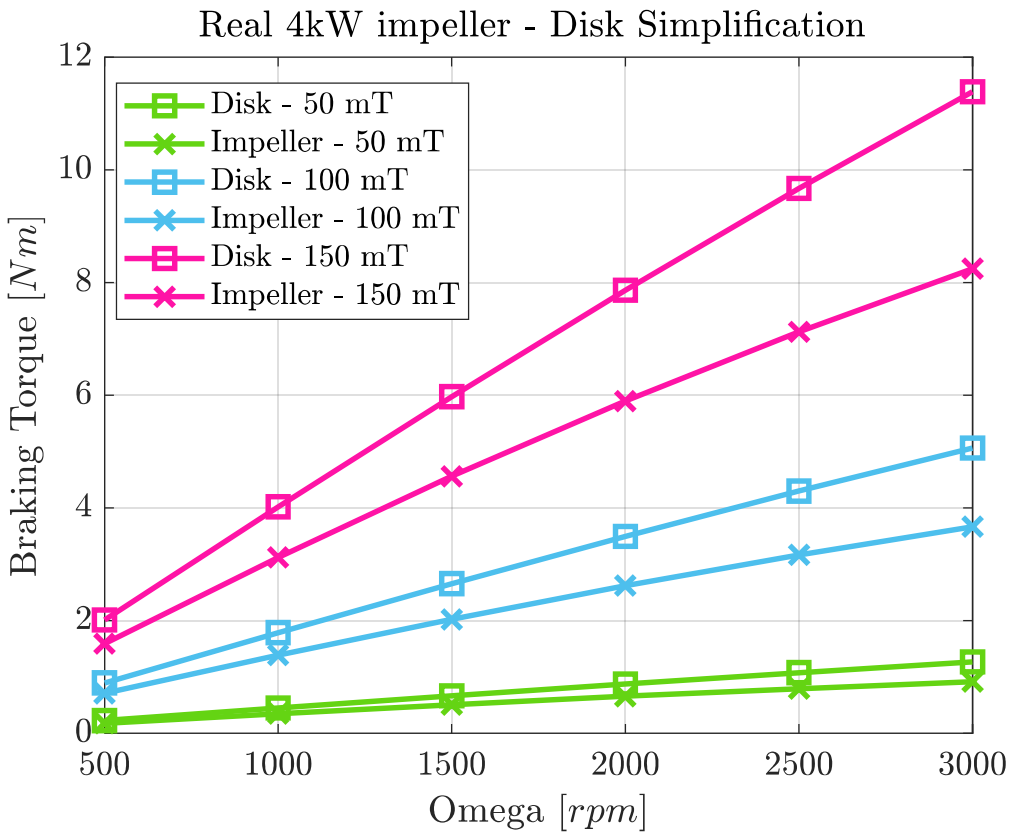

Fig. 102 Braking torque comparison between the 4kW impeller and its equivalent disk

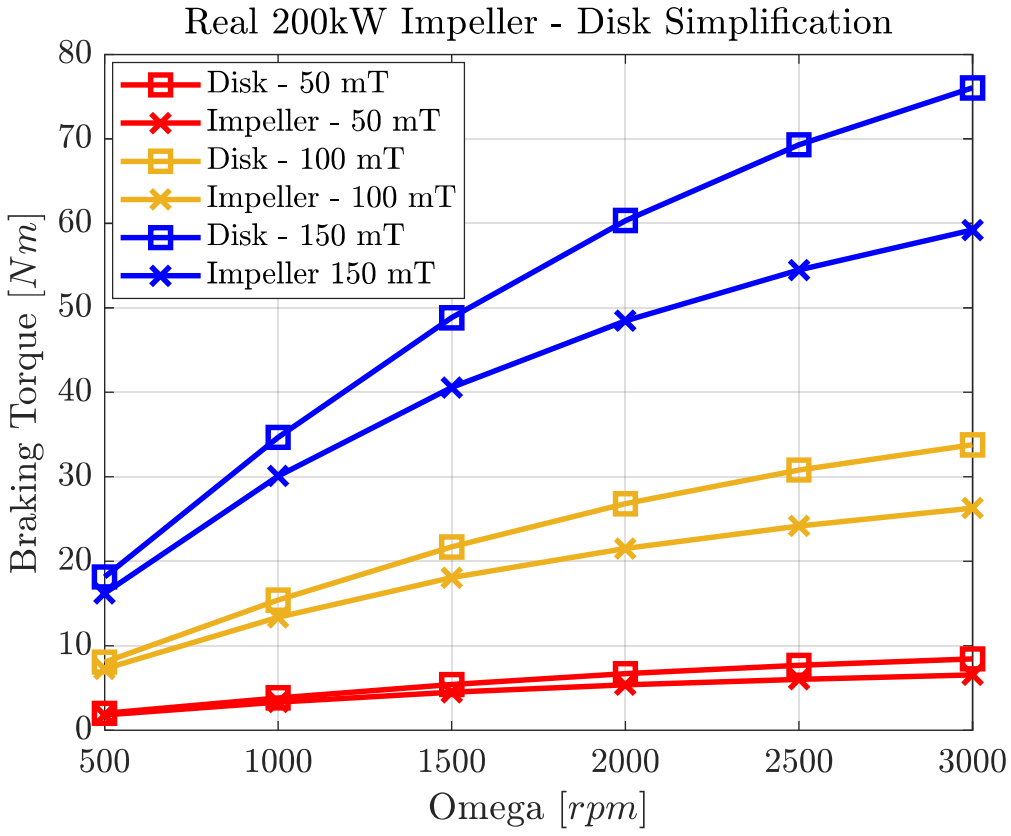

Fig. 103 Braking torque comparison between the 20kW impeller and its equivalent disk

And finally, the percentage difference of the braking torque on the equivalent disks with respect to the braking torque of the real impellers is shown in Fig. 104.

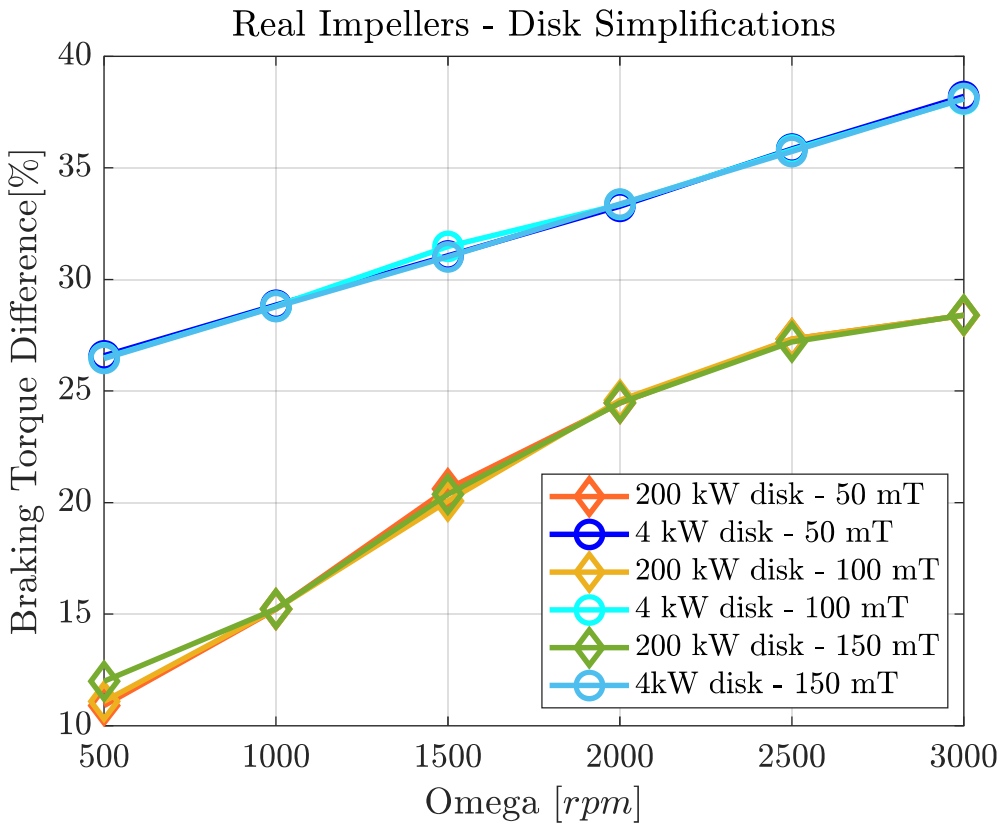

Fig. 104 Braking torque percentage difference

From these plots it important to notice that the equivalent disks always determine a higher braking torque, thus they provide conservative results for both the low and high power pumps.

The extent of the braking torque "surplus" determined by the equivalent disks is shown in Fig. 104.

It is easy to notice that the equivalent disk produces more accurate results for high power pumps, i.e. when the mass of the impeller is higher.

It is also interesting to notice the results for both disk become more conservative as the speed increases.

In order to complete this study it would be interesting to obtain a curve of the minimum scaling factor (once a minimum speed is fixed) depending on the pump power. For instance, here, assuming a minimum speed of 500 rpm one has a scaling factor around 1.1 for the 200kW pump and 1.25 for the 4kW pump.

Having such curve would allow to estimate (still conservatively, as this scaling factor increases with speed) the braking torque of any pump of any power (with a similar geometry) only by studying the behaviour of its equivalent disk.

A more sophisticated solution could also be to map this scaling factor not only depending on power, but on speed too, in order to estimate the braking torque of the real impeller without being conservative. However, this approach aiming at obtaining results that are more accurate, might be risky and it has to be validated through a higher number of simulations of a higher number of impellers.

Finally, an even more accurate equivalent model still able to provide conservative results would be impeller 1 from Fig. 79, however, this model can be adopted only if one has the information of the blade mass from which the straight blades can be obtained.

10 Conlcusions

10.1 Summary

A comprehensive study of rotating impellers in a uniform SMF was performed and developed on the basis of a staged approach: starting from simplified geometry the analysis was moved to more realistic objects up to the simulation of real impellers with their shafts.

The braking torque arising from the interaction between the Eddy currents and the external uniform SMF was evaluated and compared to the rated torque of each specific impeller in order to determine the additional mechanical load on the pump caused by the magnetic field.

Curves quantifying the maximum load for the analysed pumps are computed and presented in this report, also taking into accounts the presence of the shaft.

Two pumps were studied, a low power and a high power pump, the same analysis has been perform on each one of them showing and proving that high power pumps are less sensitive to the magnetic field. Unfortunately, the differences between the two impellers do not allow to use the affinity laws in order to reinforce the results obtained.

In addition, the effect of the orientation of the pump with respect to the magnetic field is studied, showing the impact it has on the resulting braking torque.

Finally, an equivalent model of real impellers has been studied and analysed in order to quantify its ability to produce accurate or conservative results

10.2 Key Results

The key results can be highlighted in this section.

As regards the Termomeccanica 4kW cast iron impeller the following results were obtained:

- The maximum load is less than 10% for a magnetic field intensity up to 50 mT
- The maximum load is less than 20% for a magnetic field intensity up to 75 mT
- The maximum load is around 30% for a magnetic field intensity around 100 mT

As regards the Termomeccanica 200kW cast iron impeller the following results were obtained:

- The maximum load is less than 5% for a magnetic field intensity up to 100 mT
- The maximum load is around 10% for a magnetic field intensity around 150 mT

Besides, given the amagnetic material and its lower electrical conductivity, the braking torque on the overall system caused by the shaft is negligible if compared to the one caused by the impeller, regardless of its length.

Probably the most interesting results is given by the dependence of the magnetic field impact on the power of the pump. Indeed, it has been shown that high power pumps are significantly less affected by the SMF.

Finally the orientation of the pump with respect to the magnetic field lines is of crucial importance, as it can determine alone an excessive overload of the entire system if not properly oversized. On the contrary, of the pump is correctly oriented, any oversizing action could in principle be avoided.

10.3 Future works

Different pump impellers and of different materials should still be studied, as the results highly depend on the geometry of the impeller and on its material itself.

In addition, whenever the pump is connected to a variable speed drive and its operation envisages an intermittent load profile, the steady state analysis is not sufficient to quantify the de-rating effect of the magnetic field on the system.

A transient analysis is also crucial for those back up pumps which have to start for safety reasons, indeed the magnetic field could determine during the transient phase an excessive load preventing the pump to start up, therefore, analysing and quantifying the additional power the electric motor has to deliver is of primary importance.

References

[1] M. Garfinkel and W. Engeler, "Magnetic Field Effect on the Current Distribution in p-n Junctions," *Journal of Applied Physics,* vol. 36, pp. 1877-1882, 1965.

[2] W. Hudson, E. Meyn, and C. Schultz, "Transistor performance in intense magnetic fields," *IEEE Transactions on Magnetics,* vol. 6, pp. 704-704, 1970.

[3] E. Karakushan and V. Stafeev, "Large area magnetodiodes," *Soviet Physics-Solid State,* vol. 3, pp. 1476-1482, 1962.

[4] R. Parshad and S. Mehta, "EFFECT OF MAGNETIC FIELD ON VI CHARACTERISTICS OF SOLID STATE DIODES," *INDIAN JOURNAL OF PURE & APPLIED PHYSICS,* vol. 5, pp. 23-&, 1967.

[5] S. Bansal and R. PARSHAD, "DETERMINATION OF MAGNETIC FIELD USING VI CHARACTERISTIC OF SOLID STATE DIODES," vol. 7, ed: NATL INST SCIENCE COMMUNICATION DR KS KRISHNAN MARG, NEW DELHI 110 012, INDIA, 1969, pp. 210-&.

[6] D. Yang, F. Wang, Y. Ren, Y. Zuo, Y. Peng, S. Zhou*, et al.*, "A Large Magnetoresistance Effect in p–n Junction Devices by the Space-Charge Effect," *Advanced Functional Materials,* vol. 23, pp. 2918-2923, 2013.

[7] T. Wang, M. Si, D. Yang, Z. Shi, F. Wang, Z. Yang*, et al.*, "Angular dependence of the magnetoresistance effect in a silicon based p–n junction device," *Nanoscale,* vol. 6, pp. 3978-3983, 2014.

[8] D. Yang, T. Wang, W. Sui, M. Si, D. Guo, Z. Shi*, et al.*, "Temperature-Dependent Asymmetry of Anisotropic Magnetoresistance in Silicon pn Junctions," *Scientific reports,* vol. 5, p. 11096, 2015.

[9] Y. Cao, D. Yang, M. Si, H. Shi, and D. Xue, "Model for large magnetoresistance effect in p–n junctions," *Applied Physics Express,* vol. 11, p. 061304, 2018.

[10] B. G. Streetman and S. Banerjee, *Solid state electronic devices* vol. 4: Prentice Hall Englewood Cliffs, NJ, 1995.

[11] B. V. Zeghbroeck, "Principles of semiconductor devices," 2011.

[12] O. Madelung, *Introduction to solid-state theory* vol. 2: Springer Science & Business Media, 2012.

[13] R. S. Popovic, *Hall effect devices: magnetic sensors and characterization of semiconductors*: CRC Press, 2003.

[14] A. Nathan, "Microtransducer CAD," in *ESSDERC'96: Proceedings of the 26th European Solid State Device Research Conference*, 1996, pp. 707-715.

[15] A. Nathan and T. Manku, "The thermomagnetic carrier transport equation," *Sensors and Actuators A: Physical,* vol. 36, pp. 193-197, 1993.

[16] C. Riccobene, G. Wachutka, J. Burgler, and H. Baltes, "Operating principle of dual collector magnetotransistors studied by two-dimensional simulation," *IEEE transactions on electron devices,* vol. 41, pp. 32-43, 1994.

[17] H. Baltes, L. Andor, A. Nathan, and H. Schmidt-Weinmar, "Two-dimensional numerical analysis of a silicon magnetic field sensor," *IEEE Transactions on Electron Devices,* vol. 31, pp. 996-999, 1984.

[18] C. Riccobene, K. Gartner, G. Wachutka, H. Baltes, and W. Fichtner, "First three-dimensional numerical analysis of magnetic vector probe," in *Proceedings of 1994 IEEE International Electron Devices Meeting*, 1994, pp. 727-730.

[19] W. Allegretto, A. Nathan, and H. Baltes, "Numerical analysis of magnetic-field-sensitive bipolar devices," *IEEE transactions on computer-aided design of integrated circuits and systems,* vol. 10, pp. 501-511, 1991.

[20] ATLAS User's manual - Device simulation software [Online]. Available: http://www.eng.buffalo.edu/~wie/silvaco/atlas_user_manual.pdf

[21] Sentaurus™ Device User Guide [Online]. Available: http://www.sentaurus.dsod.pl/manuals/data/sdevice_ug.pdf

[22] W. Fichtner, D. J. Rose, and R. E. Bank, "Semiconductor device simulation," *SIAM Journal on Scientific and Statistical Computing,* vol. 4, pp. 391-415, 1983.

[23] A. Nathan, "Carrier transport in magnetotransistors," 1989.

[24] S. Selberherr, *Analysis and simulation of semiconductor devices*: Springer Science & Business Media, 2012.

[25] B. J. Baliga, *Fundamentals of power semiconductor devices*: Springer Science & Business Media, 2010.

[26] J. M. Park. Dissertation - Novel Power Devices for Smart Power Applications [Online]. Available: http://www.iue.tuwien.ac.at/phd/park/diss.html#CHILD_LINKS

[27] L. Andor, H. Baltes, A. Nathan, and H. Schmidt-Weinmar, "Numerical modeling of magnetic-field-sensitive semiconductor devices," *IEEE Transactions on Electron Devices,* vol. 32, pp. 1224-1230, 1985.

[28] D. L. Scharfetter and H. K. Gummel, "Large-signal analysis of a silicon read diode oscillator," *IEEE Transactions on electron devices,* vol. 16, pp. 64-77, 1969.

[29] Y. He, "Discretization method for current continuity equation containing magnetic field," *IEEE Transactions on Electron devices,* vol. 39, pp. 820-824, 1992.

[30] Wikipedia. *Bilinear Interpolation*. Available: https://en.wikipedia.org/wiki/Bilinear_interpolation

[31] H. K. Gummel, "A self-consistent iterative scheme for one-dimensional steady state transistor calculations," *IEEE Transactions on electron devices,* vol. 11, pp. 455-465, 1964.

[32] B. Van Zeghbroeck, "Principles of semiconductor devices," *Colarado University,* vol. 34, 2004.

[33] ABB, "Datasheet - 5SDA 11D1702 - Avalanche diode."

[34] P. P. ELECTRONICS, "Datasheet - Rectifier diode AR709."

[35] U. Krey and A. Owen, *Basic theoretical physics*: Springer, 2007.

[36] M. E. Davison, "A Simple Proof that the Lorentz Force, Law Implied Faraday's Law of Induction, when B is Time Independent," *AmJPh,* vol. 41, pp. 713-713, 1973.

[37] J. D. Jackson, "Classical electrodynamics," ed: American Association of Physics Teachers, 1999.

[38] P. E. Randall W. Whitesides. *Basic Pump Parameters and the Affinity Laws*. Available: https://www.pdhonline.com/courses/m125/m125content.pdf